Photodissociation Dynamics and Photoelectron Imaging Spectroscopy of Anions and Anion Clusters

by

Todd J. Sanford

B.S., Purdue University, 1997

A thesis submitted to the

Faculty of the Graduate School of the

University of Colorado in partial fulfillment

of the requirements for the degree of

Doctor of Philosophy

Department of Chemistry and Biochemistry

2004

This thesis for the Doctor of Philosophy degree by

Todd J. Sanford

has been approved for the

Department of Chemistry and Biochemistry

by

_____

W. Carl Lineberger

_____

Robert Parson

Date: _____

Sanford, Todd J. (Ph.D. Physical Chemistry)

Photodissociation dynamics and photoelectron imaging spectroscopy of anions and anion clusters.

Thesis directed by Professor W. Carl Lineberger

The objective of this dissertation is to study the broad topic of solvation by investigating the effects of a solvent environment on small anion solutes in gas-phase clusters. The dihalide solute chromophore, IBr^-, is solvated by a controllable amount of CO_2 molecules and photodissociated with tunable laser radiation. The subsequent solvent-dependent dynamics are monitored by detection of ionic photofragments. The second solute-solvent system involves Cu^- solvated by H_2O molecules with solvent effects on the atomic anion solute studied by photoelectron imaging spectroscopy to monitor solvent-dependent changes in the photoelectron spectrum of the solute.

The first part of the dissertation involves a detailed discussion of the two experimental methods with the previously described cluster ion source and tandem time-of-flight mass spectrometer briefly discussed focusing on modifications made to the existing system for the study of $IBr^-(CO_2)_n$ cluster ions. The remaining portion of the section describes in detail the design and operation of a new velocity-map imaging photoelectron spectrometer.

The second part of the dissertation describes the results of the photodissociation of mass-selected $IBr^-(CO_2)_n$ cluster ions. In one-color experiments, the clusters are excited to two electronic states of the solute anion and the product distributions measured as a function of cluster size. These results are compared to

previous studies on $ICl^-(CO_2)_n$ and $I_2^-(CO_2)_n$ clusters. The dynamics after photoexcitation are shown to be highly dependent on the number of solvent molecules attached and on the identity of solute anion. The solvent is shown to drive such processes as charge-transfer, spin-orbit relaxation, and vibrational relaxation. A femtosecond time-resolved experiment is carried out on $IBr^-(CO_2)_8$ to determine timescales for these events.

The final part of the dissertation investigates the photoelectron imaging spectroscopy of $Cu^-(H_2O)_n$ (n = 1,2) clusters to determine the effect of solvation on an atomic anion solute. The technique of velocity-map imaging is used to produce high resolution images from which the photoelectron energy spectra and photoelectron angular distributions are obtained. Solvation shifts the Cu^- features to higher binding energies along with broadening the spectral features. There are also features present assigned to the water solvent molecules that are confirmed by deuteration experiments.

Acknowledgements

I would like to first thank my advisor, Prof. Carl Lineberger. He is a superb scientist with a breadth of knowledge that seems to know no bounds. This was especially useful to a graduate student who not only did not know the answer to a question, but often did not even know where to start looking. Almost as important as his scientific abilities was his ability to manage his group effectively. Throughout my time here, he has kept a very supportive, laid back atmosphere to the research group while carrying out high level scientific experiments without sacrificing productivity. He also has the ability to bring in good people to the group that fit this mold. He has been a great mentor and has taught me much more than just how to carry out solvation dynamics experiments. I also thank Prof. Barney Ellison with whom I have had many interactions through group meetings. Barney's unbridled enthusiasm for science in general was an enormous inspiration to me. Whenever I had doubts about continuing in graduate school, all it took was to hear Barney give a group meeting to get me excited about not only what he was discussing, but also my own work as well. I want to acknowledge the great help provided to me by our theoretical collaborators Prof. Robert Parson and Matt Thompson. Dr. Jim Faeder and Dr. Nikki Delaney were very helpful early in my graduate career, but Robert and Matt have been invaluable in helping me understand at a deep level what the cluster results from the experiments really mean.

I want to thank all of the members of the Lineberger group that I have been privileged to know and work with over the years. First on the list, I would like to thank Prof. Andrei Sanov, who is now a rising star in the science world at the

University of Arizona. I worked with Andrei, then a postdoc, when I first joined the group. He was instrumental in really getting me excited about the experiment and being a fantastic teacher of not only the ins and outs of our experiment in particular, but how to be an experimentalist in general. After he left, he was still there to answer any questions I had and provided valuable information in designing and troubleshooting the photoelectron imaging spectrometer. I also thank Dr. Sang-Yun Han, Dr. Mark Taylor, Dr. Bert Callicoatt, Dr. Becky Schwartz, Prof. Gustavo Davico, Dr. Jeff Rathbone, Django Andrews, Adam Gianola, Jack Barbera, Dr. Evan Jochnowitz, Dr. Xu Zhang, Prof. Stephen Blanksby, and Dr. Tanya Ramond for being fantastic coworkers in JILA and good friends outside of JILA.

One of the major strengths of JILA is the unmatched support staff employed here. The machine shop and electronics shop, in particular, provided the highest level of knowledge in solving any electrical or mechanical problems and needs that arise in the lab. In the electronics shop, I thank Mike Whitmore, James Fung-a-Fat, Terry Brown, and Paul Beckingham. All of them were always willing to drop what they were doing and answer any questions I had. They were also very easy to work with on the design of electrical components for the lab. The machine shop also has top notch people who were willing to help and work well with us in designing components for the lab. In particular, I thank Hans Green for his always enthusiastic and friendly manner I was greeted with whenever I bothered him with design and machining problems. Finally, I want to thank Brian Lynch in the supply office and Dave Tegart in the electronics shop for being good friends outside of JILA.

Last, but certainly not least, I thank my beautiful wife Kristin for all of support and love throughout this process. I have only known her for roughly the last four years of this, but these were definitely the most trying years of my time here. Although, she didn't always understand what I was doing or why, I knew I had a sympathetic ear and someone who would try to empathize if things didn't go well or congratulate me if they did. She was also a sport in putting up with hearing me say, "I think I'm almost done with grad school. Probably next semester it will be wrapped up," for the past four years.

Table of Contents

List of Tables

List of Figures

Chapter 1

Introduction

1.1 Solvation studies using gas-phase clusters

The process of solvation is of central importance in chemistry and has been the subject of numerous experimental and theoretical studies. The presence of a solvent influences the outcome of a chemical reaction through the interaction of the local environment with the individual species undergoing the reactions. The solvent, on one level, provides an energy bath for the stabilization of energetic products formed during reactions and provides physical barriers to the motion of the reactive species. On a more subtle level, the solvent perturbs the potential energy curves that govern these reactions. Solvation has been shown to be of fundamental importance in such diverse areas as biological activity and atmospheric processes.[1,2]

In condensed phase media, the effects of solvation are easily observed by monitoring macroscopic changes in solute properties or solvent-dependent reaction products. On a microscopic level, understanding of the solvation process is complicated by the poorly defined local environments around solutes in the condensed phase. Studies of these effects will necessarily sample very large numbers of solvent molecules in undetermined configurations about the solutes. The goal of this dissertation is study solvation at a microscopic, molecular level. To achieve this, the detailed interactions between the solute and solvent along with the solvent-solvent interactions must be explored. Information on these interactions at the molecular level is lost due to the statistical nature of descriptions of condensed phase media.

The work presented here attempts to avoid the averaging of molecular details inherent in condensed phase experiments by using gas-phase clusters to provide a controllable, well-defined solvent environment that mimics condensed phase behavior.[3-7] In ionic clusters,[8] the techniques of ion mass spectrometry[9] allow for the study of stepwise microsolvation, since clusters of a desired size can be selected. Supersonic expansions[10] allow for the production of a wide range of cluster sizes from solutes with one or two solvent molecules up to clusters for which the solute is completely enclosed by a solvent cage. The entire ensemble of anionic clusters is introduced into a Wiley-McLaren time-of-flight mass spectrometer[11] where the clusters are then mass selected, thus allowing for the control of the solvent environment by carrying out experiments as a function of cluster size.

1.2 Photodissociation dynamics of size-selected clusters

The behavior of a chromophore following photodissociation has been used to study solvation effects since the work of Franck and Rabinowich[12] in 1934. In that study, neutral I_2 was photodissociated in a liquid solvent and found on occasion to undergo bond recombination or "caging", which was attributed to collisions of the dissociated I atoms with the solvent. This process has also been confirmed by numerous subsequent studies.[13-17] Similar studies on the time-resolved caging dynamics have been carried out on the I_2^- anion in liquids by the Barbara group.[18,19] As mentioned above, the solvent effects in these studies are averaged over a large number of solvent configurations, so that the effects of specific solvent configurations around the solute are unresolved.

The Lineberger group carried out solvent-dependent photodissociation studies in size selected gas-phase clusters, using I_2^- as the solute chromophore and CO_2, OCS, N_2O, and Ar as the solvent.[20-26] The I_2^- anion has a measured bond strength[27,28] of 1.01 eV and the typical binding energy of the above solvents to this solute is around 0.2 eV.[22,29] In the presence of four or five solvent molecules, the total solvent binding energy becomes comparable to the solute bond strength. Accurate potential energy curves[30-32] have been generated which allow for a complete description of the effects of the solvent molecules on the solute anion. These calculated potential energy curves[30,32] are shown in Fig. 1.1 for unsolvated ICl^- and I_2^-.

The first studies on solvated I_2^- in gas phase clusters involved the excitation of the solute chromophore to the A' electronic state as shown in Fig. 1.1(a). In this case, the excited state is asymptotically degenerate with the ground state and very little perturbation to the potentials is needed to induce recombination on the ground state. The results showed that the extent of recombination on the ground state increases with increasing cluster size. This recombination channel turns on with the addition of a sixth CO_2 solvent molecule and reaches 100% with the 16^{th} solvent molecule, corresponding to a complete solvent shell around the solute.[22] Time-resolved pump-probe studies determined the timescales for this recombination for I_2^- in CO_2 clusters.[22,25,33] Typical timescales were on the order of tens of picoseconds with the recombination time decreasing with increasing cluster size. These recombination times were comparable to those determined in the similar experiments on I_2^- in liquids[18,19] leading to the conclusion that gas phase clusters, in this case, do indeed produce solvent-dependent behavior similar to that in condensed phase.

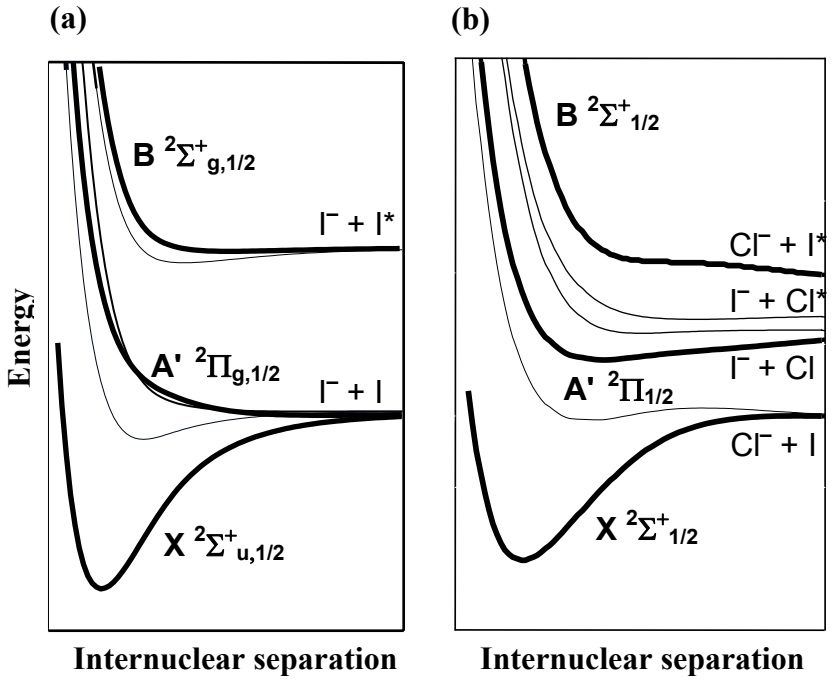

Figure 1.1: Calculated potential energy curves for (a) I_2^- and (b) ICl^- anions. The original calculations are found in references cited in the text. The states in bold are accompanied by their state labels.

Subsequent studies on the I_2^- solute centered on UV excitation to the B electronic state.[20,21] This excitation in size-selected clusters leads not only to the solvent-induced recombination seen in A' excitation, but now includes a spin-orbit relaxation step that must occur before recombination. The recombination on the ground state was shown[20,21] to be depend even more strongly on the number of solvent molecules (and thus the structure of the solvent cage around the solute), due to the additional perturbations to the potential curves required for spin-orbit relaxation. Pump-probe studies[21] determined that the additional spin-orbit step before recombination produced no increase in the recombination time as the observed recombination times for A' and B excitation were very similar. A charge-transfer mechanism[34] has been implicated in the spin-orbit relaxation step, but is not directly observable in the experiments due to the symmetric nature of the solute.

Photodissociation experiments were also carried out on $ICl^-(CO_2)_n$ clusters.[26,35] For this asymmetric solute, the two photodissociated products can be distinguished by ion mass spectrometry. In both excitation to A' and B states (see Fig. 1.1 (b)), the solvent was again shown to drive recombination and spin-orbit relaxation. Solvent-induced charge transfer could now be observed directly. However, $ICl^-(CO_2)_n$ clusters showed decreasing recombination with increasing cluster size, in stark contrast to the I_2^- case for reasons to be discussed in Ch. 3. This behavior coupled with a very low two-photon cross section made $ICl^-(CO_2)_n$ clusters unsuitable for pump-probe experiments to determine recombination timescales.

The photodissociation of $IBr^-(CO_2)_n$ clusters is one of the projects presented in this dissertation. This system is well-suited for photodissociation solvation studies,

because it provides an antisymmetric solute for which time-resolved experiments can be carried out. The photofragmentation of $IBr^-(CO_2)_n$ clusters is shown schematically in Fig. 1.2. There are three classes of products that are possible after exciation of the IBr^- chromophore. Both the Br^--based and I^--based products represent dissociation of the solute anion, while the IBr^--based products arise from the cage effect observed in the condensed phase and in gas-phase cluster studies of I_2^-. The anionic photoproducts are unambiguously detected by a mass-sensitive detection method described in Ch. 2. The product ratios as a function of cluster size reflect the step-wise effects of increasing solvation on the solute anion. The mass-selective detection scheme allows for not only differentiation among the three classes of photoproducts, but also for the determination of the number of solvent molecules evaporated from the products. The solvent evaporation data makes it possible to distinguish between ionic dissociation products that are correlated with different spin-orbit states of the neutral fragments. The Br^--based products formed with spin-orbit excited I retain more solvent molecules than those Br^--based products formed with ground state I and are easily distinguished in the experimental detection.

The one-photon photofragmentation of size-selected clusters clearly demonstrates the effect of the solvent on the solute photodissociation behavior. Recombination, charge-transfer, and spin-orbit relaxation were shown to depend on the number of solvent molecules (and thus the structure of the solvent cages) around the solute. However, these one-photon studies only probe the state of the system at roughly 10 μs after photodissociation when detection of the ionic products occurs.

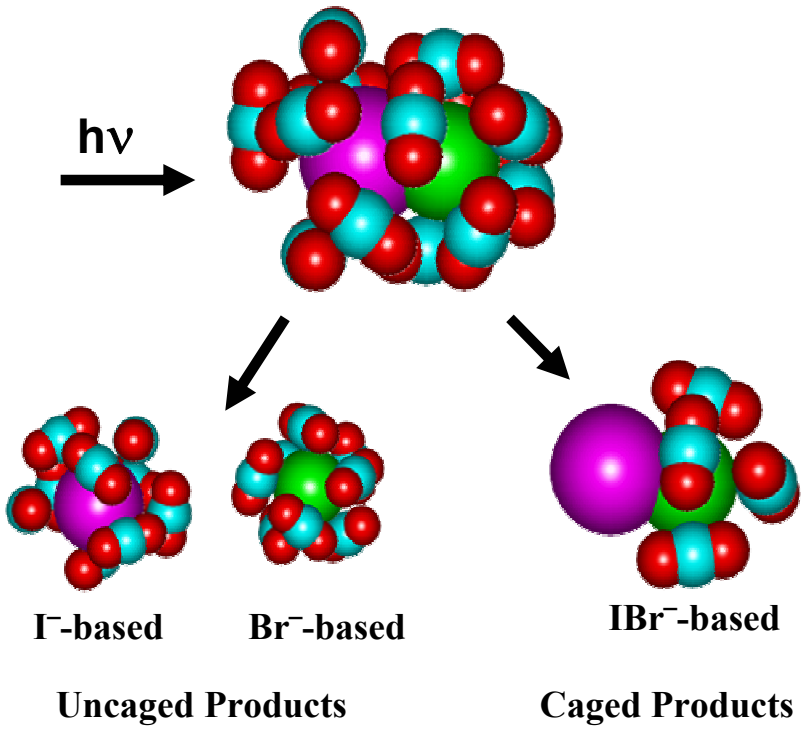

Figure 1.2: The photofragmentation products after photodissociation of size-selected $IBr^-(CO_2)_n$ clusters. The amount of solvent molecules retained on the products identifies the states on which the dissociation products are formed as well as the amount of vibrational relaxation on the ground state for the recombined products.

Pump-probe studies shed light on dynamics at earlier times after photodissociation. This method probes the system only when the solute has recombined on the ground state; the timescales of individual processes such as charge-transfer and spin-orbit relaxation along with any other excited state dynamics cannot be directly measured. Such phenomena as potential wells formed on the excited electronic states of the solute and reorganization of the solvent cage are thought to be critical to the overall recombination dynamics, but are not observed using the photodissociation methods described above. Anion photoelectron spectroscopy is ideally suited for these excited state dynamics studies. After photodissociation, the excess negative charge resides on species (IBr^-, Br^-, or I^- in the case of $IBr^-(CO_2)_n$ cluster photodissociation) that are easily photodetached. The time evolution of the photodetachment signal will yield snapshots of the system throughout the entire excited and ground state dynamics and is not limited to a narrow window on the ground state. This will provide a much more powerful tool in studying the solvation dynamics of these dihalide systems.

1.3 Photoelectron imaging spectroscopy

Anion photoelectron spectroscopy (PES)[36] has proven to be an invaluable tool for the study of the structures and energetics of both anions and neutrals. An important parameter obtained from anion photoelectron spectroscopy is the electron affinity of the neutral molecule, which can be used in a thermochemical cycle for the determination of bond strengths.[37,38] Vibrational frequencies of neutral molecules can be extracted from vibrational progressions in the spectra while those of the anions can be determined from vibrational hot bands, as can term energies of electronic states,

spin-orbit splittings and bond lengths of both the anion and neutral. A powerful application of anion PES is the study of reactive neutral species formed via the photodetachment of the precursor anion that cannot otherwise be directly prepared. Photodetachment of anions is also used to prepare neutral species at the transition state geometry on the neutral ground state surface, in order to study the subsequent reactions.[39,40]

The anion photoelectron spectroscopy experiment is simply described by the process:

$$AB^- + h\nu \rightarrow AB + e^- \quad (1.1)$$

where AB^- is the precursor anion species, $h\nu$ is the photon energy, AB is the neutral species formed from photodetachment, and e^- is the photodetached electron. The process is depicted schematically in Fig. 1.3. The photodetached electron kinetic energies (eKE) are measured to yield the photoelectron spectrum shown in Fig.1.3. The eKEs are typically converted to electron binding energies (eBE) by subtracting the eKE from the photon energy yielding spectra independent of the photon energy. The Franck-Condon Principle, stating that photodetachment of the electron is much faster than any nuclear motion, constrains the geometries of the anion and neutral to be equivalent upon photodetachment. For anions and neutrals with similar equilibrium geometries, the electron affinity can be measured as the transition between the lowest vibrational energy levels of the ground states of the two species.

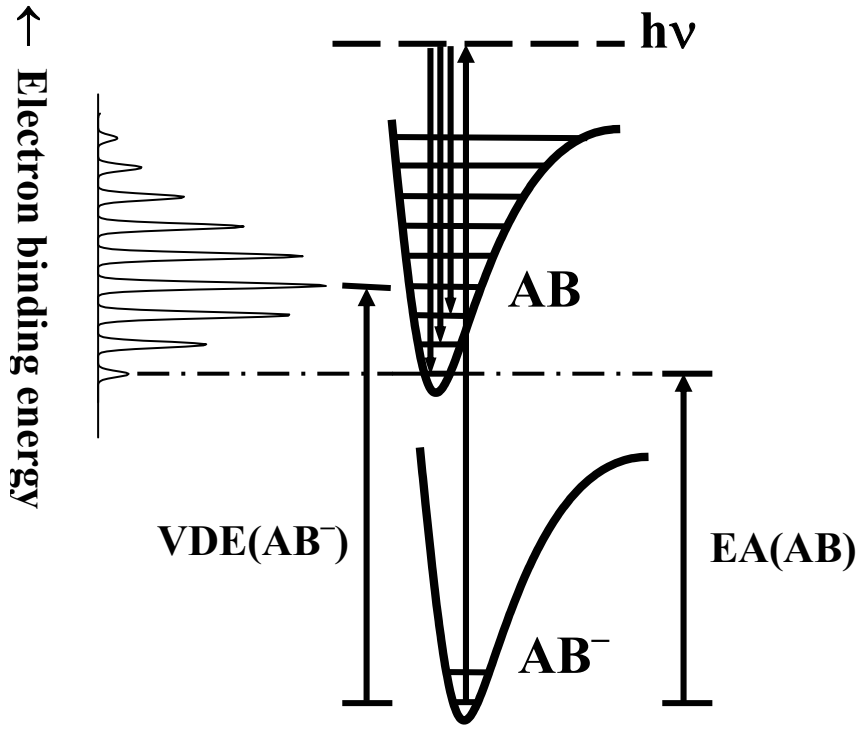

Figure 1.3: Schematic diagram of the photoelectron spectrum of the photodetached AB^- anion at a fixed photon energy, hν. The spectrum represents transitions to vibrational states of the ground electronic state of the neutral AB. The transitions representing the EA and VDE discussed in the text are shown.

However, if the equilibrium geometries are significantly different, this transition is very weak and the vertical detachment energy (VDE) is then reported as the transition from the lowest vibrational state of the anion to the state in the neutral with same geometry as the anion. Photoelectron angular distributions are also obtained from the photoelectron spectra and used to determine the anisotropy parameter, β.[41] The value of β reflects the symmetry of the electronic orbital from which the photoelectron is detached. This analysis is rigorous for atomic systems, but is less exact for molecules. The value of β is experimentally obtained by taking photoelectron spectra at multiple laser polarizations.[42]

Photoelectron imaging of negative ions[43-48] can trace its roots to the pioneering imaging experiments[49] of Houston and Chandler on photofragments formed from the photodissociation of neutral molecules. The images simultaneously provide the full three dimensional velocity distributions of all of the particles, from which the individual velocities (kinetic energies) and angular distributions can be obtained. The photoelectron energy spectra as described above are extracted from photoelectron images that now also directly contain the photoelectron angular distributions (PAD) necessary for a description of the properties of the orbitals from which the photoelectrons are detached.[50] These two observables (kinetic energy and angular distributions) are measured simultaneously adding enormously to the application of this technique, which can be extended to the time domain.[43,45,51]

A key step in the development of photoelectron imaging as an effective experimental tool was the introduction of velocity-map imaging[52] by Parker and Eppink. The ability to obtain high resolution images, and thus well resolved

photoelectron energy spectra, had suffered from blurring associated with the extended, non-point source of the anions from which photodetachment occurs. The quality of the images is determined in large part by how the three-dimensional (3D) photoelectron distributions are mapped onto the two-dimensional (2D) detector. Parker and Eppink recognized that the quality of the 2D images, from which the 3D distributions are reconstructed, depends on the configuration of the electrodes used to extract the electrons from the photodetachment region to the detector. A three element open electrode configuration was found to minimize distortions to images caused by grid electrodes as well provide unique focusing characteristics. Parker and Eppink determined that when appropriate voltages are applied to the electrodes the particles with the same initial velocity vector are mapped onto the same point on the detector regardless of their initial position upon photodetachment, hence the term "velocity map imaging." This allows for the acquisition of high quality images despite the use of an extended ion source. The velocity map imaging electrode configuration and mapping characteristics are depicted in Fig 1.4 along with typical electrode voltages used for the imaging experiments described within.

The high quality 2D images detected do not represent the full 3D electron distribution necessary to obtain the photoelectron energy spectra and angular distributions. The task is to reconstruct the 3D distribution from the 2D projection on the detector. For images where the electrons' photodetachment kinetic energy is much less than the kinetic energy acquired in the acceleration stage, cylindrical symmetry exists and the 2D projection can be transformed into the 3D distribution by use of the Abel integral.[53] This cylindrical symmetry requirement dictates that the

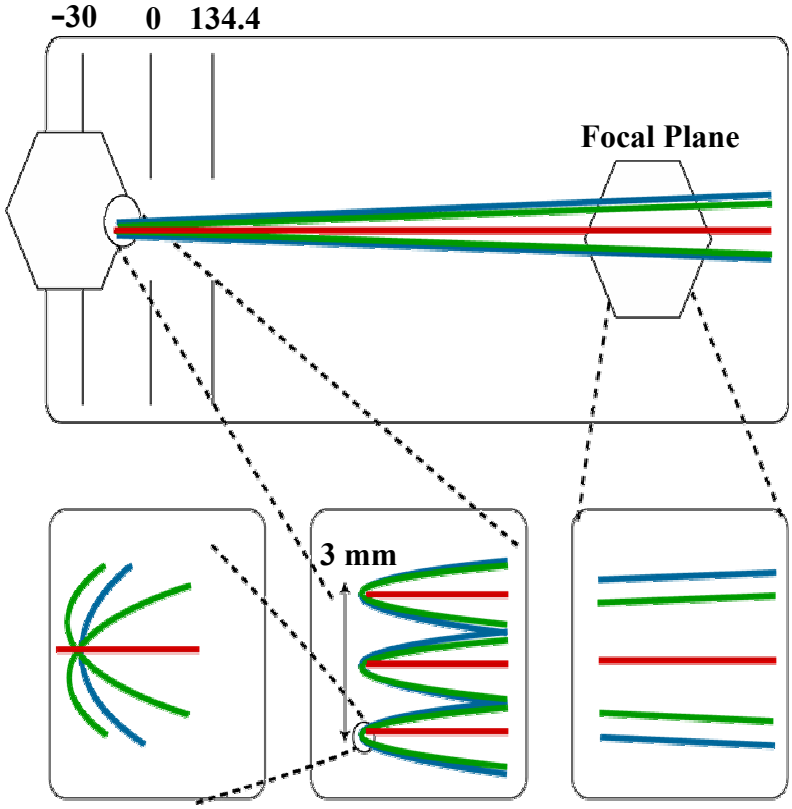

Figure 1.4: Velocity map imaging electrode configuration with experimental voltages applied shown in volts with the focusing properties of the electrons. The different colors for the trajectories represent different initial velocities of the photodetached electrons. The schematic demonstrates that electrons with the same initial velocity in the focal plane are mapped onto the same point on the detector despite an extended ion source of 3 mm.

photodetachment laser polarization be parallel to the plane of the detector. However, this transform can lead to reconstructed images that are very noisy and contain singularities due to the form of the transform integral. Reisler and coworkers developed the basis set expansion (BASEX) method[53] to produce much higher quality reconstructions that avoid the pitfalls of Abel transform methods. This method expands the 2D image projection in a basis set of well-behaved, Gaussian-like functions. The full 3D distribution is then reconstructed as a linear combination of these well-behaved functions. The BASEX software takes a 2D slice through the 3D distribution reconstruction from which the photoelectron spectrum as a function of camera pixel (later converted to electron kinetic or binding energy) is produced and the values of β as a function of pixel are calculated. The imaging process is shown schematically in Fig. 1.5 as well as the associated sample raw and BASEX reconstructed images.

1.4 Dissertation overview

The remainder of the dissertation is broken into five chapters. Chapter 2 describes the cluster ion sources and the Wiley-McLaren time-of-flight and reflectron mass spectrometers. Various modifications made to the existing system for production of the $IBr^-(CO_2)_n$ cluster ions are presented along with descriptions of the femto- and nanosecond laser systems employed here. This chapter also describes the design and implementation of the velocity map imaging spectrometer.

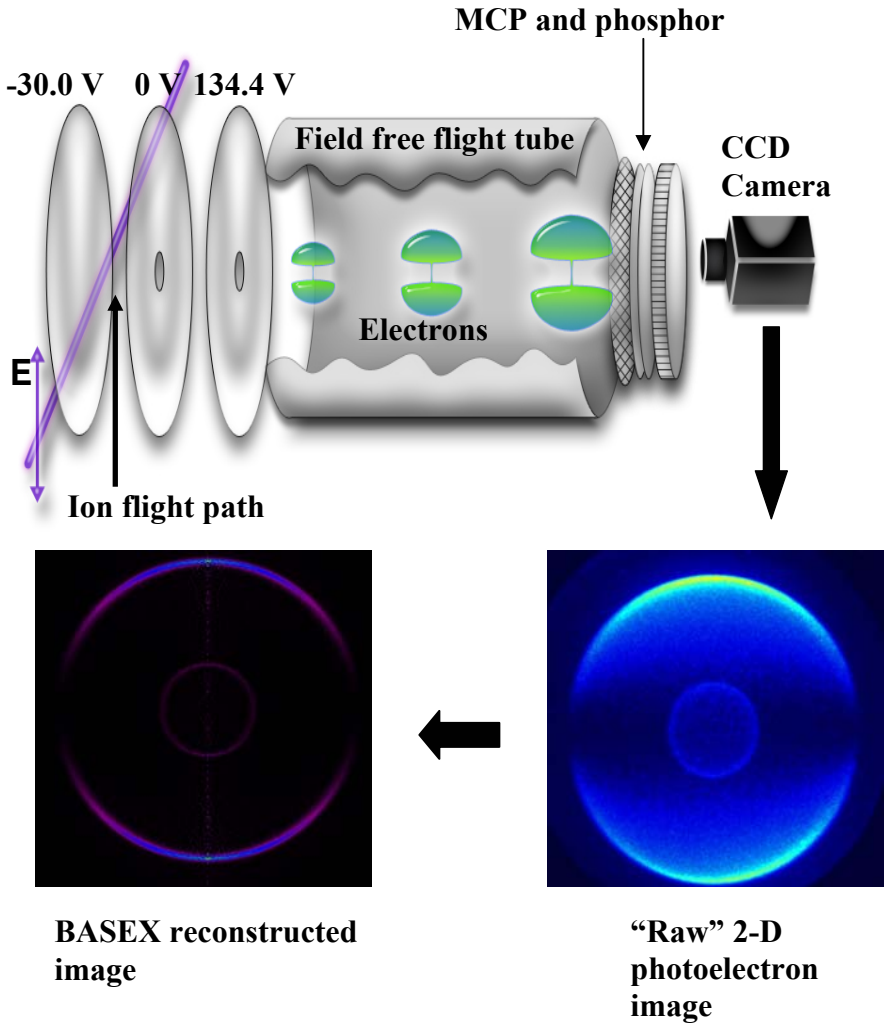

Figure 1.5: Photoelectron imaging system including the electrodes arranged in velocity-map imaging mode. A typical raw image recorded with the CCD camera as well as the BASEX reconstruction of the raw image are shown.

Chapter 3 discusses the photofragmentation studies carried out on $IBr^-(CO_2)_n$ clusters to determine the effect of the CO_2 solvent on the dihalide solute anion. The bare IBr^- solute is first spectroscopically characterized to determine absorption cross sections and the bond strength of the solute. The photoproduct ratios are then measured as a function of cluster size upon excitation to two electronic states of the solute anion. A time-resolved pump-probe experiment is carried out to determine the recombination time after excitation to the lower electronic state studied. The solvation dynamics of $IBr^-(CO_2)_n$ are then discussed in the context of a comparison with the dynamics of $ICl^-(CO_2)_n$ and $I_2^-(CO_2)_n$ clusters studied previously in this group.

The photoelectron imaging spectroscopy of Cu^- and $Cu^-(H_2O)_n$ (n = 1,2) clusters is the subject of Chapter 4. The copper anion is used to provide an atomic system for characterization and optimization of the new imaging spectrometer. The photoelectron spectra of the $Cu^-(H_2O)_n$ anion complexes are used to determine the effect of the solvent on the electronic structure of the Cu^- solute and to characterize the neutral complexes formed after the photodetachment of the anion. This work supplements previous time-resolved experiments and calculations on these systems that investigate the dynamics of the complex after photodetachment.[54-56]

Chapter 5 describes experiments involving the photodissociation of mixed trihalide anions to produce vibrational wavepackets in the dihalide anion photoproduct. The time-resolved experiments use a second probe photon to monitor the evolution of the wavepackets on the dihalide ground state potential. Finally,

Chapter 6 presents a summary of the dissertation work as well as conclusions and future directions that build on the results presented here.

Chapter 1 References

[1] W. T. Keeton and J. L. Gould, *Biological Science*, 5th ed. (W.W. Norton & Co., New York, 1993).

[2] A. R. Ravishankara, Science **276**, 1058 (1997).

[3] A. W. Castleman, Int. J. Mass Spect. Ion Proc. **118**, 167 (1992).

[4] A. W. Castleman and K. H. Bowen, J. Phys. Chem. **100** (31), 12911 (1996).

[5] J. M. Farrar, in *Current Topics in Ion Chemistry and Physics*, edited by C. Y. Ng and I. Powis (Wiley, New York, 1992).

[6] A. Sanov and W. C. Lineberger, Physical Chemistry Chemical Physics **6**, 2018 (2004).

[7] A. Sanov and W. C. Lineberger, PhysChemComm **5**, 165 (2002).

[8] A. W. Castleman, Jr. and R. G. Keesee, Chem. Rev. **86**, 589 (1986).

[9] M. A. Johnson and W. C. Lineberger, in *Techniques for the Study of Ion Molecule Reactions*, edited by J. M. Farrar and J. W. Saunders (Wiley, New York, 1988), pp. 591.

[10] R. E. Smalley, L. Wharton, and D. H. Levy, Accts. Chem. Res. **10**, 139 (1977).

[11] W. C. Wiley and I. H. McLaren, Rev. Sci. Instr. **26** (12), 1150 (1955).

[12] J. Franck and E. Rabinowitch, Trans. Faraday Soc. **30**, 120 (1934).

[13] L. F. Meadows and R. M. Noyes, J. Am. Chem. Soc. **82**, 1872 (1960).

[14] J. Troe, Ann. Rev. Phys. Chem. **29**, 223 (1978).

[15] B. Otto, J. Schroeder, and J. Troe, J. Chem. Phys. **81** (1), 202 (1984).

[16] X. Xu, S. Yu, R. Lingle, H. Zhu, and J. B. Hopkins, J. Chem. Phys. **95** (4), 2445 (1991).

[17] A. L. Harris, J. K. Brown, and C. B. Harris, Ann. Rev. Phys. Chem. **39**, 341 (1988).

[18] A. E. Johnson, N. E. Levinger, and P. F. Barbara, J. Phys. Chem. **96**, 7841 (1992).

[19] D. A. V. Kliner, J. C. Alfano, and P. F. Barbara, J. Chem. Phys. **98** (7), 5375 (1993).

[20] S. Nandi, A. Sanov, N. Delaney, J. Faeder, R. Parson, and W. C. Lineberger, J. Phys. Chem. **102** (45), 8827 (1998).

[21] A. Sanov, T. Sanford, S. Nandi, and W. C. Lineberger, J. Chem. Phys. **111** (2), 664 (1999).

[22] J. M. Papanikolas, J. R. Gord, N. E. Levinger, D. Ray, V. Vorsa, and W. C. Lineberger, J. Phys. Chem. **95** (21), 8028 (1991).

[23] J. M. Papanikolas, P. J. Campagnola, V. Vorsa, M. E. Nadal, H. K. Buchenau, R. Parson, and W. C. Lineberger, in *The Chemical Dynamics and Kinetics of Small Radicals*, edited by K. Liu and A. Wagner (World Scientific Publishing Co., Singapore, 1995), Vol. 6, pp. 616.

[24] J. M. Papanikolas, V. Vorsa, M. E. Nadal, P. J. Campagnola, J. R. Gord, and W. C. Lineberger, J. Chem. Phys. **97** (9), 7002 (1992).

[25] V. Vorsa, S. Nandi, P. J. Campagnola, M. Larsson, and W. C. Lineberger, J. Chem. Phys. **106** (4), 1402 (1997).

[26] M. E. Nadal, Ph.D. Thesis, University of Colorado, 1996.

[27] B. J. Greenblatt, M. T. Zanni, and D. M. Neumark, Chem. Phys. Lett. **258** (5), 523 (1996).

[28] M. T. Zanni, T. R. Taylor, B. J. Greenblatt, B. Soep, and D. M. Neumark, J. Chem. Phys. **107** (19), 7613 (1997).

[29] J. M. Papanikolas, V. Vorsa, M. E. Nadal, P. J. Campagnola, H. K. Buchenau, and W. C. Lineberger, J. Chem. Phys. **99** (11), 8733 (1993).

[30] P. E. Maslen, J. Faeder, and R. Parson, Chem. Phys. Lett. **263** (1-2), 63 (1996).

[31] P. E. Maslen, J. M. Papanikolas, J. Faeder, R. Parson, and S. V. ONeil, J. Chem. Phys. **101** (7), 5731 (1994).

[32] J. Faeder, Ph.D. Thesis, University of Colorado, 1998.

[33] B. J. Greenblatt, M. T. Zanni, and D. M. Neumark, J. Chem. Phys. **112**, 601 (2000).

[34] N. Delaney, J. Faeder, and R. Parson, J. Chem. Phys. **111**, 651 (1999).

[35] M. E. Nadal, P. D. Kleiber, and W. C. Lineberger, J. Chem. Phys. **105** (2), 504 (1996).

[36] K. M. Ervin and W. C. Lineberger, in *Advances in Gas Phase Ion Chemistry*, edited by N. G. Adams and L. M. Babcock (JAI Press, Greenwich, 1992), Vol. 1, pp. 121.

[37] K. M. Ervin, S. Gronert, S. E. Barlow, M. K. Gilles, A. G. Harrison, V. M. Bierbaum, C. H. DePuy, W. C. Lineberger, and G. B. Ellison, J. Am. Chem. Soc. **112**, 5750 (1990).

[38] S. J. Blanksby, T. M. Ramond, G. E. Davico, M. R. Nimlos, S. Kato, V. M. Bierbaum, W. C. Lineberger, G. B. Ellison, and M. Okumura, J. Am. Chem. Soc. **123** (39), 9585 (2001).

[39] D. M. Neumark, Science **272** (5267), 1446 (1996).

[40] D. M. Neumark, PhysChemComm **11**, 76 (2002).

[41] J. Cooper and R. N. Zare, J. Chem. Phys. **48**, 942 (1968).

[42] T. M. Ramond, Ph.D. Thesis, University of Colorado, 2001.

[43] A. V. Davis, R. Wester, A. E. Bragg, and D. M. Neumark, J. Chem. Phys. **118**, 999 (2003).

[44] R. Mabbs, E. Surber, and A. Sanov, Analyst **128**, 765 (2003).

[45] R. Mabbs, K. Pichugin, E. Surber, and A. Sanov, J. Chem. Phys. **121**, 265 (2004).

[46] E. Surber, R. Mabbs, and A. Sanov, J. Phys. Chem. A **107** (40), 8215 (2003).

[47] A. Osterwalder, M. J. Nee, J. Zhou, and D. M. Neumark, J. Chem. Phys. **121** (13), 6317 (2004).

[48] A. E. Bragg, J. R. R. Verlet, A. Kammrath, and D. M. Neumark, J. Chem. Phys. **104**, 3515 (2004).

[49] D. W. Chandler and P. L. Houston, J. Chem. Phys. **87** (2), 1445 (1987).

[50] K. L. Reid, Ann. Rev. Phys. Chem. **54**, 397 (2003).

[51] L. Wang, H. Kohguchi, and T. Suzuki, Faraday Discuss. **113**, 37 (1999).

[52] A. Eppink and D. H. Parker, Rev. Sci. Instr. **68** (9), 3477 (1997).

[53] V. Dribinski, A. Ossadtchi, V. Mandelshtam, and H. Reisler, Rev. Sci. Instr. **73**, 2634 (2002).

[54] F. Muntean, M. S. Taylor, A. B. McCoy, and W. C. Lineberger, J. Chem. Phys. **121**, 5676 (2004).

[55] M. S. Taylor, J. Barbera, C. P. Schulz, F. Muntean, A. B. McCoy, and W. C. Lineberger, J. Chem. Phys. **submitted** (2004).

[56] M. S. Taylor, F. Muntean, W. C. Lineberger, and A. B. McCoy, J. Chem. Phys. **121**, 5688 (2004).

Chapter 2

Experimental Hardware and Methods

2.1 Overview

The various experiments carried out in this work involved the use of a single tandem time-of-flight mass spectrometer. However, numerous modifications were made throughout the course of these experiments to meet the requirements of the specific chemical systems used and the various detection methods. The system is first described in its original configuration with the modifications presented as they occurred. The system is used to produce anions and anion clusters of various precursor species. These ions are injected into a Wiley-McLaren time-of-flight mass spectrometer[1] where they are mass-selected and intersected with laser pulses of varying wavelength and pulse duration. The photodissociated anion and neutral fragments are then detected with two microchannel plate detectors. The significant modification to the system involves the design and implementation of a velocity-map imaging[2] photoelectron spectrometer into the existing apparatus. The lasers used to generate the nanosecond and femtosecond pulses along with the various optical components are also discussed in some detail. An overall schematic of the apparatus before implementation of the electron imaging system is depicted in Fig. 2.1.

.

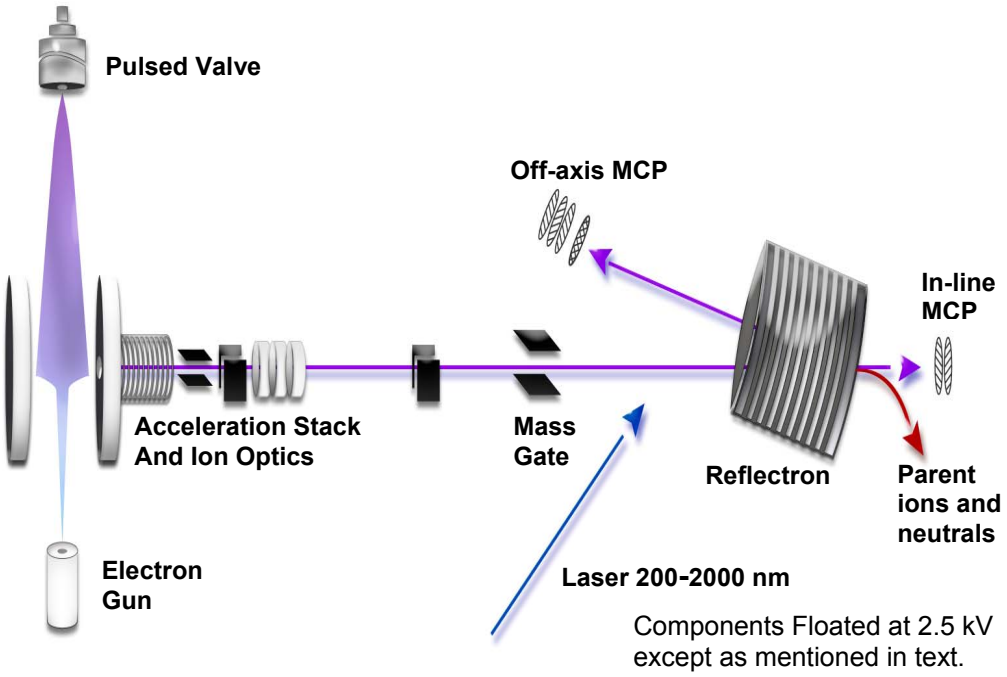

Figure 2.1: Cluster ion source and tandem time-of-flight mass spectrometer.

2.2 Cluster Ion and Discharge Sources

The $IBr^-(CO_2)_n$ cluster ions are created by crossing a neutral supersonic expansion with a high energy beam of electrons.[3] The supersonic neutral expansion is formed by passing a backing gas, which is typically neat CO_2 or CO_2 diluted with Ar, at pressures of 30 to 50 psig over a stainless steel reservoir containing a solid sample of iodine monobromide (Aldrich). The methods for the production of $ICl^-(CO_2)_n$ and $I_2^-(CO_2)_n$ cluster ions are described in detail elsewhere.[4-7]

The most important factor in the formation of the IBr-containing species is providing sufficient time for the IBr vapor to saturate the lines and valve. A passivation time of about a week is required after any thorough cleaning of the stainless steel lines or the pulsed valve. A qualitative observation is that until sufficient saturation of the lines and valve is achieved the dominant ions in the mass spectra are I^- along with I^--based clusters. There is also an $I_2^-(CO_2)_n$ progression along with the ubiquitous $(CO_2)_n^-$ peaks. Initially, there are no IBr^--based peaks. As the IBr saturation of the lines proceeds, the mass spectra show the $IBr^-(CO_2)_n$ peaks growing in at the expense of the corresponding I^-- and I_2^--based cluster peaks with the $(CO_2)_n^-$ ions remaining nearly constant in intensity. Once the saturation has been achieved, IBr^- clusters then persist as the dominant peaks until the next cleaning. The IBr reservoir is typically heated to about 40°C with the pulsed valve kept at a few degrees higher to avoid clogging. For the most stable ions, the CO_2 was initially mixed in the reservoir. The outlet is then left open with the inlet closed as the CO_2 bypasses the reservoir. The production schemes for the trihalide anions are discussed in Ch. 5.

The supersonic expansion is formed by expanding the gas mixture through a Series 9 General Valve with an 800 μm aperture on the faceplate. The poppets found to perform the best were made from KELF and Teflon. The valve is driven at 30, 50, or 80 Hz by a trigger pulse from a Stanford Delay Generator. The TTL trigger is amplified and varied in width before being sent to the valve solenoid. The voltage of the driving pulse can be varied and it is found that the most stable ion production occurs when a voltage of around +100 V is applied. The driving pulse duration is 200–600 μs with the actual gas pulse slightly longer. The production of large clusters with good intensities is also very dependent on the adjustment of the valve. The optimal adjustment has the pulse barely discernible to the touch at 30 Hz and a pulse width of 450 μs. The body of the valve can be heated or cooled with four thermoelectric pads along with water cooling lines attached to copper pads that are in contact with the valve housing block. A grounding cable is also attached to the face plate to prevent charging of the valve due to its electrical isolation from the chamber.

An electron gun produces the high energy beam of electrons via thermionic emission from a bent thoriated iridium filament (Electron Technology, Inc.). This filament is heated by passing approximately 6 amps through it. The electrons are extracted from the filament region and mildly focused by an anode plate that is negatively biased from the filament by about 80–200 V. Both the filament and the anode plate are floated at +1000 V. After extraction the electrons encounter an einzel lens that provides additional focusing of the electrons. The lens consists of two plates held at ground and a middle plate at around –1000 V. The two ground plates have apertures of roughly 0.054″ and the middle plate has an aperture of 0.30″. The

electron beam is steered by a set of horizontal and vertical deflectors that typically have modest voltages of 0–50 V. The electron gun is positioned in a perpendicular arrangement to the expansion nozzle about 5 cm away from the nozzle assembly. The electron beam axis in the gun is positioned as close as possible to the end of the nozzle in the horizontal direction to ensure that the electron beam intersects a high density portion of the expansion close to the orifice. The vertical and horizontal deflectors provide a fine adjustment of this condition with the electron beam sometimes skimming the face plate. The electron current is measured by a Faraday cup positioned on the opposite side of the valve with electron currents in the range of a few hundred μA.

A discharge source is used for the production of Cu^- and various clusters consisting of Cu^- solvated by water along with impurities, such as copper hydroxides and copper oxides. A representative mass spectrum is shown in Fig. 2.2 with the peaks of experimental interest assigned and labeled. The discharge replaces the electron gun as the source for ion production. A General Valve analogous to the one described above is used, but slightly modified by having four threaded holes drilled into the face plate. A Macor block is attached to this faceplace with Teflon screws. The Macor block has a 4 mm orifice in the center. A copper rod and a stainless steel rod are brought in from the sides of the block through a channel perpendicular to the gas flow channel with the 4 mm orifice. The two rods are separated by typically 1.5 mm in the center of the orifice. The stainless steel rod is kept at ground and the copper rod is held at −1000 to −3000 V. When the valve is pulsed and the gas expansion is present, there is a discharge from the copper rod to the grounded

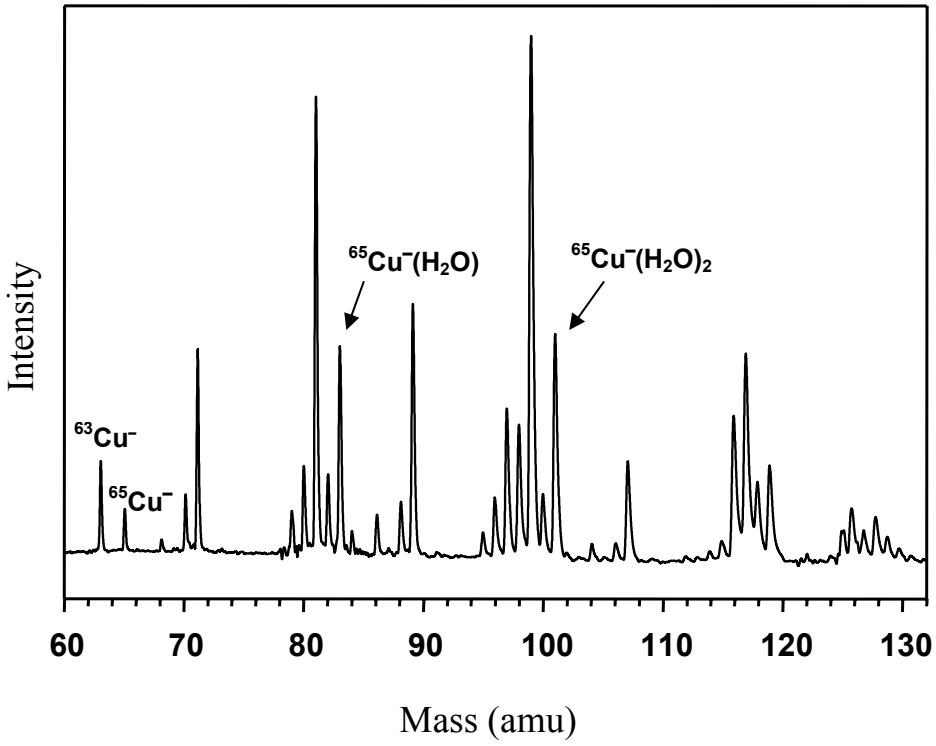

Figure 2.2: Time-of-flight mass spectrum of water in the copper discharge source. The ions used in the experiments are denoted with arrows along with the two isotopes of copper atomic anion. The other peaks represent species such as copper oxides, copper hydroxides, and water hydroxides.

stainless rod. For the copper-water anion experiments, a backing gas mixture of 40 psig is passed over a stainless steel reservoir containing water. The gas mixture found to be the most effective at making copper-water clusters consists of 40 psig of Ar and 210 psig of Ne (16% Ar). As the gas passes through the discharge region, the Ar gas is ionized producing Ar^+ and secondary electrons. The positively charged ions are attracted to the negatively charged copper rod and sputter off neutral, anionic, and cationic copper atoms. The secondary electrons attach to the neutral atoms forming additional negative copper ions. Clustering around the newly formed negative charge centers then occurs in a manner similar to that described below for the dihalide anions. A more detailed account of the dimensions and operation of the discharge source can be found elsewhere.[8]

2.3 Cluster Ion Formation

The intersection of a high energy electron beam with the molecules in a free jet expansion ionizes a portion of the initially neutral molecules to produce cations and low energy secondary electrons that collisionally cool to around 1 eV.[3,9] These secondary electrons remain in the expansion and then attach to neutral molecules via collisions.

There are two major mechanisms for formation of the anion clusters observed in the mass spectra.[4] The first mechanism is rather straightforward and is responsible for the formation of the dihalide anion clusters. A given anion, IBr^- for example, is formed by attachment of secondary electrons to the neutral dihalide species found in

the expansion. Cluster growth then occurs as the solvent molecules, CO_2 in this case, condense around the newly formed charge centers by the following mechanism:

$$IBr + \text{secondary } e^- + M \rightarrow IBr^- + M$$

$$IBr^- + CO_2 + M \rightarrow IBr^-(CO_2) + M$$

$$IBr^-(CO_2) + CO_2 + M \rightarrow IBr^-(CO_2)_2 + M$$

$$IBr^-(CO_2)_n + CO_2 + M \rightarrow IBr^-(CO_2)_{n+1} + M.$$

This mechanism shows that cluster growth depends on the presence of neutral CO_2 molecules along with third body collision partners. Regions of high density in the expansion favor large cluster growth.

The second mechanism is responsible for the ubiquitous $(CO_2)^-_n$ clusters that are present in spectra where CO_2 is used as a backing gas. In this case, there is not a negatively charged nucleation center as is the case for the dihalide anions, due in part to the CO_2^- anion being unstable. The $(CO_2)_n^-$ anion clusters are instead formed by attachment of the slow secondary electrons to neutral CO_2 clusters already formed in the expansion. The negative cluster ions are then stabilized by ejection of neutral monomers and collisions with other molecules in the expansion,

$$(CO_2)_n + \text{secondary } e^- \rightarrow [(CO_2)_n^-]^* \rightarrow (CO_2)_m^- + (n\text{-}m)\ CO_2.$$

The formation of these clusters depends less on the position of the high energy electron beam with respect to the dense part of the expansion, because cluster growth occurs before interaction with the high energy electrons.

The keys to cluster growth around the dihalide ions of interest are both the density of the expansion and the temperature. The clusters grow based on the interaction of the newly formed dihalide ion and the neutral CO_2 molecules in the

expansion. Long drift distances are needed for sufficient cluster growth. The drift distance is about 15 cm, which is the distance from the pulsed valve to the extraction region in the apparatus. The formation of a neutral plasma keeps the ions coupled to the neutral CO_2 molecules over this long drift distance. Otherwise, the ions would undergo diffusion from Coulomb repulsion and the densities would be much less than the $10^9/cm^3$ density that is estimated[3] in the extraction region. The ion-molecule reaction rate[10] (Langevin reaction rate) determines the collision rate between the dihalide ions and the neutral solvent molecules necessary for cluster growth. This reaction rate is shown to be independent of temperature and cluster growth is facilitated by having a very dense expansion over large distances. Temperature does become important, however, because the clusters expel their excess energy to become more stable by collisional cooling with neutral molecules in the expansion and also by evaporation of monomer solvent molecules. Lower expansion temperatures may not be important for the ion-molecule reaction rates, but they are important for limiting excess energy that clusters contain thus making the evaporation of solvent molecules unnecessary and leading to the production of larger clusters. The ideal expansion is then both as cold and as dense as possible over long distances. The clusters in this source are estimated to have a temperature of 50–60 K based on RRKM calculations.[11]

2.4 Cluster Ion Source Modifications

Modifications were made to the existing cluster ion source during the work carried out on $IBr^-(CO_2)_n$ cluster ions. Initially, large clusters (n>11) of usable intensities were absent from the mass spectra. Large clusters were present in the $ICl^-(CO_2)_n$ and $I_2^-(CO_2)_n$ systems with experiments carried out up to around n = 20 in some cases. The $IBr^-(CO_2)_n$ mass spectra showed an increase in intensity with increasing n up to a maximum at around n = 7,8,9. The intensities of the clusters then quickly dropped off with n = 11 usually being the larger cluster of usable intensity.

The first modification is based on the work of the Johnson group.[12] Their electron gun is operated in a position collinear with the expansion nozzle. This mode of operation guarantees that the high energy electrons interact with the densest part of the expansion. The production mechanism for the $IBr^-(CO_2)_n$ cluster ions indicates that the position of the electron beam with respect to the nozzle orifice is critical to the production of large clusters. Having the electron beam propagate collinearly allows steering of the beam down the throat of the nozzle thus guaranteeing interaction with the absolute densest part of the expansion.

The electron gun is moved from the previous perpendicular position described above to a position in-line with the nozzle on the opposite side of the extraction region. The end of the gun was positioned about 15 cm from the center of the aperture to the time-of-flight portion of the instrument, the same distance as the valve orifice to the time-of-flight entrance. The electron beam is quite diffuse at the expansion interaction region after traveling over the 30 cm from the gun to the nozzle orifice. A small samarium-cobalt ring magnet was attached to the faceplate of the

valve to focus the diffuse electron beam into the nozzle orifice. The electron beam is aligned by adjusting the gun deflectors as the appearance of a visible plasma at the valve faceplate is monitored. The deflectors are then fine tuned by monitoring the mass spectra on an oscilloscope. The electron beam current is measured by a smaller Faraday cup that is placed on a vertically retractable arm. The electron beam current is maximized and then the Faraday cup is removed from the electron beam and ion path easily.

The second modification to the cluster source involves the redesign of the supersonic expansion nozzle. Previously, commercially available nozzles employed in the cluster source had valve orifices of 0.8 mm and cone angles of 90º. There is also a small, narrow channel between the poppet and the orifice in which the poppet rests and the gas must pass through before expansion. Studies have been published by the Even group[13,14] where they investigate the properties of rare gas expansions as a function of the valve geometry. They found that an optimum cone angle of 40° provides the best spatial confinement of the expansion over long distances. Their studies also measure temperatures of the expansions to the tenths of Kelvin range. With these results, a new nozzle is designed for the cluster ion source that is depicted in Fig. 2.3. Due to machining constraints, the valve orifice was decreased to only 0.61 ± 0.02 mm from the original 0.8 mm of the commercial valve. The Even nozzles have much smaller orifices of 0.1 mm. Another parameter found to be important is the ratio of the total nozzle length to the nozzle orifice. The nozzles that produced good spatial confinement and low temperatures had ratios of around 30. The machined nozzle for the IBr source has a ratio of only 6.6. Another change in the

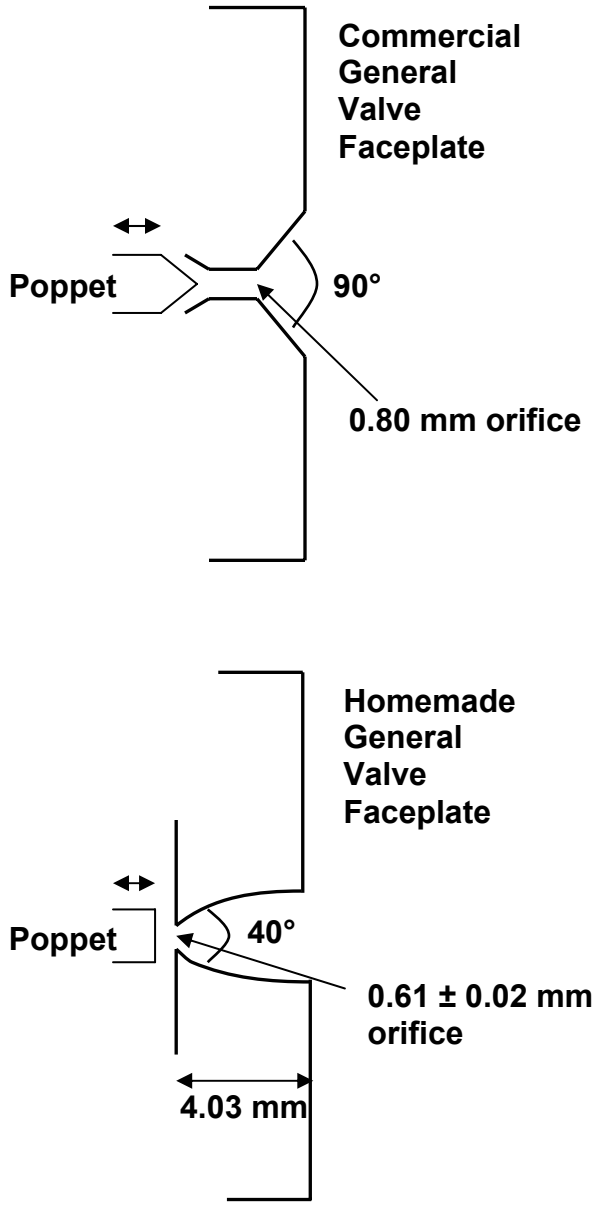

Figure 2.3: Cross sections and dimensions of the commercial and homemade faceplates for a General Valve.

new nozzle is the manner in which the poppet rests on the nozzle. The commercial valve has poppets with conical shaped ends that rest in a conical shaped area on the back of the valve orifice. A small channel separates this poppet resting area from the expansion orifice. This small channel leads to significant heating of the gas before expansion. The newly designed valve no longer has this channel. The orifice is connected to the poppet region by a knife edge (see Fig. 2.3). The conically shaped poppet no longer rests easily against the valve orifice, so the poppet now is modified so that the end of the poppet is a flat surface as opposed to the cone shape. This ensures that when the valve is closed the poppet rests flush against the orifice and produces no leaks through the nozzle.

When both of these modifications are implemented in tandem the mass spectra show an increase in intensity of midrange clusters by about 50%. A typical mass spectrum of the $IBr^-(CO_2)_n$ cluster ions with these new modifications is shown in Fig. 2.4. Clusters of usable intensities are also now present up to n = 14. The larger clusters (up to n ~18) seen in the ICl^- and I_2^- systems still are not present after the modifications. The modifications are not implemented as effectively as possible and improvements can still be made. First, the electron beam diameter is quite large at the ring magnet. Although, the electrons are focused the diameter of the electron beam is much larger than the diameter of the ring magnet. A significant portion of the electrons are not being focused into the expansion and are simply lost. The electron gun must be redesigned to provide better focusing of the beam over longer distances. Second, the new valve did not have the optimal dimensions that are desired. For maximum spatial confinement and the lowest temperature possible, the

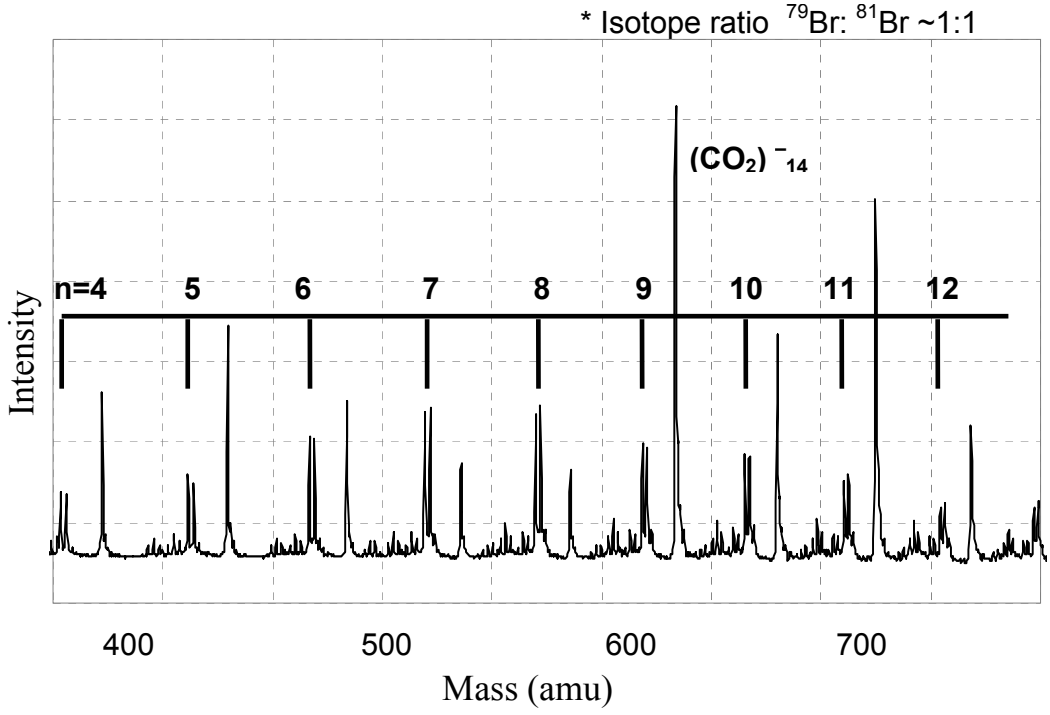

Figure 2.4: Time-of-flight mass spectrum of the midsized $IBr^-(CO_2)_n$ cluster ions, where n indicates the number of CO_2 molecules attached to IBr^-. The other prominent peaks are $(CO_2)^-_n$ cluster ions which were used as references for mass assignment.

nozzles have to be fabricated with smaller orifices (~0.1 mm) along with a larger nozzle length to orifice diameter ratio. Ratios of 20 to 30 should be more effective at producing larger clusters than the current ratio of 6.6.

2.5 Extraction, Ion Optics, and Primary Time-of-Flight Mass Spectrometer

After the ions drift for around 15 cm and cluster formation is complete, the negatively charged ions are extracted into the primary time-of-flight mass spectrometer by a transverse, pulsed electric field. The pulsed negative voltage is typically –400 to –1000 V and has an adjustable pulse width held at 2 ms. The homemade extraction plate pulser is triggered externally by a TTL pulse from a Stanford Research Systems delay generator (Model DG535) and is fed high voltage from an external power supply source. The final output is a square wave pulse at the input negative high voltage with a pulse width of 2 ms. The extraction pulse has a sharp rise time (<10 ns) and a long duration to ensure a uniform extraction field while the ions are in the extraction region. The timing of the extraction voltage pulse is optimized by observation of the ions on an oscilloscope.

The extracted ions pass through a 3 mm aperture into the acceleration region of the time-of-flight mass spectrometer. A majority of the ions in the extraction region collide with the entrance plate to the time-of-flight held at ground with only a small cylindrical volume of the anions entering the time-of-flight region. This volume is quite spatially diffuse, however, due to the diffuse character of the expansion in the extraction region. The extracted ions first enter an acceleration region that consists of 10 stainless steel rings with 2.54 cm diameter apertures each

spaced 0.43 cm apart with a 1 MΩ resistor between the two. A DC voltage of +2500 V is applied to the final plate giving the extracted ions an extra 2.5 keV of kinetic energy. A majority of the ion elements and detectors downstream of the acceleration stage are floated at the beam potential (2.5 kV).

The accelerated ions pass through a set of horizontal and vertical deflectors immediately after exiting the acceleration stage. The deflectors typically have 0 to 100 V floated above the +2.5 kV beam potential. After the deflectors, the ions enter an einzel lens that consists of three stainless steel cylinders with the first and last cylinder biased at the beam potential. The middle lens is operated in a deceleration mode with the voltage applied to this element between +800 V and +2000 V. Operation in this mode provides a much longer focal length for the anions with the focus near or at the Wiley-McLaren time-of-flight focus in the laser interaction region. The ions travel half a meter in a field free region before encountering a final set of horizontal deflectors. These deflectors usually are at 0 to 80 V above the float voltage and steer the ions through a 1.5° horizontal bend in the instrument that separates the energetic ions from metastable decay or collision induced dissociation products formed in the extraction and acceleration regions.

One of the critical aspects of working with gas phase clusters to study solvation is the ability to select specific cluster sizes on which to carry out experiments. This is accomplished by the use of a mass gate that is simply a set of horizontal, parallel stainless steel plates just before the laser interaction region. The top plate is directly connected to the floated back-end of the chamber and is constantly held at the float voltage of +2.5 kV. The bottom plate is switched between

two voltages. A DEI high voltage pulser takes two input voltages and a trigger pulse. One voltage is the float potential of +2.5 kV. The second potential is slightly below this voltage at +2.2 kV to +2.45 kV. When the mass gate is off, the bottom plate simply has the float voltage of +2.5 kV applied. In this mode of operation, all ions pass through the mass gate with no attenuation or deflection. When the mass gate is on, the bottom plate has the second lower potential on it deflecting the ions out of the path to the detectors. The DEI box pulses the potential back to the beam potential when it is provided a trigger. This allows a selected ion of a given mass to pass through unaffected. The voltage then returns to the offset voltage deflecting all other ions after the one selected. This trigger is provided from the same Stanford delay/pulse generator mentioned above.

A mass gate driver is fed two TTL trigger pulses from the delay generator. The first trigger brings the lower plate voltage down from the beam potential to the offset voltage. The driver then provides the DEI pulser a second trigger pulse with an adjustable pulse width that brings the plate back up to the beam potential for an adjustable time. This pulse width was measured to range from 58 ns to 5.6 μs. The plate is then pulsed back to the offset until the end of the cycle when it returns to the beam potential. The entire mass gate operation cycle (pulsing down to the offset voltage, back up to the beam potential for an adjustable time, and back down to the offset voltage again until the end of the cycle) is roughly constant at 275 μs in duration after receiving the initial trigger from the Stanford delay generator. The delay generator timing is adjusted until the desired ion peak appears on the scope. In the ideal mode of operation, this is the only ion mass reaching the detectors and thus

appearing on the scope. Both the trigger pulse width and the offset voltage need to be adjusted to minimize the attenuation of the mass-selected peak in conjunction with allowing a minimum amount of neighboring ion masses to get through. It is found that an offset voltage of around 200 V provides enough deflection to minimize both background noise at the detector and attenuation of the mass selected ion. Offset voltages of more than 300 V provides efficient minimization of noise, but begin to distort and attenuate the parent ion. Pulse widths of around 600 to 800 ns provide the smallest window where no attenuation or distortion was observed. The mass gate is surrounded by an enclosure with entrance and exit apertures. The entrance aperture diameter is 2.5 mm while the exit is 4.3 mm. These are easily removed if there is a change in the ion trajectory leading to scattering from either aperture plate. The entrance and exits have diameters of 9.2 mm when the apertures are absent. The entire assembly is on threaded rods by which the height can be adjusted in case of changes in the ion trajectories.

2.6 Photolysis, Secondary Mass Spectrometer, and Detectors

The ions arrive at the spatial focus of the primary time-of-flight mass spectrometer just after exiting the mass gate. Extensive work was done in the design of the instrument to determine the dimensions and voltages necessary for the spatial focus of the time-of-flight to be precisely at the laser interaction region.[4] The mass selected ions are intersected perpendicularly by the laser beam about 6 cm after the exit of the mass gate. Upon photolysis, the parent ion and any photofragment ions produced enter the secondary time-of-flight mass spectrometer. This spectrometer is

a single stage, reflectron mass spectrometer[15,16] at an initially designed tilt angle of 2.5°. The reflectron consists of 30 equally spaced plates connected by 10 MΩ resistors. The front of the reflectron has both the entrance and exit apertures and is held at the beam potential of +2.5 kV. The back plate is held at a variable voltage that is discussed below. The entrance aperture is collinear with the entrance and exit apertures of the mass gate. The back plate also contains an exit aperture to allow ions to travel directly through the reflectron to the in-line detector when desired.

The voltage applied to the back plate of the reflectron reverses the trajectory of an ion when the energy of the retarding field exceeds the kinetic energy of the ion. This field separates ions according to their mass as well as focuses them onto the off-axis detector located after the exit of the reflectron. There is an inherent energy spread in the ion beam of about ±500 V. The distance that an ion penetrates into the reflectron depends on its kinetic energy. Focusing of the ions is achieved due to the fact that ions of the same mass and spatial position, but with different energies penetrate to different depths in the reflectron. The higher energy ions penetrate further and thus have a longer flight time through the reflectron to the off-axis detector. However, in the field free region after the reflectron the more energetic ions overtake the slower, less energetic ions. The point where this takes place is the spatial focus of the reflectron where the off-axis detector is positioned.

The advantage of the reflectron is that desired ionic fragments of a mass-selected, photofragmented parent ion are focused onto the off-axis detector by simply varying the voltage applied to the back plate of the reflectron. The position of the spatial focus depends on the mass of the ionic fragments for a fixed reflectron field.

The voltage applied to the back plate must be adjusted to move the spatial focus of a fragment ion to that of its parent ion, which is located at the off-axis detector. The voltage that is applied is proportional to the ratio of the mass of the fragment ion, m_f, to the mass of the parent ion, m_p. The reflectron voltage, V_R, is given by:

$$V_R = \frac{4D}{L}\frac{m_f}{m_p}\frac{E_P}{e\cos(\theta)} \tag{2.1}$$

where m_f and m_p are the masses of the fragment and parent ions, E_p is the energy of the parent ion, θ is the tilt angle of the reflectron, L is the free field drift region distance, and D is the percentage of penetration into the reflectron. There are two variables in Eq. 2.1 with all others assumed to be constant for this particular apparatus. The masses of the fragment and parent ions are the variables to be entered from which the voltage applied to the reflectron is given. This is the voltage that focuses the fragment onto the off-axis detector at the same flight time as the parent ion. It had been assumed in previous experiments that the optimal penetration depth for the best focusing and most intense ions on the off-axis detector was 0.86. This penetration depth corresponds to a reflectron voltage to focus all of the parent ions onto the off-axis detector of –988 V. However, it was found that the optimized ions are at reflectron voltages other than the voltage previously used. When the parent ions are optimized, it is critical that the reflectron voltage is varied to obtain the most intense, focused parent ions. The reflectron voltage that must be applied varies daily, sometimes over hundreds of volts meaning that the penetration depth is varying. The

prior method of assuming a penetration depth of 0.86 when optimizing the parent ions and calculating voltages for the fragment ions is inaccurate.

The reflectron voltages for the fragment ions are now found by first determining the reflectron voltage necessary to produce the most intense, focused parent ions. From this voltage, the penetration depth was determined by simply taking the average parent ion kinetic energy divided by the reflectron voltage. The average parent kinetic energy is found by taking half of the extraction voltage and adding it to the float voltage of +2.5 kV. The reflectron voltage is 2500 V – (voltage on the reflectron power supply). For instance, if the voltage supplied is –850 V the reflectron voltage is 2500 – (–850) or 3350 V. For an extraction voltage of 500 V, the penetration depth is 0.82. The voltage necessary to focus a fragment of a given mass from a parent ion is now calculated by entering the extraction voltage, the penetration depth, and the masses of the parent and fragment ions. These calculations provide the correct reflectron settings when changes in the extraction voltage and the penetration depth occur.

The instrument has two detectors with one in-line behind the reflectron on the ion axis and the other off-axis after the exit of the reflectron. Only a brief discussion of the configuration in the floated regime is given here with a full description of the detectors and their circuit diagrams when floated found elsewhere.[4] The in-line detector consists of two microchannel plates (Hamamatsu Corp. F4612-09 and Burle part #32733) that are impedance matched and in a "Chevron" configuration. This arrangement provides a gain of around 10^7. Each plate has a 20 mm active area. In the floated configuration of the detector, the front plate was biased at the beam

potential of +2.5 kV. The back plate is biased at 1.6 kV above the beam potential when detecting parent ions and usually 1.8–1.9 kV for detecting less intense photoproducts with a maximum permitted voltage of 2.0 kV above the float potential across the plates. There is a mesh held at the beam potential in front of the first plate to provide a flat, field free potential for the ions and can be used as an acceleration stage if desired. A vertical deflector is also used to steer the ions into the detector. It typically has a few hundred volts above the beam potential for maximum ion signal at the in-line detector. It is also used to deflect the negative ions away from the detector for the detection of neutrals. In this case, the plate is biased at 1.0–1.5 kV above the beam potential. The electrons from the microchannel plates (MCPs) are collected by an anode that is biased at +200 V above the voltage of the last plate. This voltage is regulated by a Zener diode that maintains this +200 V between the anode and last plate as the voltage on the last plate is varied. The ion signal is capacitively coupled to the data processing electronics due to the detector being biased at high voltages. The signal from the anode is amplified by a factor of 10 by a pre-amplifier (EG&G 9301) and is then further amplified by a Stanford Research Systems 350 MHz fast pre-amplifier (SR 240A) that provides a gain of up to 625 before finally being sent to the data processing electronics.

The off-axis detector is located at the spatial focus of the reflectron about 38 cm from the reflectron exit. This detector consists of three microchannel plates (Galileo, 0.70″ active area diameter). The first two are impedance matched in a Chevron configuration. The third plate is not impedance matched and is at an orientation of 180° with respect to the second plate. The overall gain is roughly 10^{10}.

The detector is floated at the beam potential of +2.5 kV. A potential of around 2.1 kV above the float potential is applied to the back of the third MCP for the detection of parent ions. A potential of 2.5–2.6 kV is applied for the less intense one-photon ionic photoproducts with 2.8–2.9 kV applied for the typically smaller two-photon ionic products. The anode is biased +200 V above the potential of the back plate by use of a Zener diode in the same manner as the in-line detector. The ion signal is capacitively coupled to the detector electronics and is amplified by an identical pre-amplifier as the in-line detector.

As with the in-line detector, the off-axis detector has a mesh held at the beam potential which is 96% transmissive. After this there is an electron filter that is simply a grid that is at –200 V to discriminate against any stray, low energy electrons from hitting the detector. This filter is quite useful when ion production is difficult. The filter can be turned off to allow the low energy electrons to strike the detector. These low energy electrons typically depend on the same conditions as the ions when present. The conditions for maximum electron signal on the detector are usually very close to the conditions for ion production. The filter is turned on and the parent ion signal can be found. After the electron filter, there is post-acceleration stack. This stack was designed to provide the ions with an additional 1 to 3 keV kinetic energy before striking the detector. However, it was determined that this stack is responsible for a great deal of noise on the detectors, especially noticeable when operating in the single ion counting (two-photon experiments) regime. Although, the stack does increase the intensity of the parents the added noise made the use of it undesirable. The stack is now kept at the float potential making the added noise negligible.

2.7 Photoelectron Imaging Considerations and Potential Switch

There are two major design concerns that were considered when implementing the electron velocity map imaging system as described in the Introduction. The first is that the imaging system can not be held at a large potential. The detector region and all the components in electrical contact with the imaging system can no longer be floated at the existing 2.5 kV beam potential. The second concern is that the electron imaging apparatus needs to be designed such that it can be installed into the pre-existing tandem time-of-flight/reflectron mass spectrometer system. Full functionality of the Wiley-McLaren time-of-flight and reflectron mass spectrometers as well as the two detectors needs to be retained with minimal modifications.

The first task is to reference components that were previously floated at +2.5 kV to ground, which in this case is the detection chamber ground. Accelerated ions are still desirable, but they need to be referenced to ground after the acceleration region in a way in which no potential force is felt when encountering the grounded portions of the apparatus. This is accomplished by the use of a potential switch[17] pioneered by the Johnson group. The potential switch is a region that is electrically isolated from the other components of the instrument. Initially, it is held at the beam potential of 2.5 kV. When the accelerated anions of interest enter the switch, the potential applied to the region is quickly switched down to the chamber ground. The ions continue to have 2.5 keV of kinetic energy, but now are referenced to ground making floating the reflectron and detectors region unnecessary.

The switch itself is composed of existing hardware in the time-of-flight chamber. A cylindrical mesh previously connected directly to the acceleration and ion optics stack, is now electrically isolated by a Teflon ring and Vespel screws. Near the beginning of the mesh cylinder (close to the exit of the ion optics stack) there is a stainless steel circular plate with a 1″ aperture in the center. The other end of the mesh is in electrical contact with the moveable stainless steel cylinder housing the aperture between the second and third differential pumping regions and the 1.5º bend deflectors. After the deflector region, there is another cylindrical mesh in electrical contact with the moveable cylinder that forms the last portion of the switch. The end of this mesh is capped with a circular stainless steel plate with a 1″ aperture in the center. The two end plates with the 1″ apertures define the total length of the potential switch. The apertures are in place to keep potential fields from other parts of the instrument from penetrating into the switch. It is desirable to have the switch as long as possible to allow for larger ranges of masses to be present in the switch at a given time to facilitate peak assignments. The switch in this case is 70 cm allowing for a range of 65–70 amu of focused ions. This range is actually a bit wider, but ions on the edge of the switch tend to be distorted and not used in experiments.

A problem with the potential switch arranged in this manner is that the 1.5º bend deflectors are within the switch. These deflectors are electrically isolated from the switch and float at voltages different from the switch potential. This effectively halved the length in which the switch performed properly with the effective length now from the first stainless steel plate aperture to the aperture separating acceleration region from the region with the bend deflectors. This problem is remedied by

completely removing the deflectors from this region. A cylindrical section of the chamber is removed between the detection chamber gate valve and the end of the switch and fitted with a new set of deflectors. Electrical SHV feed-throughs were added on both sides of the cylinder to provide the electrical connection to the deflectors from the power supplies. A final modification to the system was placing a stainless steel plate with a 1″ aperture and tabs to hold it in place just after the detection region gate valve to provide differential pumping between the third pumping region and the detector region.

The potential switch voltage is pulsed by a DEI PVX-4140 Pulse Generator. This pulse generator takes two voltage inputs with one from a power supply set to the beam potential (2.5 kV in this case) and the other input is connected directly to the backend of the chamber (ground). A TTL trigger pulse from a Stanford Delay Generator is sent to a homemade DEI controller box. This allows the trigger pulse sent to the DEI pulser to be adjustable in width from 30 ns to 13 ms. The switch is turned on when the trigger pulse is sent to the pulser. This trigger is set to coincide with the triggering of the extraction plate. The length of the trigger pulse is varied in width to allow a larger mass range to be present in the switch. The pulse width to cleanly include masses of up to around 70 amu is 13 μs. The rise and fall time of the switch pulse is 15 ns.

2.8 Electron Imaging Stack Design and Installation Concerns

In addition to the implementation of the potential switch, the other major challenge of the design of the electron imaging system is to incorporate the hardware

of the imager into the existing apparatus in a way such that none of the original functionality of the time-of-flight and reflectron mass spectrometer instrument is compromised. The only suitable location for the electron imaging hardware is vertically in the region between the mass gate and the reflectron. However, it needs to be carried out in such a way that the parent ion and ionic fragment flight paths through the mass gate to the reflectron entrance and from the reflectron exit to the off-axis detector remained unobstructed.

A generalized schematic of this electron imaging system along with the potential switch installed in the existing system is shown in Fig 2.5. The distances and sizes are not to scale. Exact dimensions are given below. As mentioned above, the electron imaging system follows the velocity map imaging design[2] of Eppink and Parker. In their configuration, a repeller plate with a small 1 mm hole is used followed by an extractor and a ground plate. Both of these plates have open apertures of 20 mm. The imaging system described here has a slightly different electrode configuration based on the Sanov group imaging apparatus.[18] The photodetached electrons after extraction pass through a field free flight tube before striking a microchannel plate detector. The electrons from the microchannel plates impinge on a phosphor screen that is then imaged by a CCD camera. The electron imaging stage must be shielded from stray magnetic fields as well as having accurately timed voltage pulses applied to various elements of the imaging system.

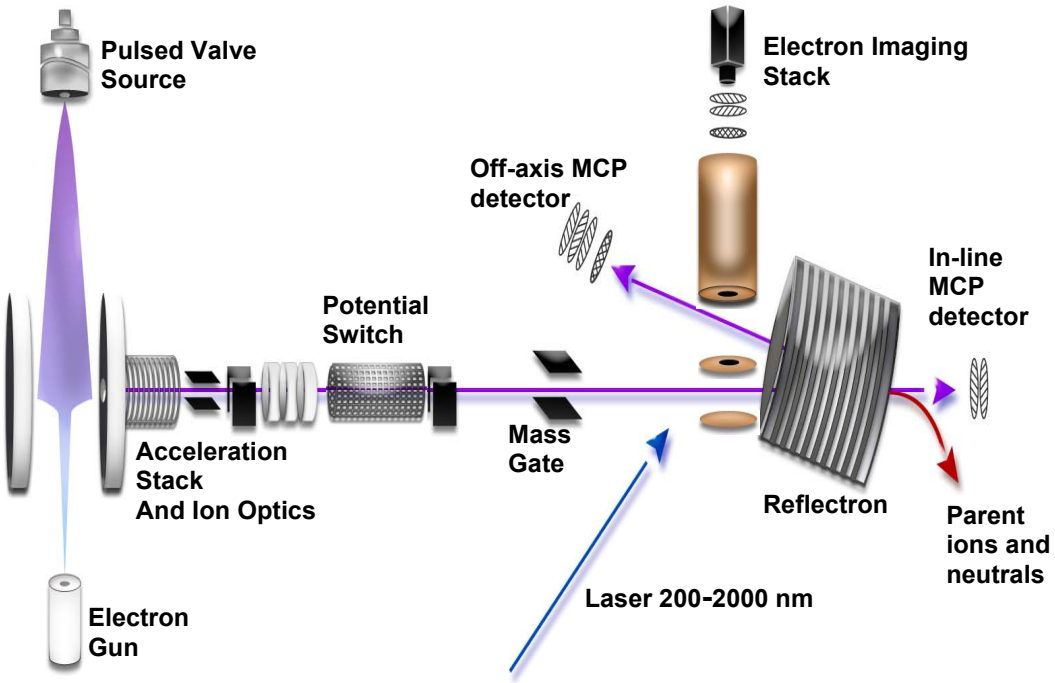

Figure 2.5: Cluster ion source and tandem time-of-flight mass spectrometer with potential switch and electron velocity map imaging components.

2.9 Electron Imaging Optics and Flight Tube

The electron extraction and imaging optics consist of three plates made of oxygen-free high-conductivity copper. The plates are 3″ in diameter and 0.03″ in thickness. The bottom plate (repeller) is solid with the ground and extractor plates having a 1″ aperture in the center of each. The plates are spaced 1″ apart and are held in place by threaded Molybdenum rods and ceramic washers to electrically insulate them from the grounded rods. The plates are connected to power supplies via insulated wires. The flight tube is made of oxygen-free high-conductivity copper and is 15 cm long with a 2.75″ diameter. The flight tube is in direct electrical contact with the final electrode plate and the two are held at the same potential. The entire assembly is mounted onto an 8″ conflat flange containing electrical feed-throughs for the voltage connections.

The low energy electrons formed from photodetachment are susceptible to the Earth's magnetic field along with any other stray magnetic fields. For this reason, the electron optics and flight tube assembly is enclosed with magnetic shielding. The shielding is μ-metal (Magnetic Shielding Corp.) and consists of four layers of 0.020″ thickness covering the entire length of the inside of the flight tube. The extraction plates are covered by a μ-metal cup that is fastened to the flight tube via a Teflon ring to isolate it from the flight tube. The cup contains openings to allow for the parent ions, laser beam, and fragment ions exiting the reflectron to the off-axis detector to pass through unperturbed. The openings were designed to be as small as possible to minimize field penetration into the extraction region [penetration $\propto$(diameter)^2], but to still allow for unobstructed ion trajectory paths. The laser openings on each side

are 0.5″. The entrance and exits on the front side are roughly 1 cm and the back consists of a long slit about 1 cm wide and 3″ long. There is also a 1″ opening on the bottom of the cup for pumping purposes. The assembly is illustrated in Fig. 2.6.

As mentioned before, the entire assembly needed to be installed in the existing chamber with minimal modifications. The assembly is mounted on an existing 8″ flange directly above the laser interaction region of the chamber. The mass gate previously was positioned on the middle of a 6″ flange that is just before the laser interaction region. For the new assembly to be accommodated, the mass gate is moved 1.5″ away from the center of the flange in the direction of the source region. The side view of the chamber with the electron imaging system installed is shown in Fig. 2.7.

2.10 Imaging Detector and CCD Camera

The imaging detector consists of two microchannel plates (MCP) and a phosphor screen mounted onto a 6″ flange with the electrical feed-throughs that itself mounts onto the 8″ electron flight tube flange. The entire detector assembly was shipped as one component from Burle Electro-Optics, Inc. The MCPs are impedance matched in a chevron configuration. The plates have a 40 mm active area and a minimum gain of 4000 for each plate at +1000 V. The front plate is held at the flight tube potential while the back plate is at +1600 V above the front plate. The back plate is pulsed between +1600 V and +1900 V. The plates have the larger voltage across them when the photoelectrons are arriving at the detector. Pulsing the plates down to the lower voltage minimizes the background of stray electrons and ions

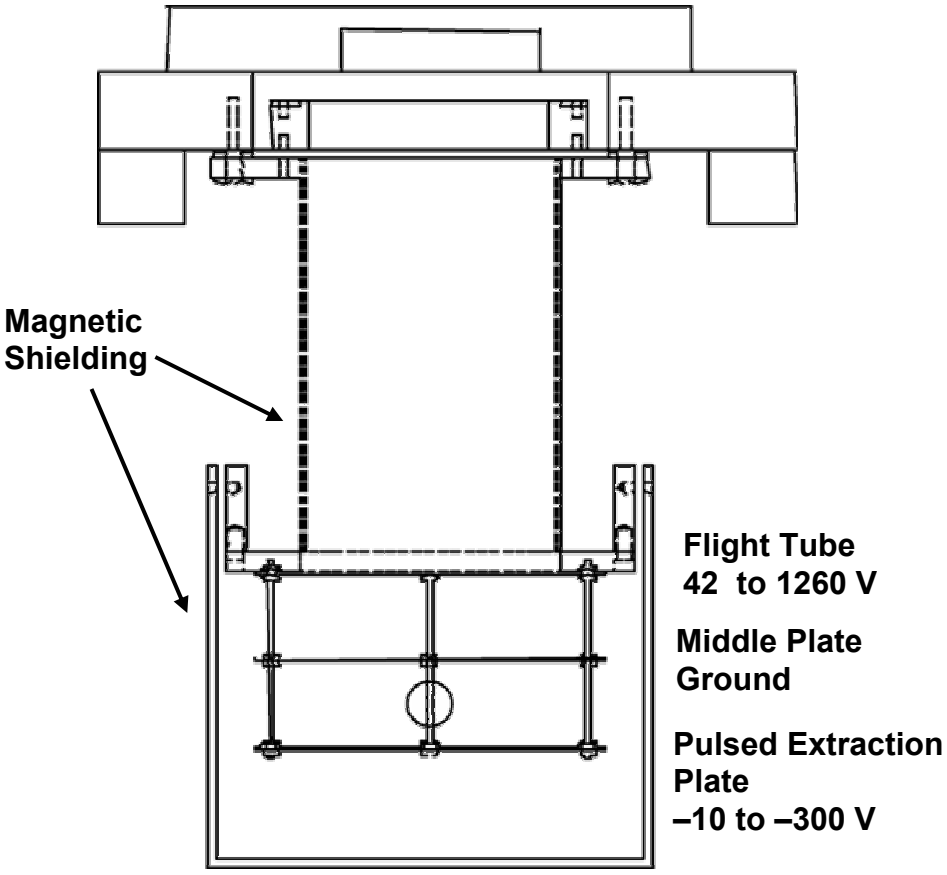

Figure 2.6: Electron velocity map imaging schematic. Exact dimensions and distances are given in text.

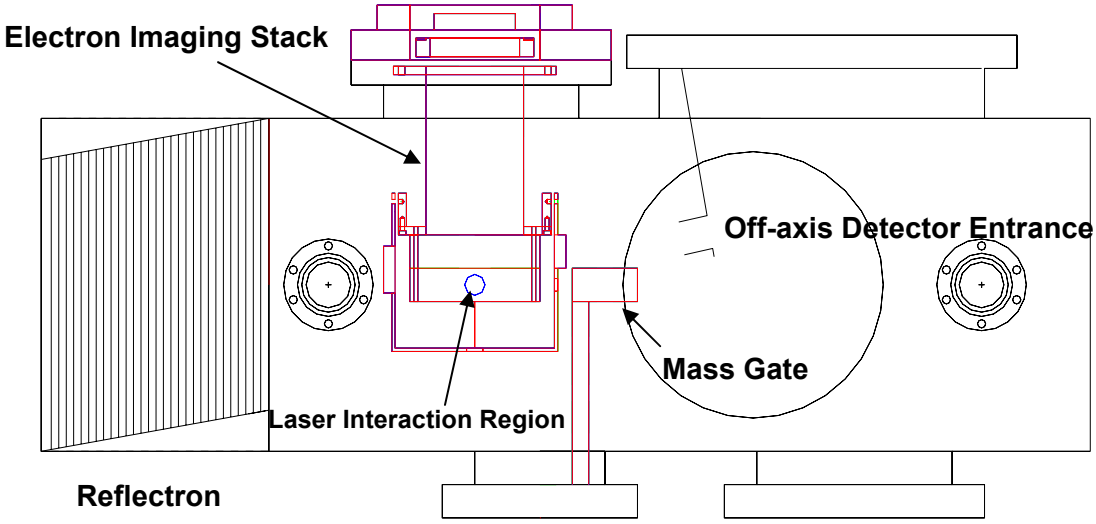

Figure 2.7: Side view of the chamber with the Imaging stack installed. Components in red are either new or in a modified position compared to the original design in black.

arriving at the detector when the photoelectrons are not present. The phosphor screen is a P47 type and is electrically isolated from the MCPs and the chamber ground. The screen is at held at around +6 kV and is not pulsed.

The pulsed voltages are provided by homemade controllers similar to that of the potential switch mentioned above. The pulsed extraction plate voltage is provided from a DEI PVM-4210 model dual output pulser module. The pulser provides adjustable positive and negative voltages. In the imaging experiments described within, the typical voltages are between −10 and −100 V. The pulser module receives a trigger of adjustable width from the homemade DEI pulser controllers. This controller takes a TTL trigger provided from the Stanford delay generator and sends it to the DEI module with an adjustable width. The extraction plate pulse is set to be 50 μs wide and pulses between chamber ground and the desired negative voltage set on the module itself. The MCPs are likewise pulsed by a DEI PVM-4140 pulser. However, this module takes not only a trigger pulse, but also two input voltages to switch between. The input voltages are provided by two external power supplies and the trigger pulse is produced in an analogous manner as the extraction plate from an input TTL pulse. The MCP pulse is 200 ns wide and pulses the back plate between +1600 and +1900 V. Both the front MCP plate and the flight tube are held at their voltages in DC mode by external power supplies. The exact timing of the pulsed voltages is discussed below.

The CCD camera is a La Vision 3LS model. It has a spectral range of 290−1000 nm that includes the peak wavelength of the P47 phosphor of 410 nm. The physical dimensions are 1280 x 1024 pixels with an individual pixel size of 6.7 μm x

6.7 μm. The exposure time can be varied between 1 and 100,000 ms with a read-out time of 121 ms. The camera is linked to the PCI-Interface Board by a 10 m fiber optic cable. Within the camera head is a 12 Bit A/D along with a parallel/serial converter for serial data transfer to the interface board. The CCD is Peltier cooled to a normal operating temperature of –11 ºC. The camera has a Nikon 12 x 24 mm wide angle lens. The entire camera is mounted onto a height adjustable mount which is fastened to the 6″ detector flange. A black metal cylinder is placed between the phosphor screen and the lens along with a black drape over the entire camera assembly to limit stray light impinging on the CCD that leads to higher background counts.

2.11 Laser Systems and Timing Schemes

2.11.1 Nanosecond Laser System

For one-photon experiments a nanosecond laser system is used. This system consists of a commercial Nd:YAG pumped optical parametric oscillator (OPO). The laser is a Coherent Infinity with a Coherent XPO and a 2nd harmonic generation stage and is depicted in Fig. 2.8. The entire XPO and doubling assembly of the Infinity provides a wavelength range of 210–2000 nm at pulse energies of 100 μJ–600 mJ with a continuously adjustable repetition rate of 0.1–100 Hz.

The initial pulse is formed by a diode-pumped Nd:YAG prism inside a ring resonator. The cavity is Q-switched by use of an acousto-optic modulator (AOM) within the oscillator cavity.[19] The low energy pulses from this oscillator are then amplified by use of Xenon flashlamp pumped Nd:YAG rods. There are two trigger

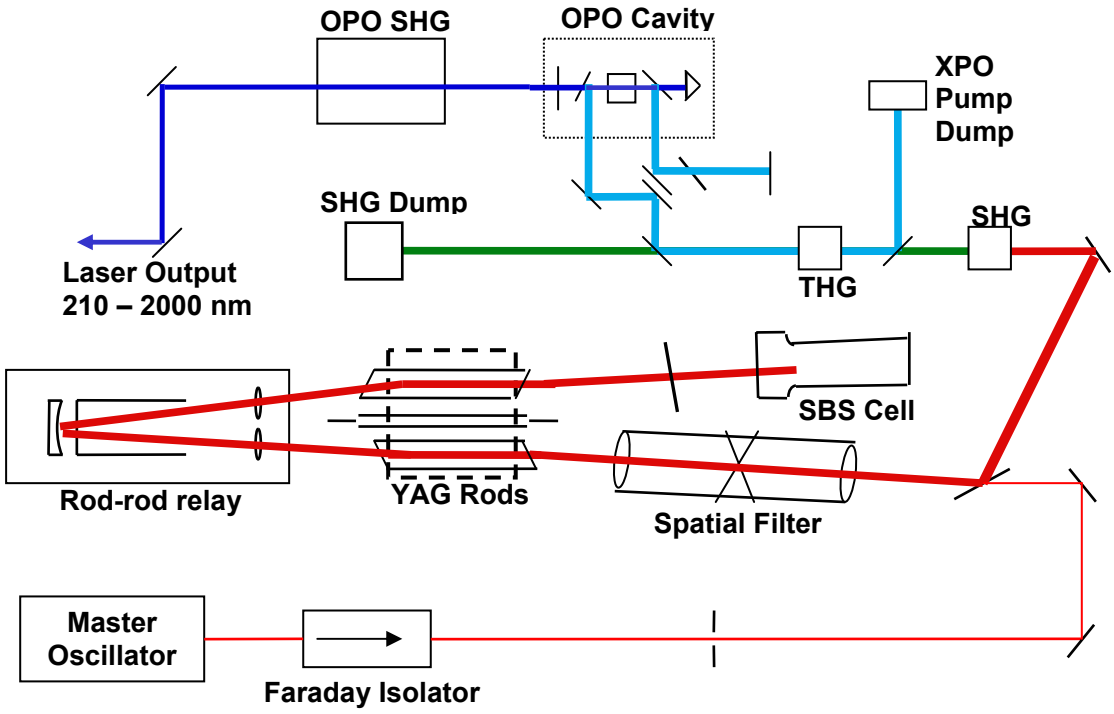

Figure 2.8: Nanosecond Nd:YAG-pumped OPO laser schematic.

timings involved in this laser that must be coordinated in any combination of external and internally triggered. The timing between the Q-switch and the firing of the flashlamp is optimized by observing the power of the fundamental pulse as a function of this delay between the two. The optimized timing has the Q-switch being triggered around 250 μs after the flashlamp is triggered. This value is used when developing experimental timing sequences described below. The pulses make two passes through each of the two Nd:YAG rods that are designed to ensure a pure polarization state and are then reflected out of the amplifier by a thin film polarizer.

The fundamental pulse (1064 nm) exits the amplifier with vertical polarization and up to 600 mJ/pulse in energy. The pulse width of the amplified pulse is 3 ns. The fundamental pulse undergoes type I doubling in an angle tuned BBO crystal to produce frequency doubled light at 532 nm. The fundamental and 2^{nd} harmonic pulses are then mixed in another angle tuned BBO crystal to produce the 3^{rd} harmonic of the fundamental at 355 nm. The fundamental, 2^{nd}, and 3^{rd} harmonics are separated from one another using dichroic mirrors allowing for the use of the three colors for experiments.

The XPO stage is an optical parametric oscillator (OPO) placed in the Infinity laser and is pumped by the 3^{rd} harmonic light. The 3^{rd} harmonic pump pulse is introduced into a cavity with a nonlinear BBO crystal as the gain medium. The production of the tunable light from the pump pulse is a result of difference frequency mixing.[20] Due to noise in the cavity there is a cavity resonant beam present at low intensity of a frequency lower than the pump called the signal, ω_s. This frequency interacts with the pump frequency, ω_p. The interaction of these two frequencies

produces a new frequency called the idler at ω_i. This new frequency quickly grows in intensity and can itself interact with the pump frequency to produce a difference frequency at the original signal frequency. In this way, both the signal and the idler are amplified within the cavity at the expense of the pump beam. The overall process is then $\omega_p = \omega_s + \omega_i$ with the pump photons converted into the signal and idler photons. A phase matching condition must be met for the optical parametric oscillator to provide gain for the signal and idler frequencies. The equation $k_p = k_s + k_i$ must hold where k represents the wavevector of each frequency that depends on the index of refraction of the frequency in the BBO. The crystal is birefringent meaning that the indices of refraction in the crystal change as the crystal angle is changed. As the crystal angle is changed, the phase matching condition is met by a new set of signal and idler frequencies. The tunability of the OPO thus arises from varying the crystal angle to allow different sets of signal and idler frequencies to meet the phase matching condition necessary for oscillation.

The cavity is set up to be singly resonant in which only the signal or only the idler can form the output pulse. Selection of either the idler or the signal can easily be accomplished by the use of different sets of optics in the XPO cavity. There is a narrow wavelength region that is inaccessible around the point where the signal and idler are degenerate in energy (709.4 nm). The degeneracy gap has been measured to be roughly from 690–730 nm. The signal tuning range is then 420 nm–690 nm and the idler range is 740–2200 nm. Output pulse energies in the range of 1–20 mJ for the signal are observed with the pulses becoming broader in width from typically 3 ns to about 6 ns as the wavelengths approach the degeneracy gap. The idler wavelengths

have pulse energies below 1 mJ with somewhat broader pulse widths than the signal wavelengths. The final element to the Infinity-XPO is a 2nd harmonic generation assembly employing another BBO crystal to produce the doubled frequencies of either the signal or the idler. There is a gap in the wavelengths between 345–365 nm reflecting the degeneracy gap in the OPO wavelengths to be doubled.

The velocity map imaging experiments require the laser polarization to be horizontal with respect to the ion flight axis. The light coming out of the Infinity-XPO has polarizations dependent on whether the signal, idler, or the doubled signal/idler is used. In some cases, the polarization must be rotated 90° before interaction with the ions. This is simply accomplished by the use of two mirrors in a periscope arrangement. The input polarization is retained upon exiting the periscope when the two mirrors have their axes parallel to one another. The polarization is rotated 90°, however, if the mirror axes are 90° apart. The polarization is then changed from vertical to horizontal or vice versa by simply changing the periscope arrangement. This allows for polarization changes easily over broad wavelength ranges without the need for wavelength specific wave plates. Also, in the optical path is a telescope that consists of a 50 cm focal length lens followed by a –20 cm focal length lens that is placed within the focus of the first lens. This telescope serves to collimate the beam as it enters the chamber. This is especially important for the idler beam that has a very large divergence in the far field. A polarizer is used after the telescope to ensure a pure polarization state and various lenses are used after this for tighter focusing inside the chamber. Broadband aluminum mirrors (Thorlabs, Inc.) with a range of 200–1000 nm were used to avoid switching out mirrors when varying

the wavelength drastically. One final consideration for the nanosecond laser system is the fact that numerous components within the electronic imaging stack contain copper that has a work function of 4.7 eV (267 nm). Using wavelengths below this threshold produces a great deal of electrons ejected from the copper surfaces leading to a much higher background in the images. To overcome this, the entrance and exit window flanges on the chamber were extended on each side by about 7.5″. On each side in the extended regions, three annuluses were inserted with apertures of decreasing diameter. This serves to block scattered UV light from reaching the copper components thus minimizing background at the detector. Brewster windows were also installed on the entrance and exits sides cut at 56.44° for 250 nm. This minimizes scattering from the windows and is effective over a broad wavelength range. The Brewster's angle for 200 nm to 800 nm only changes by 2°.

2.11.2 Femtosecond Laser System

The femtosecond laser system generates short pulses for use in the time-resolved pump-probe experiments described below. A schematic of the overall system is shown in Fig. 2.9. The femtosecond pulses are generated by a Coherent Mira Ti:Sapphire oscillator. The Mira is pumped by a Coherent Verdi diode-pumped Nd:YVO_4 laser producing 5.5 W cw at 532 nm. The Mira produces modelocked femtosecond pulses at wavelengths tunable between 750–850 nm. The repetition rate of the laser is 76 MHz and is determined by the round-trip time of a pulse from one end of the Mira cavity to the other. The laser uses the technique of passive modelocking via the optical Kerr effect.[19] The wavelength is varied by tuning a

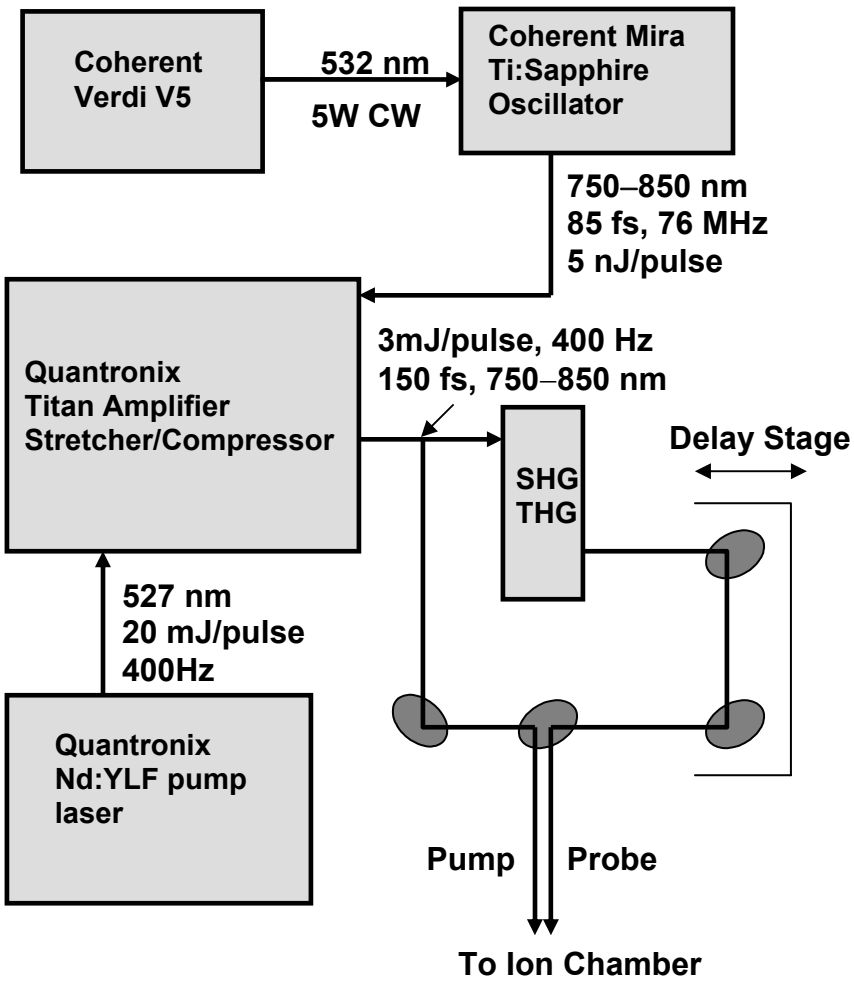

Figure 2.9: Femtosecond laser system for pump-probe experiments.

birefringent filter and monitoring the wavelength with an Ocean Optics spectrometer. The pulse width of the new center wavelength is then minimized by the adjustment of a Brewster prism to compensate for any group velocity dispersion incurred by elements within the cavity or by self-phase modulation of the pulse. Optimized pulse widths tend to be 10 or 12 nm on the spectrometer corresponding to around 85 fs. However, the pulse energies are only 5−10 nJ and need to be amplified for use in the pump-probe experiments. A photodiode is placed behind a mirror outside the Mira to serve as a trigger for the amplification stage.

The output pulses of the Mira enter a Quantronix Titan amplifier that consists of a stretcher and compressor along with a regenerative amplifier[21] and a multipass amplifier. The input pulses are first stretched out to a few hundred picoseconds and are sent into a regenerative amplifier. The leakage from the mirror just after the Mira triggers a Medox Pockels Cell driver. This driver serves numerous purposes in the laser system. First, it divides the 76 MHz repetition rate of the Mira down to 400 Hz. A trigger at 400 Hz is then provided to the Q-switch of the pump laser for the amplifier. The Medox driver also controls when the stretched pulse is injected into the regenerative amplifier and when it is switched out by providing a time-dependent voltage for a Pockels cell within the regenerative cavity. Finally, it provides an external trigger for the clusters experiments that is discussed below. When a voltage is applied to the Pockels cell it rotates the polarization of the laser pulse 90°. This is combined with a thin-film polarizer to control when the pulse is injected into the cavity and switched out. The timing of this process is determined by observing the intensity build up of the pulse in the regenerative amplifier cavity on an oscilloscope

monitoring leakage from an end mirror of the cavity onto a photodiode. The amplification medium is a Ti:Sapphire crystal that is pumped by a Q-switched Quantronix Nd:YLF laser with a 400 Hz repetition rate. The power upon exiting the regenerative amplifier is around 800 mW.

The pulse is then further amplified by a multipass amplifier that consists of another Ti:Sapphire crystal pumped by the same Nd:YLF laser. The Nd:YLF light is split upon entering the Titan between the regenerative and multipass amplifiers. The pulses make two passes through the second amplifier and exit with a power of 1.8 W. The pulses are then recompressed using another grating pair to introduce group velocity dispersion of the opposite sign introduced in the stretcher stage. This compression depends primarily on the distance between the two gratings. The pulse width is measured by an autocorrelator and is minimized by adjusting the grating distance while monitoring the autocorrelation trace. The optimized output pulse is 150–200 fs in width with a power of 1.2 W corresponding to 3 mJ/pulse at 400 Hz. Losses in the compressor account for the drop in power from 1.8 W.

The output of the Titan is split into a pump and a probe pulse with a 50:50 beam splitter. For one-color experiments, the two identical beams are sent on two separate optical paths. For two-color experiments, the 2^{nd} harmonic of the fundamental is generated by placing a KDP crystal in one of the optical paths. In both one- and two-color experiments, a computer-controlled delay stage was inserted into one of the beam paths chosen to be the probe pulse path. The time-delay between when the pump and the probe pulse arrive at the ion packet is controlled by changing the relative path length difference between the two optical paths. The delay

stage provides delays within a tenth of a picosecond with a maximum delay of ±200 ps. The paths are designed to be nearly identical in total length with the picosecond delays then added by moving the delay stage millimeters (1 mm difference in path length distance corresponds to a delay of 3 ps between the two pulses). For the long time delays experiments described below, the delay stage is not used. The long delays are set by manually changing the length of one optical path with respect to the other.

The two beams are recombined in the one-color experiment by use of a polarizing beam splitter cube. The two beams are identical and thus have the same polarization. The polarization of one of the beams is rotated 90° by use of a wave plate. The polarizing beam splitter is then oriented to allow one beam pass straight through and the other beam of the opposite polarization to be reflected at a 90° angle. In this manner, the two beams of now horizontal and vertical polarizations are recombined collinearly. A 1m lens is used for mild focusing of the beams inside the chamber. The pump and the probe beams for the two-color experiments (typically near 800 nm and 400 nm) are recombined by simply using a mirror just before the chamber that reflects one color and passes the other color straight through from behind. This allows the two beams to be collinearly recombined with any combination of horizontal or vertical polarizations.

The accurate determination of zero time delay between the pump and the probe beams is critical for carrying out the time resolved experiments. For one-color experiments, the zero delay between the two beams is determined by the appearance of an interference pattern when the two beams are slightly misaligned with respect to

one another. The delay stage is moved until the interference pattern appears. The delay time usually needs to be accurate to one or two tenths of a picosecond for the most prominent interference pattern. The delay stage is then reset to have this newly determined position read as zero time delay. For the fundamental and second harmonic beams, time zero is determined by the appearance of the third harmonic of the fundamental. This is accomplished by mixing the pump and the probe beams in a KDP crystal followed by a prism to separate the colors. The delay stage is moved until the third harmonic appears. Fine adjustments are made until the third harmonic intensity is maximized which occurs when the pump and probe are overlapped exactly in time. This represents time zero outside of the chamber. The two colors have different travel times through the laser window on the chamber. The time zero inside the chamber is previously measured to be 0.95 ps less than time zero outside the chamber. The delay stage is then moved by this amount and reset as time zero.

2.11.3 Nanosecond Timing and Data Collection Schemes

The Infinity laser system is used for one-photon experiments to determine relative and absolute cross sections as well as ionic cluster branching ratios. The timing scheme is designed to ensure that the mass-selected ion packet arrives at the laser interaction region at the precise time the laser pulse does. The Infinity laser has two triggers with one for the flashlamp and the other for the Q-switch. The flashlamp and the Q-switch can be triggered in any combination of external or internal. The first triggering scheme involves triggering both the flashlamp and Q-switch externally from the SRS DG 535 Delay Generator with TTL pulses at 50Ω impedance. The

overall scheme including ion events is as follows and is shown schematically in Fig. 2.10 with an actual set of timings shown for reference. The delay generator is internally triggered at 80 Hz. The T_o output is used to trigger the pulsed valve and represents time zero for each ion production cycle. The A delay triggers the extraction plate and is typically set to be around T_o + 1 ms where 1 ms represents the flight time of the cluster ions from the valve to the extraction region. The B delay turns the mass gate on and is equal to A + x where x is the flight time of the ions from the extraction region to the mass gate. The timing, x, is adjusted to mass select a desired parent ion as monitored on the scope. The C delay triggers the flashlamp and the D delay triggers the Q-switch. As mentioned before, the timing between the flashlamp and the Q-switch was optimized by measuring the output power of the Infinity. This value is represented in the D delay, which in this case is D = C + 251.6 μs and remains fixed. This delay may need to be periodically re-optimized, but does not change throughout the course of experiments. The C delay is the delay used to overlap the laser pulse with the ion packet and is calculated as follows. It is assumed that when the Q-switch is triggered, the laser pulse is instantaneously at the ion packet interaction position. The flight time of the ions from the extraction region to the mass gate is known from the mass gate timing. There is an added flight time, Δ, that represents the short flight time from the mass gate to the laser interaction region. The flashlamp and Q-switch have a fixed delay, in this case, of 251.6 μs, which is much longer than the flight time of the ions from the extraction region to the laser interaction region. The flashlamp must be triggered some time before the ions are extracted to ensure the Q-switch fires when the ions are at the interaction region.

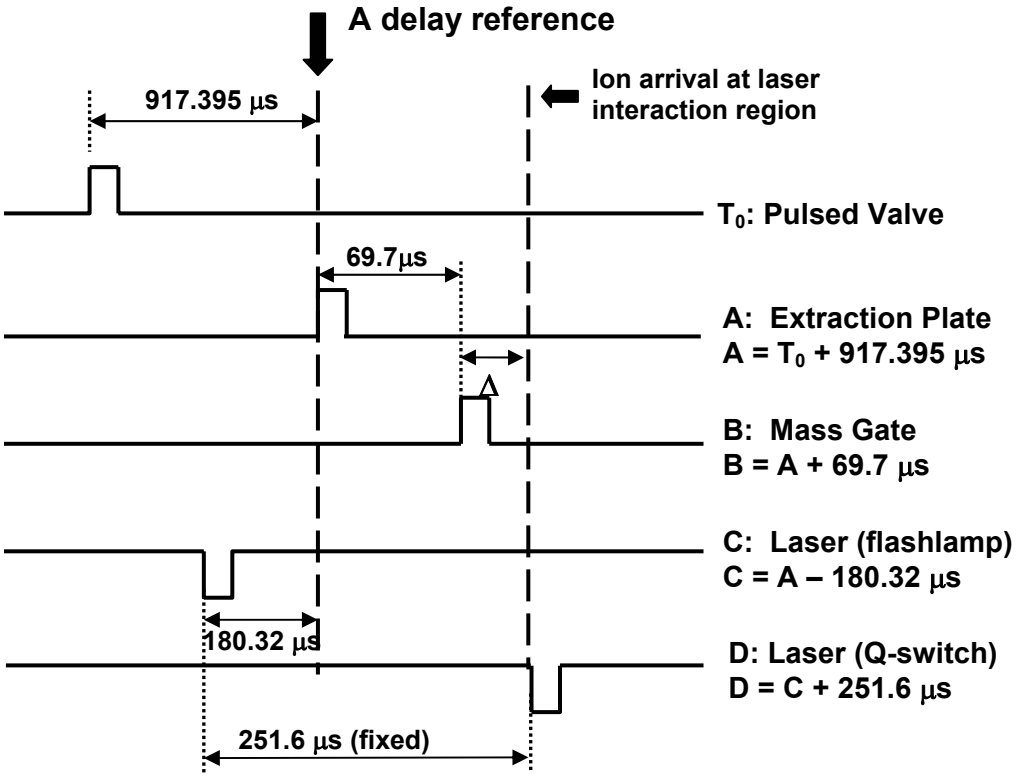

Figure 2.10: Ion and laser event timings for the nanosecond experiments. Actual delays from an experiment are included.

This time is calculated by the equation:

$$C = \text{Q-switch setting (251.6 } \mu s) - \text{mass gate delay (from B setting)} - \Delta \qquad (2.2).$$

This C value represents that amount of time before the extraction plate is triggered that the flashlamp must be triggered. The value for Δ is not known until photoproducts are actually observed.

- **Kinetic Energy Release and Angular Distributions**

In these experiments, the mass-selected parent diatomic anion is photodissociated to produce an atomic anion and an atomic neutral fragment. The laser timing is adjusted by monitoring the appearance of the photoneutrals on the in-line detector. The 8 mm orifice diameter of the entrance to the reflectron truncates the spatial distribution of the neutral fragments in the transverse direction thus limiting the total amount of neutrals striking the detector. The neutral signal at the in-line detector is amplified by both the EG&G pre-amplifier (x10) and by either a Phillips 771 amplifier that only provides linearity in gains up to 5x or the SR 240A amplifier providing gains up to 625. The amplified analog signal is then digitized and averaged with a Transient Recorder 200AS/Averaging Memory 4101. The sampling interval is 10 ns rather than the usual 20 ns to provided better temporal resolution for more accurate determination of peak separations in the neutral spectra. The spectra are typically average over 3000 or 5000 laser shots depending on signal levels.

- **Absolute Cross Section Measurements**

The absolute cross sections are determined from the depletion of a mass-selected parent ion signal after interaction with the laser. This is not a precise measurement in that a very small change needs to be measured in a very large signal. Any fluctuations and high backgrounds degrade the quality of the measurements, so numerous data sets are taken and averaged. The measurement made is the intensity of the parent ion with the laser on compared with the intensity with the laser off to determine the depletion of the parent ion as a result of photoabsorption. The percent depletion is measured as the ratio of depleted parent ion intensity over the parent ion intensity without laser absorption. Each intensity measurement consists of two measurements to take into account backgrounds. The depleted parent signal is determined by measuring the intensity with the both the reflectron and the laser on. The background for this is the intensity of the parent ion with the reflectron off, but with the laser on. This gives the background due to the presence of the laser itself being there. The non-depleted parent ion intensity has the reflectron on with the laser off. From this is subtracted the background with both the laser and the reflectron off. This ratio with the background subtractions is then inserted into Beer's Law. The process is summarized as:

Parent ion depleted = I(on, on) – I(off, on) = I_o

Parent ion = I(on,off) – I(off, off) = I_{off}

$$\sigma = \frac{1}{\Phi} \ln\left[\frac{I_{on}}{I_{off}}\right] \tag{2.3}$$

where the (on/off, on/off) corresponds to the state of the reflectron and laser (reflectron, laser). Equation 2.3 is Beer's law with σ being the cross section in cm^2 and Φ is absolute photon flux that is described in a later chapter. The reflectron and laser state are controlled by the 12 bit DAC. The DAC controls a mechanical shutter placed in the laser path with a maximum repetition rate of 40 Hz. The reflectron receives its voltage from a programmable power supply that itself is also controlled by the 12 bit DAC. Each data cycle consists of making each of the measurements of the four states of the reflectron/laser at 40 Hz to accommodate the maximum repetition rate of the shutter.

A schematic of the analog signal processing is shown in Fig. 2.11. The signal from the off-axis detector is amplified and sent to the Dual Gated Integrator that is triggered from the second SRS Delay Generator. The input analog signal is monitored along with the integrated signal on an oscilloscope. The integrator trigger timing is adjusted by observing the integrated signal on the scope. The gate from the integrator is then used to trigger the quad gate generator. From the quad gate generator, two gates are sent to the LeCroy ADC. The integrated signal is sent to the two gated channels of the ADC. The gates are set to be less than 100 ns to provide the largest dynamical range for the ADC. The gate timing is adjusted for each such that Gate 1 resides on the higher plateau of the integrated signal and the Gate 2 on the lower side of the signal (see Fig 2.11). The signal within each gate is digitized and

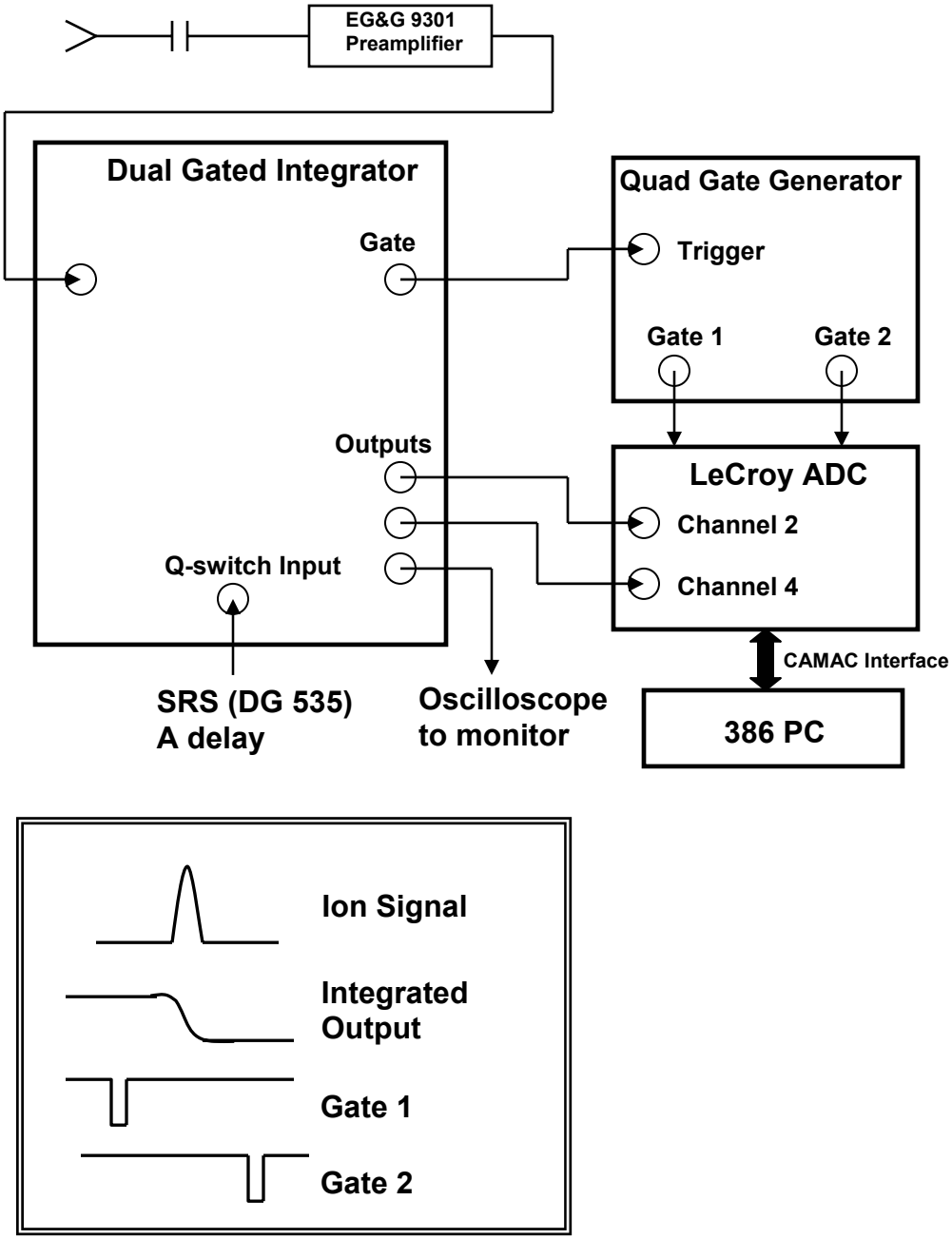

Figure 2.11: Analog signal processing electronics.

sent to the computer where the area of the ion peak is simply the digitized signal from Gate 1 minus the signal from Gate 2. The computer program then measures these digitized peak areas at the various reflectron/laser configurations and calculates the percent depletion from which the absolute cross section is calculated. The laser fluence is measured at a photodiode during each cycle to monitor fluctuations in laser intensity.

- **Relative Cross Section Measurements**

The relative cross section measurements are carried out by measuring the intensity of the photofragment ion divided by the parent ion intensity multiplied by the laser intensity. The fragment ions are measured at the off-axis detector with both the laser and the reflectron on. The reflectron on setting corresponds to placing a voltage on the reflectron to focuses the photofragment ion onto the off-axis detector. The off setting corresponds to placing the back plate of the reflectron at the float potential allowing the parent ion to travel through the reflectron to the in-line detector. The laser off position simply has a shutter closed blocking the laser. The various signals to be measured along with the relative cross section calculation are summarized in Fig. 2.12. The laser signal in the calculation is taken to be the measured laser power multiplied by the wavelength. The data acquisition program records the laser signal at a photodiode and includes it in the data output to determine the magnitude of fluctuations in the laser power. This signal, however, is not directly used in calculating the relative cross sections. The reflectron and shutter are controlled as described above.

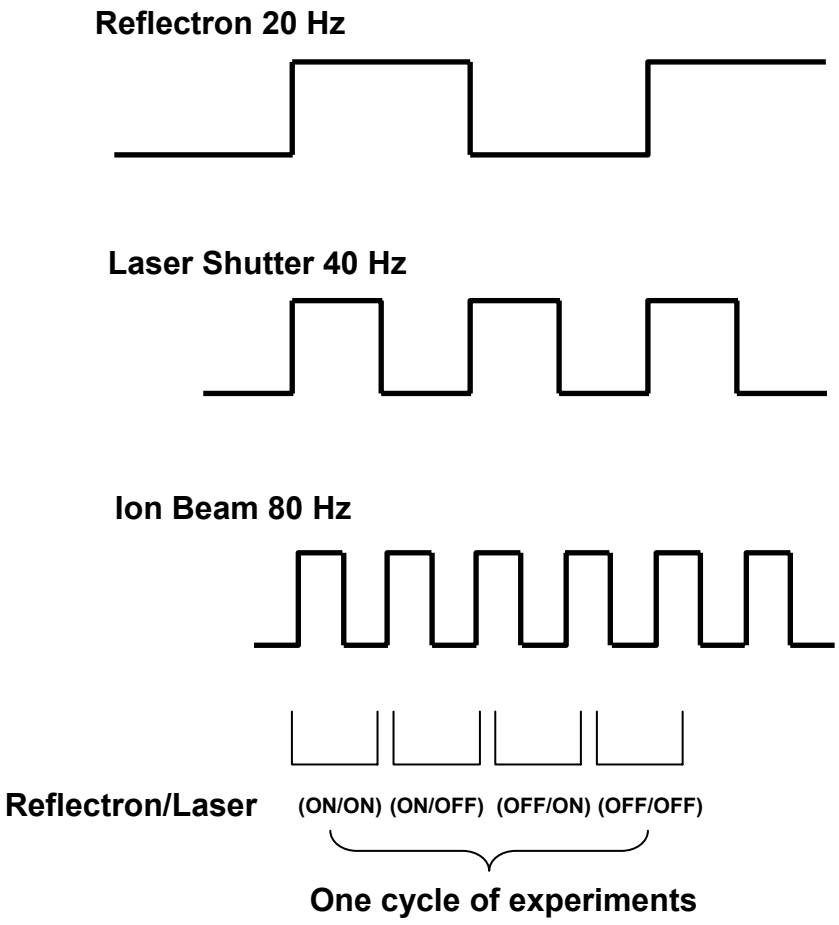

$$\sigma_{rel} = \frac{\text{Fragment}}{\text{Parent x Laser}}$$

At off-axis detector: Fragment = (on,on) – (off,on)

At in-line detector: Parent = (off, off) – (on, off)

Figure 2.12: Relative cross section data collection and calculation schematic.

The timing of the events within each cycle is depicted in Fig. 2.12. This scheme is used to maximize the repetition rate of both the ions (80 Hz) and the shutter (40 Hz). Each cycle consists of taking measurements at each of the four reflectron/laser configurations. Due to the 80 Hz repetition rate, each reflectron/laser configuration setting consists of two laser shots per cycle. Numerous runs are taken at each wavelength with typically 800 or 1000 cycles per run. The largest cross section across the band of wavelengths is set to equal 1 and the cross sections at the remaining wavelengths are then scaled accordingly. The absolute cross section measurement taken using the depletion method is used to determine the absolute cross sections across the band if desired.

- **Cluster Photofragmentation Product Distributions**

The photofragmentation distributions are carried out by intersecting the laser of a particular wavelength with a mass selected cluster ion. The full set of reflectron voltages are calculated for every possible photoproduct ion from a given parent cluster ion. The products present were determined by setting the reflectron to the voltage to focus a suspected fragment ion onto the off-axis detector. The appearance of a laser dependent signal on the oscilloscope at the exact flight time of the parent ion confirms the presence of the fragment ion upon dissociation of the parent cluster ion.

The fragment ion signal from the off-axis detector, that is amplified if desired, is sent to a transient recorder and averaged for 3000–5000 laser shots. A reference peak is chosen (typically the most intense fragment peak) from the photoproduct ions for a given parent cluster ion. The magnitude of this peak is determined at the onset

of a data run. Each data run consists of an averaged mass spectrum for each product ion present. Before each photofragment is averaged, the reference peak is checked and the ions and laser overlap are optimized if needed to achieve the original reference signal level. This should ensure that all the product ions are collected under the same ion and laser overlap conditions. Multiple runs are undertaken for each parent cluster that are then averaged together to yield the final product ratios. Previously characterized results put the statistical error at about 3% for a given fragment yield.[4]

2.11.4 Femtosecond Timing and Data Collection Schemes

The time-resolved experiments are carried out with the femtosecond laser system described above. The 400 Hz trigger from the Medox box is sent to a homemade modulo-N-divider that divides this trigger pulse down to 80 Hz. This 80 Hz pulse is used as the external trigger for the SRS delay generator that had been previously triggered internally for the nanosecond experiments. The timing for all other ion events is referenced to the 80 Hz external trigger; T_0 of the SRS delay generator. When the delay generator receives the 80 Hz laser trigger, the laser pulse that served as the trigger is instantaneously (on the timescale of the ion events) at the laser interaction region and thus unusable for absorption by the ions.

The events are timed so that the mass-selected ion packet formed by the trigger of the first laser pulse arrives at the laser interaction region as the subsequent laser pulse arrives. The system triggers off of every fifth laser shot (80 Hz), but laser pulses are arriving at the chamber at 400 Hz or every 2.5 ms. The three delays that

are used from the SRS delay generator are the B delay for the pulsed valve, the C delay for the extraction plate, and the D delay for the mass gate. The C delay serves as the laser timing, i.e. this delay is adjusted to overlap the ions and the laser. The entire sequence occurs in the 2.5 ms period between laser pulses. The mass gate timing, D, is C + x where x is the flight time between the extraction region and the mass gate. This value is determined by adjusting x until the ion of interest is mass selected. The valve timing, B, is C – y where y is the flight time of the ions from the valve to the extraction region that is optimized by monitoring the parent ion intensities. The extraction plate, C, is T_0 + z where z is the adjustable timing to ensure the ion packet and laser are overlapped temporally. The value for z can coarsely be calculated by subtracting the value of the D delay, the flight time from the extraction region to the mass gate, from 2.5 ms. However, there is a short ion flight time between the mass gate and the laser interaction region that must be accounted for by simply adjusting the C timing and observing the appearance of laser-dependent photofragment ion signal on the oscilloscope.

The off-axis detector is operated in a single ion counting mode for the typically small two-photon signal. The detector is biased at 2.8–2.9 kV with a large amount of electronic noise present at these large voltages. The two-photon signal is pre-amplified and sent to a 300 MHz Phillips 6904 Discriminator. The threshold voltage of the discriminator is set to pass the two-photon signal and reject the smaller electronic background noise. The output of the discriminator is sent to the Quad Scaler that counts the ion signal for up to four different two-photon products. The scaler has four separate channels that are each given a timing gate from a home built

pulse delay driver. The delay driver is triggered by the A output of the second SRS delay generator. Each individual timing gate has an adjustable delay and width. The timing gates have a TTL monitor that is sent to the oscilloscope. One of the discriminator outputs is likewise sent to the same oscilloscope. The gates are coarsely adjusted by the A delay of the second SRS box by observing their position with respect to the two-photon signal on the scope. Fine adjustments of each gate delay and width are made with respect to the two-photon product signals on the scope. The Quad scaler is connected to the data acquisition program through the CAMAC and GPIB interfaces. The parent ions that do not interact with the laser are monitored on the in-line detector for normalization of the two-photon signal. The in-line detector signal is sent to the Dual Gated Integrator and monitored on an oscilloscope in a manner analogous to the cross section measurements mentioned above.

The data acquisition program measures the counts in each of the four set gates at a series of five delay pump-probe times. The desired delay times are inputted along with a reference delay time. The program moves the delay stage through the 12 bit DAC along with shutters in the pump and the probe optical paths for background collection. The reference signal is chosen to be at a point where there is significant two-photon signal if possible. Within each data cycle, three backgrounds are taken. Two backgrounds have either the pump or the probe blocked and the third background has both pump and probe blocked. The ion counts at the reference are taken after the backgrounds and then counts at each of the five delays are taken. Finally, the counts at the reference are again taken. If the reference counts before and

after the delay points vary by more than 10%, the data set is discarded. Also, if the background at the three pump/probe configurations (off/on + on/off – off/off) is more than 30 or 40 % of the reference signal then the data set is also discarded. Typically, 3000 or 5000 laser shots are taken at each delay or background point over multiple cycles. At each point, the integrated parent ion intensity from the in-line detector is recorded and used for normalization of the data. A very detailed description of the femtosecond pump-probe experiment is given elsewhere.[22]

2.11.5 Photoelectron Imaging Timing and Data Acquisition

The photoelectron imaging experiment uses the Infinity nanosecond laser system, but is triggered in a manner similar to the femtosecond experiments. The SRS delay generator is triggered by the Q-switch synch output from the Infinity power supply after being divided down to 50 Hz by the modulo-N-divider from the 100 Hz repetition rate of the Infinity laser. The delays are the same as for the femtosecond experiment with the C delay being the extraction and "laser" delay, B is the pulsed valve delay and D is the mass gate delay. The timing of C is calculated in the same manner, but now the D delay is subtracted from 10000 μs, reflecting the new repetition rate of the laser. The new delay introduced in the imaging experiment is the electron extraction plate timing that is controlled by delay A. The A delay is set to be roughly C + 15 μs. The extraction plate is turned well before the ions arrive in the laser interaction region and is set for width of 50 μs. Initially, the extraction plate was turned on a few nanoseconds before the laser intersected the mass-selected ion packet and stayed on for only 200 ns. The extraction plate timing was also tuned

to optimize the images. However, it was determined that the ring diameters in the images (and thus the energies) change as this timing is varied at these very small extraction plate pulse widths. Although, not visually noticeable when observing the images, small changes in the extraction timing lead to significant changes in the photoelectron energy spectra. The longer extraction plate pulse width turned on well before the ions reach the laser interaction region eliminates this ring size dependence on the extraction timing.

The images are acquired in two modes with both being controlled by the DaVis data acquisition software that accompanied the CCD camera and are depicted in Fig 2.13. The first mode is the so-called analog mode with images being acquired for a variable exposure time (0.1 to 100000 μs). These analog images contain not only the photoelectron counts, but also any background counts present. Background images are taken with the laser blocked to determine the parent ion background and with the ions blocked (gate valve closed) to determine the background from the laser. The laser background is typically low at wavelengths longer than 300 nm with the ion background being much larger. The backgrounds are subtracted from the photoelectron images using routines programmed in LabView. Multiple images are also summed together after background subtractions using these same routines.

The second acquisition method is carried out by using the event counting mode of the data acquisition software. In the analog method, an event appeared as a spot that was roughly 6 x 6 square pixels in area along with a background of various magnitudes throughout the remaining pixels. Event counting looks for the maximum number of counts within a 6 x 6 square pixel area and puts a value of one in the center

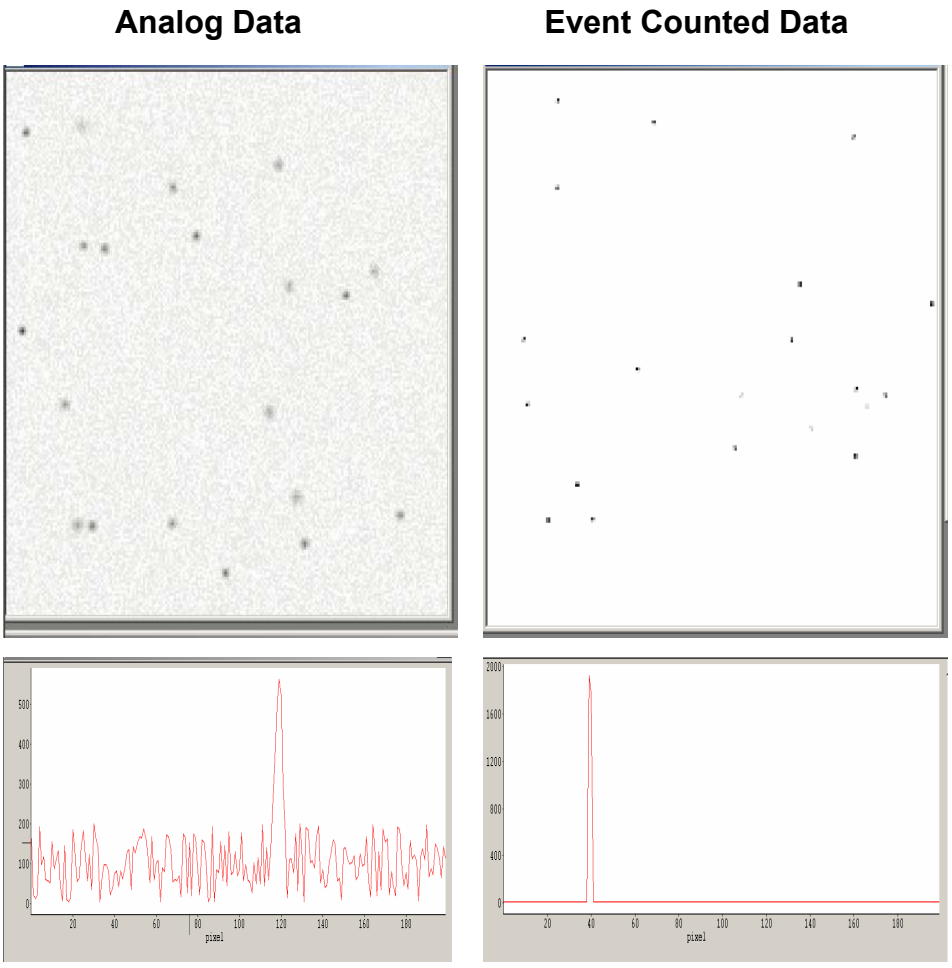

Figure 2.13: Simulated data showing typical analog image data versus event counted image data.

pixel if the counts are above a set threshold. The threshold is determined by a statistics function within the DaVis software. This takes images with events and without events (the phosphor screen voltage set to zero) and recommends a threshold setting and an offset value. The offset value is the constant background counts across the pixel array that is subtracted from the event peaks. The threshold value is then set to only allow photoelectron events to be counted that are presumably greater than any background counts. In this way, pixel resolution is achieved on a zero background. This method leads to higher quality images with improved resolution as compared to the analog method.

A concern with event counting is that signal loss can occur if the CCD camera exposure time is not set to be short enough. If this exposure time is long, it is probable that multiple, real photoelectron events occur within the same 6 x 6 pixel area. However, as the event counting procedure is defined, only the event with highest intensity is counted with the other events being discarded. It is found that using exposure times of 100 or 250 μs minimizes signal loss. A full image is then acquired by taking 3000 to 100000 short time exposures and summing them. Multiple full images can themselves be summed using the LabView routines mentioned above.

In either the analog or event counting mode, the images at this point represent the raw 2-D representations of the 3-D photoelectron spheres. The 3-D spheres are reconstructed using the BASEX method developed in the Reisler group[23] from which a slice is taken through the center. The BASEX software takes the event counted raw image .dat file as the input. Accurate determination of the pixel coordinates of the

center of the image is critical. The second version of BASEX contains an algorithm that calculates the center of inputted image. This is checked by overlaying a circle on the raw image and determining the coordinates of the center visually. The BASEX calculated center is generally accurate, although having the center coordinates wrong by a few pixels is enough to degrade the reconstructions severely.

The BASEX software provides the raw image, the reconstructed image, and the speed distribution as the outputs. The speed distribution is the angle integrated intensity as a function of a selected pixel step size (usually 1 pixel) in the radial direction from the center of the image. The speed scale is then converted to electron kinetic energy (eKE) by using a calibration spectrum of known peak energies. It is typically desirable to use an atomic species for calibration due to much narrower photoelectron peaks widths in atoms. A new calibration is needed when the extraction voltage is changed, as the extraction voltage determines the pixel energy scale. The electron kinetic energy is then simply converted to electron binding energy (eBE) by use of the equation $eBE = E_{h\nu} - eKE$, where $E_{h\nu}$ is the photon energy. Additionally, BASEX calculates the anisotropy parameter, β, at each radial pixel or eKE. The exact definition of β is discussed below in a following chapter.

Chapter 2 References

[1] W. C. Wiley and I. H. McLaren, Rev. Sci. Instr. **26** (12), 1150 (1955).

[2] A. Eppink and D. H. Parker, Rev. Sci. Instr. **68** (9), 3477 (1997).

[3] M. A. Johnson and W. C. Lineberger, in *Techniques for the Study of Ion Molecule Reactions*, edited by J. M. Farrar and J. W. Saunders (Wiley, New York, 1988), pp. 591.

[4] M. E. Nadal, Ph.D. Thesis, University of Colorado, 1996.

[5] M. E. Nadal, P. D. Kleiber, and W. C. Lineberger, J. Chem. Phys. **105** (2), 504 (1996).

[6] J. M. Papanikolas, J. R. Gord, N. E. Levinger, D. Ray, V. Vorsa, and W. C. Lineberger, J. Phys. Chem. **95** (21), 8028 (1991).

[7] V. Vorsa, S. Nandi, P. J. Campagnola, M. Larsson, and W. C. Lineberger, J. Chem. Phys. **106** (4), 1402 (1997).

[8] M. A. Taylor, Ph.D. Thesis, University of Colorado, 2004.

[9] A. W. Castleman, Jr. and R. G. Keesee, Chem. Rev. **86**, 589 (1986).

[10] J. I. Steinfeld, J. S. Francisco, and W. L. Hase, *Chemical Kinetics and Dynamics*. (Prentice Hall, Englewood Cliffs, New Jersey, 1989).

[11] N. E. Levinger, Ph.D. Thesis, University of Colorado, 1990.

[12] W. H. Robertson, J. A. Kelley, and M. A. Johnson, Rev. Sci. Instr. **71** (12), 4431 (2000).

[13] U. Even, J. Jortner, D. Noy, N. Lavie, and C. Cossart-Magos, J. Chem. Phys. **112**, 8068 (2000).

[14] M. Hillenkamp, S. Keinan, and U. Even, J. Chem. Phys. **118**, 8699 (2003).

[15] M. L. Alexander, N. E. Levinger, M. A. Johnson, D. Ray, and W. C. Lineberger, J. Chem. Phys. **88** (10), 6200 (1988).

[16] B. A. Mamyrin, V. I. Karataev, D. V. Shmikk, and V. A. Zagulin, Sov. Phys.-JEPT **37** (1), 45 (1973).

[17] L. A. Posey, M. J. DeLuca, and M. A. Johnson, Chem. Phys. Lett. **131** (3), 170 (1986).

[18] E. Surber, R. Mabbs, and A. Sanov, J. Phys. Chem. A **107** (40), 8215 (2003).

[19] A. E. Siegman, *Lasers*. (University Science Books, Mill Valley, CA, 1986).

[20] M. H. Dunn and M. Ebrahimzadeh, Science **286** (5444), 1513 (1999).

[21] J. D. Kafka, M. L. Watts, and J.-W. J. Pieterse, IEEE Journal of Quantum Electronics **28** (10), 2151 (1992).

[22] J. M. Papanikolas, Ph.D. Thesis, University of Colorado, 1994.

[23] V. Dribinski, A. Ossadtchi, V. Mandelshtam, and H. Reisler, Rev. Sci. Instr. **73**, 2634 (2002).

Chapter 3

Photodissociation Dynamics of $IBr^-(CO_2)_n$ Cluster Anions

3.1 Introduction

Photodissociation of mass-selected $IBr^-(CO_2)_n$, n = 0–14, cluster ions is carried out to study the effects of the presence of the CO_2 solvent on the IBr^- solute anion. One-color experiments focus on the determination of anion photoproduct branching ratios as both a function of excitation wavelength and initial cluster size. Photoproduct branching ratios illustrate the degree of perturbation to the internal electronic structure of the IBr^- solute upon solvation by a known number of solutes molecules in well-defined configurations. The steric effects of the solvent cage as a physical barrier to dissociation that may be present in these systems are also highlighted by the photoproduct distributions.

The $IBr^-(CO_2)_n$ clusters are excited to the A' $^2\Pi_{1/2}$ and B 2 $^2\Sigma^+_{1/2}$ electronic states of the IBr^- chromophore. The photoproducts for excitations to these two states are determined for the bare IBr^- solute. The effects of the solvent are then studied by the types of photoproducts formed as a function of initial cluster size. The solvent is shown to drive nonadiabatic transitions in the chromophore solute involving charge-transfer between the dissociating atoms of the solute, spin-orbit relaxation within the neutral photoproducts, and vibrational relaxation followed by solute recombination on the ground state. The photoproduct ratios provide the data needed to carry out a time-resolved pump-probe experiment to determine the timescale for recombination of $IBr^-(CO_2)_8$ on the ground $^2\Sigma^+_{1/2}$ state, following excitation to the A' state.

Prior to the solvation studies of $IBr^-(CO_2)_n$ clusters, the IBr^- chromophore is first spectroscopically characterized to determine the properties of the solute before solvation as well as to determine the excitation wavelengths to be used in the cluster photodissociation experiments. Relative cross section measurements are carried out across the $A'\ ^2\Pi_{1/2} \leftarrow X\ ^2\Sigma^+_{1/2}$ absorption band to determine the wavelength profile as well as to identify the photoproduct(s) present after excitation to the A' state. A depletion measurement is employed near the band maximum to record the absolute cross section measurement that is then used to scale the relative cross section measurements at the other wavelengths. The absolute cross sections are used to determine the feasibility of two-photon, time-resolved experiments. Translational energy release measurements of the photodissociated IBr^- provide a bond strength measurement for the solute. The experimental results are compared to theoretical calculations of the potential energy curves and absorption spectrum.[1,2]

The photodissociation dynamics of $IBr^-(CO_2)_n$ clusters is discussed in the context of comparisons with results of similar experiments previously carried out in $ICl^-(CO_2)_n$ and $I_2^-(CO_2)_n$ cluster ions. These previous results along with the results for $IBr^-(CO_2)_n$ clusters present an overall picture of the role of the various dihalide solutes in determining the solvation dynamics. The $IBr^-(CO_2)_n$ clusters, also, present a mixed halide system that is well-suited for time-resolved experiments.

3.2 Spectroscopic characterization of bare IBr^-

The calculated potential energy curves for the six low-lying electronic states of IBr^- anion are shown in Fig. 3.1. The ground state is bonding in nature and has a deep, attractive well. The other five electronic states are either dissociative or have very shallow wells. The IBr^- anion has 11 valence electrons, one short of a full valence shell. The anion behaves as a one-electron molecule with the symmetry of the electronic state determined by location of the electron hole. The state labels in Fig. 3.1 correspond to Hund's case (c) where strong spin-orbit mixing is present and is experimentally confirmed below. The strong spin-orbit coupling leads to four distinct dissociation limits for the six valence electronic states. The dissociative states with neutral iodine as a photoproduct are asymptotically separated by the 0.94 eV spin-orbit splitting in iodine.[3] The curves corresponding to formation of the neutral bromine photoproduct are separated by 0.457 eV, reflecting the spin-orbit splitting in bromine.[4] The IBr^- anion has a formal bond order of 1/2 and has a calculated [5] equilibrium bond length of 3.053 Å. The measured vibrational frequency of IBr^- is 136 cm^{-1}.[6]

The photoabsorption spectrum of the A' $^2\Pi_{1/2} \leftarrow$ X $^2\Sigma^+_{1/2}$ absorption band in IBr^- is measured to determine the shape, location, and magnitude of this band. Characterization of this band is crucial in that excitation on the A' electronic state is a focus of experiments described below. The spectrum characterization is carried out by the measurement of relative cross sections at wavelengths across the band as discussed in Ch. 2. The measured spectrum for A' is shown in Fig. 3.2. The band is a

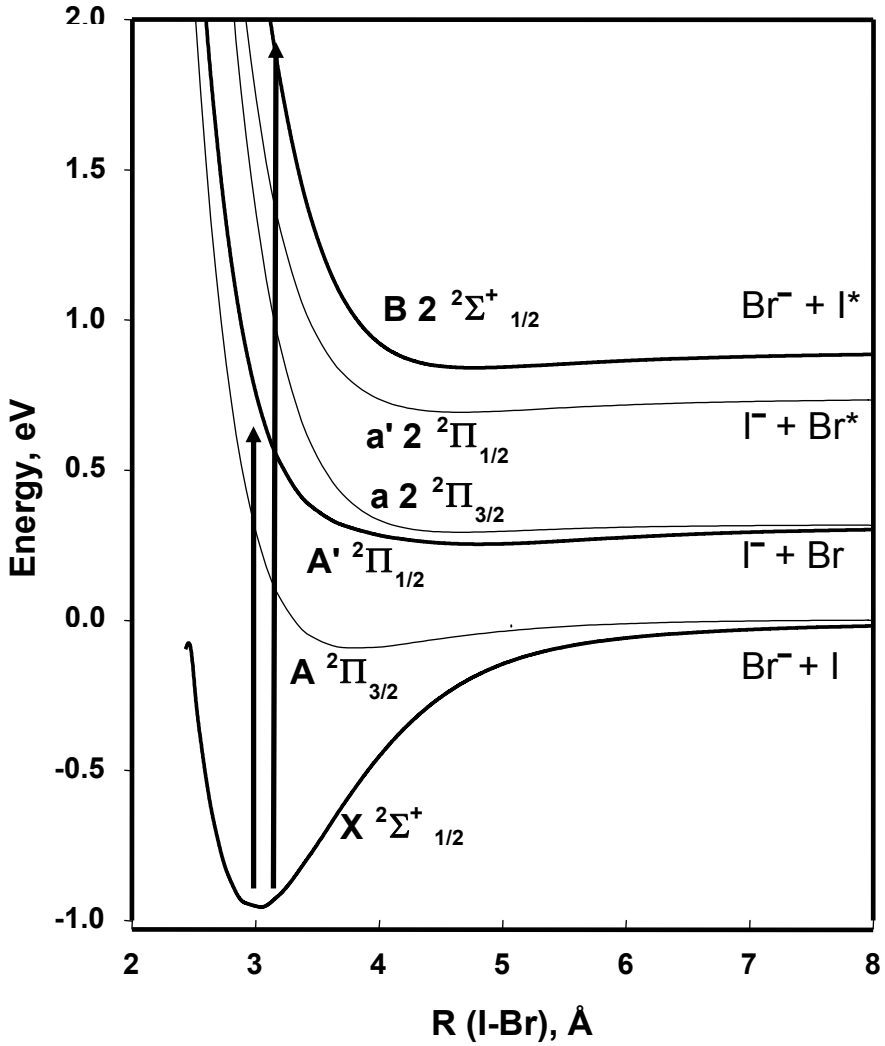

Figure 3.1: Calculated potential energy curves for the lowest six electronic states of IBr^-. Arrows indicate the studied transitions to the A' and B states.

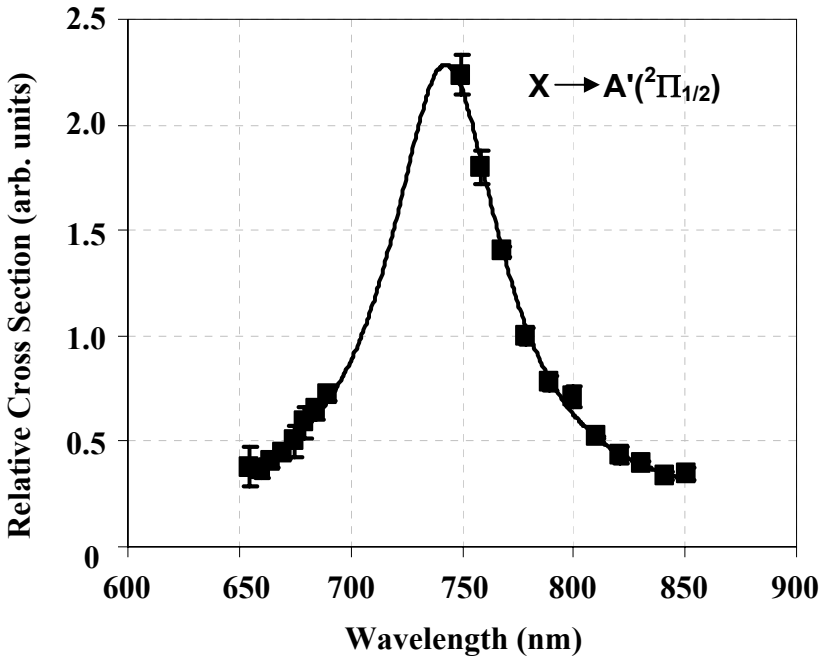

Figure 3.2: Relative cross sections for the A' absorption band. The solid line is a Gaussian fit to the data points. The error bars represent one standard deviation of the statistical uncertainty.

broad, featureless Gaussian-shaped curve centered around 740 nm with a full-width half-maximum of ~50 nm. The absence of points between 690–740 nm is due to the degeneracy gap in the Infinity-XPO laser system described in Ch. 2. A Gaussian curve is fit to the experimental data points and is superimposed on the data in Fig. 3.2. The error bars for each point represent the statistical fluctuations in the relative cross section measurements and are taken to be one standard deviation of the mean. The photoproduct I^- is the sole product formed across the band measured confirming that only one electronic state is excited, with dissociation taking place exclusively on the A' electronic state.

The calculated absorption spectrum[2] is shown in Fig. 3.3. The peak of the A' band is calculated to be 765 nm, which is slightly red-shifted from the experimentally measured band maximum of 740 nm. There is also calculated to be negligible overlap between the A' band and the absorption bands of adjacent electronic states. Transitions to the B electronic state are also investigated in experiments described below. The spectroscopic characterization of the B band was not carried out. The wavelengths that are used for excitation to this state are inferred from the calculated spectrum. The experimentally measured A' band was blue-shifted from the calculated, so it is assumed that peak transitions to the B state are slightly blue-shifted from the calculated band maximum of 405 nm.

A depletion measurement that is described in Ch. 2 is carried out at 760 nm near the measured A' band maximum. The depletion measurement yields the absolute cross section via Beer's Law. The photon flux, Φ, is given by the measured laser pulse energy divided by $h\nu$ times the area of the laser spot where ν is the frequency of

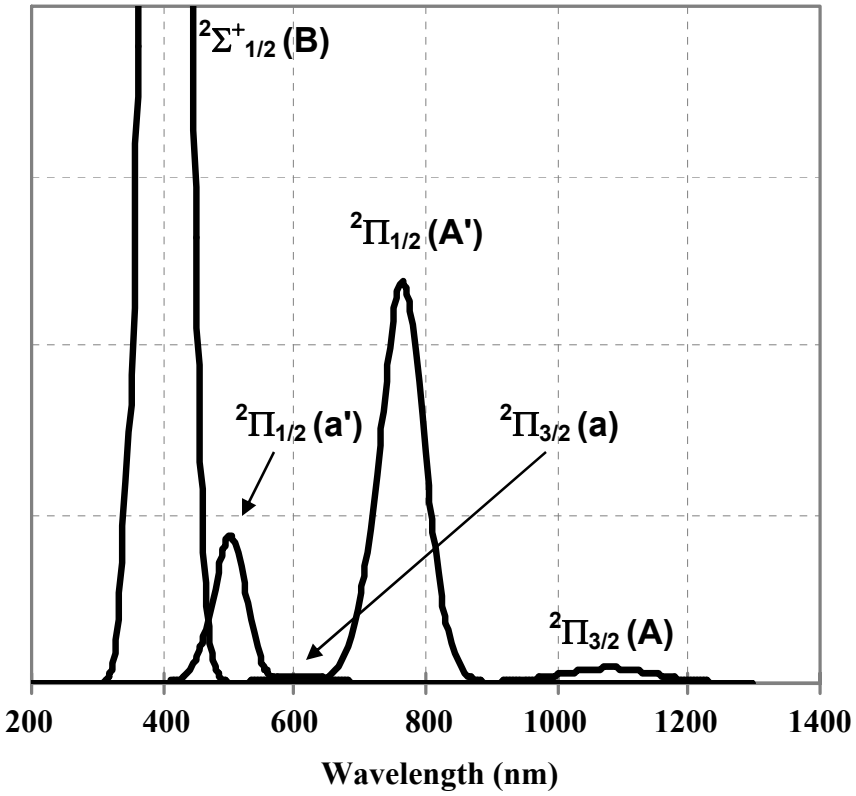

Figure 3.3: Calculated absorption spectrum for unsolvated IBr^-.

the laser light. The photon flux has the units of photons/pulse∗cm^2. For instance, 760 nm light with a pulse energy of 2.1mJ/pulse and a spot diameter of 10.5 mm has a flux of 9.28 x 10^{15} photons/pulse∗cm^2. The measured depletion was found to be 6% yielding an absolute cross section of 6.9 x 10^{-18} cm^2 at 760 nm. Using the measured relative cross sections, the absolute cross section is calculated to be 3 x 10^{-18} cm^2 at 790 nm. The cross section at this wavelength is calculated to determine the feasibility of two-photon experiments on IBr^-. The femtosecond laser system performs most effectively at wavelengths around 790 nm. In the pump-probe absorption recovery experiments, the cross section for the two-photon absorption process is approximated as the cross section for one-photon absorption squared. The measured cross section for IBr^- at 790 nm from above is 3 x 10^{-18} cm^2. Similar measurements carried out on I_2^- and ICl^- found the cross sections at 790 nm to be 2.5 x 10^{-17} and <<5 x 10^{-19} cm^2, respectively.[7,8] The two-photon cross section for IBr^- is 100 times less than for I_2^- and ICl^- is even weaker at about 1000 times less than for I_2^-. Two-photon experiments have been successfully carried out for I_2^- solvated systems.[9-12] Two-photon experiments are also shown in a following section to be successful at this much lower two-photon cross section for IBr^-. However, based on these cross section arguments, ICl^- two-photon experiments are probably not feasible at wavelengths around 790 nm.

The near-IR absorption spectrum was measured for unsolvated IBr^-, but not measured for the $IBr^-(CO_2)_n$ clusters. The absorption spectrum of $ICl^-(CO_2)_4$ has been measured previously[13] to determine the effect of solvation on the absorption characteristics of the ICl^- solute. This cluster size was chosen due to the prediction

that the largest solvent electric field (largest asymmetric solvation) on the ICl^- solute electronic states is produced at this size. The solvated spectrum shows virtually no shift when compared to the bare ICl^- spectrum. The electronic structure of the ICl^- solute is not significantly perturbed by the presence of the solvent at internuclear separations close to the equilibrium bond length, which is the region that is being probed by the one-photon cross section measurements. This agrees well with dynamics simulations[14] that show perturbations to the electronic states occurring at large internuclear separations (~6–8 Å). It is assumed that the perturbations to the IBr^- solute electronic states only occur at large internuclear separations, as well.

Translational energy spectroscopy[15] is used to measure the kinetic energy release on the A' state during the photodissociation of IBr^- with multiple excitation wavelengths. The measurement of the time splitting between the forward and backward scattered neutral fragments on the in-line detector from the photodissociated IBr^- is used to determine the kinetic energy release on the A' state. The kinetic energy release is then related to the bond strength, $D_{0,}$ for the ground state of IBr^-. The angular distributions of the recoiling neutral Br photofragments are also used to determine the direction of the $A'\ ^2\Pi_{1/2} \leftarrow X\ ^2\Sigma^+_{1/2}$ electronic transition upon excitation with linearly polarized light.

The time-of-flight spectra for the photodissociated Br atoms are shown in Fig. 3.4 with (a) corresponding to dissociation with light polarized parallel to the ion flight axis and (b) is light polarized perpendicular to the flight axis. Figure 3.4(a) shows a spectrum consisting of a doublet of peaks representing neutral fragments ejected with velocities toward and away from the in-line detector. The case of the light

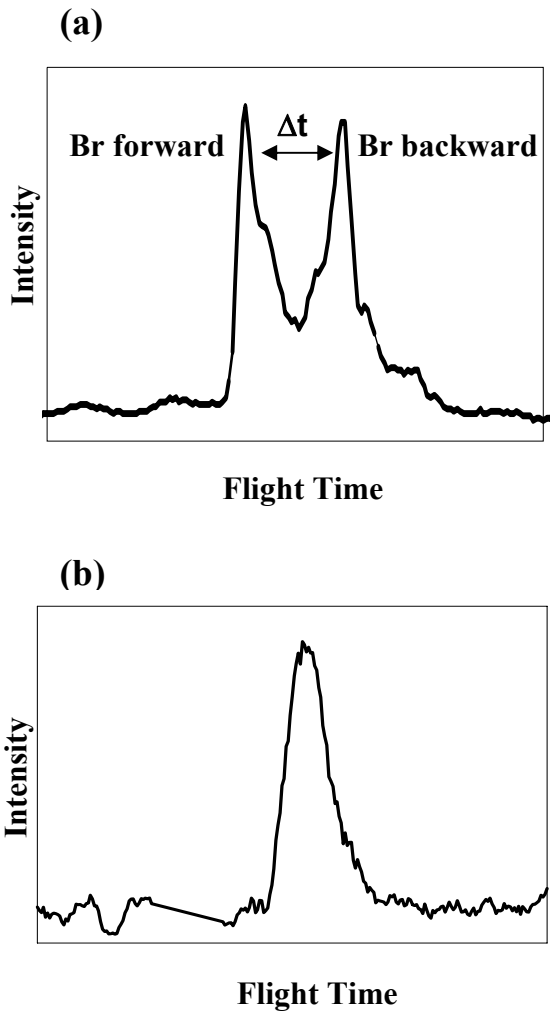

Figure 3.4: Neutral Br time-of-flight spectra of photodissociated IBr^- at 790 nm with the laser polarized (a) parallel to the ion flight axis and (b) perpendicular to the flight axis.

polarization perpendicular to the flight axis leads to a single peak in the neutral spectrum. These results show that the fragments are ejected along the polarization axis and the transition dipole moment is parallel to the internuclear axis of IBr^-. This characterizes the A' $^2\Pi_{1/2} \leftarrow$ X $^2\Sigma^+_{1/2}$ electronic transition as a parallel transition.

In the absence of spin-orbit coupling, Hund's case (a) can be applied in which the transition dipole moment lies along the internuclear axis for a purely parallel transition. This is the case for the $\Delta\Lambda = 0$, $\Sigma \leftarrow \Sigma$ or $\Pi \leftarrow \Pi$. For a purely perpendicular transition, the dipole moment lies perpendicular to the internuclear axis. This occurs for $\Delta\Lambda = \pm 1$, $\Sigma \leftarrow \Pi$. The A' $^2\Pi_{1/2} \leftarrow$ X $^2\Sigma^+_{1/2}$ transition should be perpendicular under Hund's case (a), however it is experimentally found to be parallel. Strong spin- orbit coupling leads to a Hund's case (c) description where the transition moment does not have to lie along a symmetry axis. This also leads to the two spin-orbit states for both I and Br and as seen by the presence of four distinct product channels in the potential energy curves shown in Fig. 3.1.

The photodissociation of IBr^- with parallel polarization laser light leads to distinct forward and backward scattered peaks as labeled in Fig. 3.4(a). The flight time splitting between the two is measured and used to determine the kinetic energy release on the A' electronic state. The kinetic energy of the parent IBr^- anion is found by taking half of the extraction voltage and adding this to the beam potential of 2500 eV. The velocity of the center of mass, V_{COM}, is then:

$$V_{COM} = \sqrt{\frac{2E}{M}} \tag{3.1}$$

where E is the kinetic energy of the IBr^- in joules and M is the mass of IBr^- in kilograms. The recoil velocity of the Br fragment, V_{Br}, is found by the expression:

$$V_{Br} = \frac{(V_{COM})^2 \Delta t}{2x} \tag{3.2}$$

where V_{COM} is the center of mass velocity found from Eq. 3.1, Δt is the measured time difference between the forward and backward scattered peaks, and x is the distance from the laser interaction region to the in-line detector (0.448 m for this apparatus). The kinetic energy release (KER) is:

$$KER = \frac{1}{2} V_{Br}^2 * m_{Br} * \left[1 + \frac{m_{Br}}{m_I} \right] \tag{3.3}$$

where V_{Br} is the recoil velocity of the Br fragment from Eq. 3.2, m_{Br} and m_I are the masses of Br and I, respectively. Finally, the bond strength of IBr^-, D_0, is found by:

$$D_0 = h\nu - \left[KER + \left(EA(Br) - EA(I) \right) \right] \tag{3.4}$$

where hν is the A' excitation photon energy, KER is found from Eq. 3.3, and EA(Br) and EA(I) are the electron affinities of Br and I, 3.3636 and 3.0591 eV, respectively. The D_0 calculations are performed at four different wavelengths within the A' band and averaged to give a value of the bond strength of IBr^- of 1.10 ± 0.04 eV, where the

error represents one standard deviation of the mean. This makes the bond strength of IBr^- comparable to that of ICl^- at 1.07 eV and I_2^- at 1.01 eV.[8,16]

3.3 Photofragmentation of $IBr^-(CO_2)_n$ upon excitation to the A' $^2\Pi_{1/2}$ state

The photodissociation of mass-selected $IBr^-(CO_2)_n$ cluster ions is investigated at a series of wavelengths providing excitation to the spectroscopically characterized A' $^2\Pi_{1/2}$ electronic state of IBr^-. The photodissociation is carried out at 790 nm, 760 nm, and 675 nm. These wavelengths span the absorption band of A' and provide kinetic energy releases on A' of 0.3, 0.35, and 0.55 eV, respectively. The 760 nm wavelength is chosen due to its proximity to the peak of the absorption band, 790 nm due to the possibility of use in time-resolved experiments, and 675 nm to provide a larger kinetic energy release on the A' state. From the absorption studies of IBr^-, these wavelengths are shown to exclusively excite A' with I^- and Br as the sole photoproducts.

Solvation of IBr^- by CO_2 yields three distinguishable product channels:

$$IBr^-(CO_2)_n \rightarrow I^-(CO_2)_{n-m} + mCO_2 + Br \qquad (A)$$

$$\rightarrow IBr^-(CO_2)_{n-k} + kCO_2 \qquad (B)$$

$$\rightarrow Br^-(CO_2)_{n-p} + pCO_2 + I \qquad (C)$$

Channel (A) corresponds to direct dissociation on the A' state, giving the expected I^--based dissociation products. Channel (B) corresponds to cage recombination, reforming the dihalide anion on the ground electronic state after dissociation. The number of solvents retained on the recombined products (B) reflects the extent of

vibrational relaxation on the ground state and is discussed in detail below. Channel (C) corresponds to a dissociative event following charge transfer from the initially formed I^- to the neutral Br. Both Channels (B) and (C) represent processes that require solvent participation. For the larger clusters ($n \geq \sim 4$, an additional channel producing spin-orbit excited iodine, I*, is energetically accessible through the additional process

$$IBr^-(CO_2)_n \quad \rightarrow \quad Br^-(CO_2)_{n-(p+4)} + (p+4)CO_2 + I^*. \qquad (D)$$

The photofragmentation data show no evidence for product formation in this channel. Molecular dynamics simulations[17] have shown product formation in this channel for $ICl^-(CO_2)_n$ cluster photodissociation. Experimental results in previous work[13] likewise show this channel not to be present after excitation to A' in $ICl^-(CO_2)_n$ clusters. However, results on $ICl^-(CO_2)_n$ clusters at 790 nm exciation presented in Sec. 3.6 may show this channel to be accessible.

The photofragmentation products from excitation of $IBr^-(CO_2)_n$ clusters with 790, 760, and 675 nm photons as a function of cluster size are shown in Fig. 3.5, Fig. 3.6, and Fig. 3.7, respectively. The exact photoproducts formed with their percentages are shown in Tables 3.1, 3.2, and 3.3. The total percentages in bold are plotted in the figures. In each case, the photodissociation of the bare IBr^- solute leads solely to I^- as the ionic photoproduct. For 790 and 760 nm excitation, the addition of the first solvent molecule allows a nonadiabatic transition to the ground electronic state, yielding the charge transfer Br^- product ion. The addition of the second CO_2 solvent molecule increases the yield of the charge transfer Br^--based products and

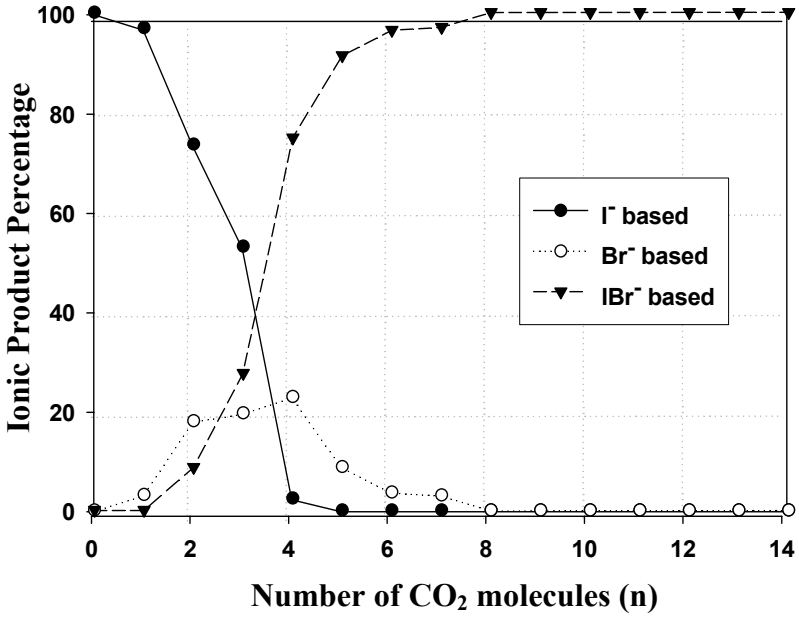

Figure 3.5: Photofragmentation products of $IBr^-(CO_2)_n$ cluster ions upon excitation to the A' $^2\Pi$ state with 790 nm photons and an energy release of 0.3 eV on the state.

Table 3.1: Photofragmentation branching ratios for $IBr^-(CO_2)_n$ at 790 nm.

Parent Ion	I^--based	Br^--based	IBr^--based
IBr^-	I^-: 100%	NONE	NONE
$IBr^-(CO_2)_1$	I^-: 36.3% $I^-(CO_2)_1$: 60.5% **[96.8%]**	Br^-: 3.2% **[3.2%]**	NONE
$IBr^-(CO_2)_2$	I^-: 4.5% $I^-(CO_2)_1$: 65.1% $I^-(CO_2)_2$: 3.9% **[73.5%]**	Br^-: 5.1% $Br^-(CO_2)_1$: 12.8% **[17.9%]**	IBr^-: 8.6% **[8.6%]**
$IBr^-(CO_2)_3$	$I^-(CO_2)_1$: 48.9% $I^-(CO_2)_2$: 4.1% **[53.0%]**	$Br^-(CO_2)_1$: 12.2% $Br^-(CO_2)_2$: 2.5% $Br^-(CO_2)_3$: 4.8% **[19.5%]**	IBr^-: 23.2% $IBr^-(CO_2)_1$: 4.3% **[27.5%]**
$IBr^-(CO_2)_4$	$I^-(CO_2)_1$: 2.4% **[2.4%]**	$Br^-(CO_2)_1$: 6.6% $Br^-(CO_2)_2$: 16.2% **[22.8%]**	IBr^-: 72.8% $IBr^-(CO_2)_1$: 2.0% **[74.8%]**
$IBr^-(CO_2)_5$	NONE	$Br^-(CO_2)_2$: 3.1% $Br^-(CO_2)_3$: 5.6% **[8.7%]**	IBr^-: 49.4% $IBr^-(CO_2)_1$: 35.7% $IBr^-(CO_2)_2$: 6.2% **[91.3%]**
$IBr^-(CO_2)_6$	NONE	$Br^-(CO_2)_3$: 3.6% **[3.6%]**	IBr^-: 5.8% $IBr^-(CO_2)_1$: 58.0% $IBr^-(CO_2)_2$: 31.0% $IBr^-(CO_2)_3$: 1.6% **[96.4%]**
$IBr^-(CO_2)_7$	NONE	$Br^-(CO_2)_4$: 3.0% **[3.0%]**	$IBr^-(CO_2)_1$: 16.0% $IBr^-(CO_2)_2$: 50.8% $IBr^-(CO_2)_3$: 22.4% $IBr^-(CO_2)_4$: 7.8% **[97.0%]**
$IBr^-(CO_2)_8$	NONE	NONE	$IBr^-(CO_2)_1$: 2.1% $IBr^-(CO_2)_2$: 25.9% $IBr^-(CO_2)_3$: 48.6% $IBr^-(CO_2)_4$: 20.2% $IBr^-(CO_2)_5$: 3.2% **[100%]**
$IBr^-(CO_2)_9$	NONE	NONE	$IBr^-(CO_2)_2$: 5.6% $IBr^-(CO_2)_3$: 37.4% $IBr^-(CO_2)_4$: 38.6% $IBr^-(CO_2)_5$: 16.6% $IBr^-(CO_2)_6$: 1.8% **[100%]**

$IBr^-(CO_2)_{10}$	NONE	NONE	$IBr^-(CO_2)_3$: 11.8% $IBr^-(CO_2)_4$: 38.2% $IBr^-(CO_2)_5$: 37.9% $IBr^-(CO_2)_6$: 12.1% **[100%]**
$IBr^-(CO_2)_{11}$	NONE	NONE	$IBr^-(CO_2)_4$: 7.4% $IBr^-(CO_2)_5$: 50.1% $IBr^-(CO_2)_6$: 42.5% **[100%]**
$IBr^-(CO_2)_{12}$	NONE	NONE	$IBr^-(CO_2)_5$: 22.2% $IBr^-(CO_2)_6$: 48.7% $IBr^-(CO_2)_7$: 29.1% **[100%]**
$IBr^-(CO_2)_{13}$	NONE	NONE	$IBr^-(CO_2)_7$: 87.4% $IBr^-(CO_2)_8$: 12.6% **[100%]**
$IBr^-(CO_2)_{14}$	NONE	NONE	$IBr^-(CO_2)_7$: 53.7% $IBr^-(CO_2)_8$: 46.3% **[100%]**

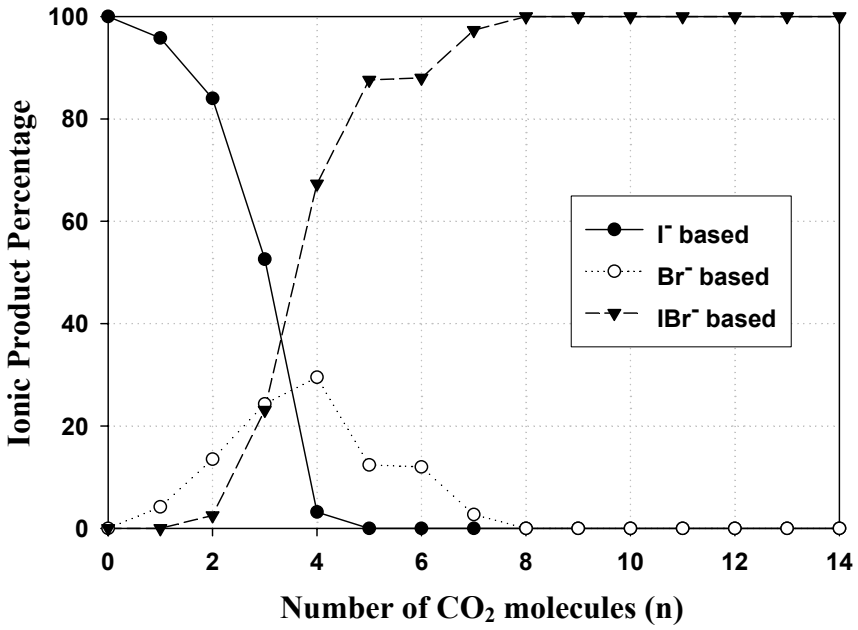

Figure 3.6: Photofragmentation products of $IBr^-(CO_2)_n$ cluster ions upon excitation to the A' $^2\Pi$ state with 760 nm photons and an energy release of 0.35 eV on the state.

Table 3.2: Photofragmentation branching ratios for $IBr^-(CO_2)_n$ at 760 nm.

Parent Ion	I^--based	Br^--based	IBr^--based
IBr^-	I^-: 100%	NONE	NONE
$IBr^-(CO_2)_1$	I^-: 31.1% $I^-(CO_2)_1$: 64.7% **[95.8%]**	Br^-: 4.2% **[4.2%]**	NONE
$IBr^-(CO_2)_2$	I^-: 5.0% $I^-(CO_2)_1$: 72.0% $I^-(CO_2)_2$: 7.0% **[84.0%]**	Br^-: 6.2% $Br^-(CO_2)_1$: 7.3% **[13.5%]**	IBr^-: 2.5% **[2.5%]**
$IBr^-(CO_2)_3$	$I^-(CO_2)_1$: 41.8% $I^-(CO_2)_2$: 10.8% **[52.6%]**	$Br^-(CO_2)_1$: 21.6% $Br^-(CO_2)_2$: 2.4% $Br^-(CO_2)_3$: 0.3% **[24.3%]**	IBr^-: 22.1% $IBr^-(CO_2)_1$: 1.0% **[23.1%]**
$IBr^-(CO_2)_4$	$I^-(CO_2)_1$: 1.0% $I^-(CO_2)_2$: 2.2% **[3.2%]**	$Br^-(CO_2)_1$: 6.3% $Br^-(CO_2)_2$: 23.2% **[29.5%]**	IBr^-: 65.6% $IBr^-(CO_2)_1$: 1.7% **[67.3%]**
$IBr^-(CO_2)_5$	NONE	$Br^-(CO_2)_2$: 5.9% $Br^-(CO_2)_3$: 6.5% **[12.4%]**	IBr^-: 57.2% $IBr^-(CO_2)_1$: 27.5% $IBr^-(CO_2)_2$: 2.9% **[87.6%]**
$IBr^-(CO_2)_6$	NONE	$Br^-(CO_2)_3$: 12.0% **[12.0%]**	IBr^-: 19.1% $IBr^-(CO_2)_1$: 57.0% $IBr^-(CO_2)_2$: 11.0% $IBr^-(CO_2)_3$: 0.3% **[88.0%]**
$IBr^-(CO_2)_7$	NONE	$Br^-(CO_2)_4$: 1.7% $Br^-(CO_2)_5$: 1.0% **[2.7%]**	IBr^-: 0.9% $IBr^-(CO_2)_1$: 29.5% $IBr^-(CO_2)_2$: 51.8% $IBr^-(CO_2)_3$: 12.9% $IBr^-(CO_2)_4$: 2.2% **[97.3%]**
$IBr^-(CO_2)_8$	NONE	NONE	$IBr^-(CO_2)_1$: 3.3% $IBr^-(CO_2)_2$: 34.4% $IBr^-(CO_2)_3$: 45.2% $IBr^-(CO_2)_4$: 15.8% $IBr^-(CO_2)_5$: 1.3% **[100%]**

$IBr^-(CO_2)_9$	NONE	NONE	$IBr^-(CO_2)_2$: 8.9% $IBr^-(CO_2)_3$: 42.4% $IBr^-(CO_2)_4$: 36.3% $IBr^-(CO_2)_5$: 11.2% $IBr^-(CO_2)_6$: 1.2% **[100%]**
$IBr^-(CO_2)_{10}$	NONE	NONE	$IBr^-(CO_2)_3$: 13.9% $IBr^-(CO_2)_4$: 45.5% $IBr^-(CO_2)_5$: 30.7% $IBr^-(CO_2)_6$: 9.9% **[100%]**
$IBr^-(CO_2)_{11}$	NONE	NONE	$IBr^-(CO_2)_4$: 21.1% $IBr^-(CO_2)_5$: 43.9% $IBr^-(CO_2)_6$: 27.5% $IBr^-(CO_2)_7$: 8.6% **[100%]**
$IBr^-(CO_2)_{12}$	NONE	NONE	$IBr^-(CO_2)_5$: 34.0% $IBr^-(CO_2)_6$: 48.4% $IBr^-(CO_2)_7$: 17.6% **[100%]**
$IBr^-(CO_2)_{13}$	NONE	NONE	$IBr^-(CO_2)_7$: 86.9% $IBr^-(CO_2)_8$: 13.1% **[100%]**
$IBr^-(CO_2)_{14}$	NONE	NONE	$IBr^-(CO_2)_7$: 59.3% $IBr^-(CO_2)_8$: 40.7% **[100%]**

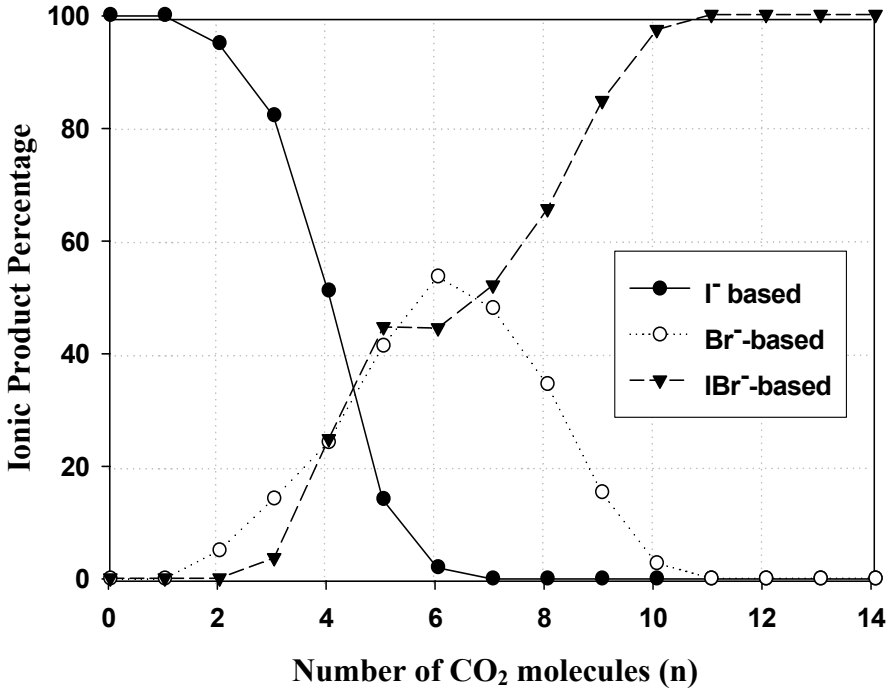

Figure 3.7: Photofragmentation products of $IBr^-(CO_2)_n$ cluster ions upon excitation to the A' $^2\Pi$ state with 675 nm photons and an energy release of 0.55 eV on the state.

Table 3.3: Photofragmentation branching ratios for $IBr^-(CO_2)_n$ at 675 nm.

Parent Ion	I^--based	Br^--based	IBr^--based
IBr^-	I^-: 100%	NONE	NONE
$IBr^-(CO_2)_1$	I^-: 18.0% $I^-(CO_2)_1$: 82.0% **[100.0%]**	NONE	NONE
$IBr^-(CO_2)_2$	I^-: 4.0% $I^-(CO_2)_1$: 83.0% $I^-(CO_2)_2$: 8.0% **[95.0%]**	Br^-: 3.0% $Br^-(CO_2)_1$: 2.0% **[5.0%]**	NONE
$IBr^-(CO_2)_3$	$I^-(CO_2)_1$: 57.2% $I^-(CO_2)_2$: 25.0% **[82.2%]**	Br^-: 4.0% $Br^-(CO_2)_2$: 10.2% **[14.2%]**	IBr^-: 3.6% **[3.6%]**
$IBr^-(CO_2)_4$	$I^-(CO_2)_1$: 11.5% $I^-(CO_2)_2$: 36.8% $I^-(CO_2)_3$: 2.8% **[51.1%]**	$Br^-(CO_2)_1$: 16.1% $Br^-(CO_2)_2$: 4.1% $Br^-(CO_2)_3$: 1.7% $Br^-(CO_2)_4$: 2.3% **[24.2%]**	IBr^-: 20.0% $IBr^-(CO_2)_1$: 1.6% $IBr^-(CO_2)_2$: 3.1% **[24.7%]**
$IBr^-(CO_2)_5$	$I^-(CO_2)_3$: 14.1% **[14.1%]**	$Br^-(CO_2)_2$: 27.0% $Br^-(CO_2)_3$: 2.8% $Br^-(CO_2)_4$: 8.5% $Br^-(CO_2)_5$: 3.0% **[41.3%]**	IBr^-: 39.7% $IBr^-(CO_2)_1$: 4.9% **[44.6%]**
$IBr^-(CO_2)_6$	$I^-(CO_2)_3$: 2.0% **[2.0%]**	$Br^-(CO_2)_3$: 6.9% $Br^-(CO_2)_4$: 2.2% $Br^-(CO_2)_5$: 31.4% $Br^-(CO_2)_6$: 13.1% **[53.6%]**	IBr^-: 23.9% $IBr^-(CO_2)_1$: 15.6% $IBr^-(CO_2)_2$: 1.8% $IBr^-(CO_2)_3$: 3.1% **[44.4%]**
$IBr^-(CO_2)_7$	NONE	$Br^-(CO_2)_4$: 2.2% $Br^-(CO_2)_5$: 1.9% $Br^-(CO_2)_6$: 39.0% $Br^-(CO_2)_7$: 5.0% **[48.0%]**	IBr^-: 7.2% $IBr^-(CO_2)_1$: 31.9% $IBr^-(CO_2)_2$: 8.5% $IBr^-(CO_2)_3$: 2.2% $IBr^-(CO_2)_4$: 2.2% **[52.0%]**
$IBr^-(CO_2)_8$	NONE	$Br^-(CO_2)_7$: 34.5% **[34.5%]**	$IBr^-(CO_2)_1$: 8.9% $IBr^-(CO_2)_2$: 36.3% $IBr^-(CO_2)_3$: 20.3% **[65.5%]**
$IBr^-(CO_2)_9$	NONE	$Br^-(CO_2)_7$: 5.3% $Br^-(CO_2)_8$: 10.0% **[15.3%]**	$IBr^-(CO_2)_1$: 7.7% $IBr^-(CO_2)_2$: 36.8% $IBr^-(CO_2)_3$: 32.5% $IBr^-(CO_2)_4$: 7.8% **[84.7%]**

$IBr^-(CO_2)_{10}$	NONE	$Br^-(CO_2)_8$: 2.7% **[2.7%]**	$IBr^-(CO_2)_2$: 12.2% $IBr^-(CO_2)_3$: 46.4% $IBr^-(CO_2)_4$: 30.9% $IBr^-(CO_2)_5$: 5.6% $IBr^-(CO_2)_6$: 2.2% **[97.3%]**
$IBr^-(CO_2)_{11}$	NONE	NONE	$IBr^-(CO_2)_3$: 21.6% $IBr^-(CO_2)_4$: 50.4% $IBr^-(CO_2)_5$: 25.4% $IBr^-(CO_2)_6$: 2.6% **[100%]**
$IBr^-(CO_2)_{12}$	NONE	NONE	$IBr^-(CO_2)_4$: 35.1% $IBr^-(CO_2)_5$: 46.1% $IBr^-(CO_2)_6$: 17.9% $IBr^-(CO_2)_7$: 0.9% **[100%]**
$IBr^-(CO_2)_{13}$	NONE	NONE	$IBr^-(CO_2)_5$: 43.3% $IBr^-(CO_2)_6$: 47.0% $IBr^-(CO_2)_7$: 9.7% **[100%]**
$IBr^-(CO_2)_{14}$	NONE	NONE	$IBr^-(CO_2)_5$: 3.0% $IBr^-(CO_2)_6$: 48.3% $IBr^-(CO_2)_7$: 41.7% $IBr^-(CO_2)_8$: 7.0% **[100%]**

produces the first IBr^--based recombined products on the ground state. As the number of CO_2 solvents is increased, the recombined products quickly dominate, and the "direct," I^--based dissociation products disappear. The charge transfer Br^--based products persist in small quantities up to n = 8, after which the only products present correspond to recombination on the ground electronic state. Although Br^--based products are observed only for 1–7 solvent molecules, solvent driven charge transfer is clearly demonstrated to occur before recombination.

Photofragmentation is also carried out at a bluer wavelength in the A' band to determine the effect of a larger kinetic energy release on the photoproduct distributions. The wavelength 675 nm provides a kinetic energy release of approximately 0.2 eV greater than for 760 and 790 nm excitation. The photoproduct distributions at 675 nm are shown in Fig. 3.7. As in the case of excitation with the other two wavelengths, unsolvated IBr^- produces only I^- as a photoproduct. With the addition of the second solvent, the charge transfer Br^--based products begin to appear. The first recombined IBr^--based products are formed with the third solvent molecule. The I^--based products persist until n = 7. The Br^--based products reach percentages of near 60% of the total products before disappearing by n = 11 when recombination on the ground state becomes 100%.

The recombination efficiency as a function of cluster size for the three excitation wavelengths is shown in Fig. 3.8. The approximate locations of each wavelength within the A' band are also shown. The curves for both 760 and 790 nm, which have nearly equal kinetic energy release on A', are nearly identical. Both show recombination at n = 2 and reach 100% recombination at n = 8. The 675 nm curve

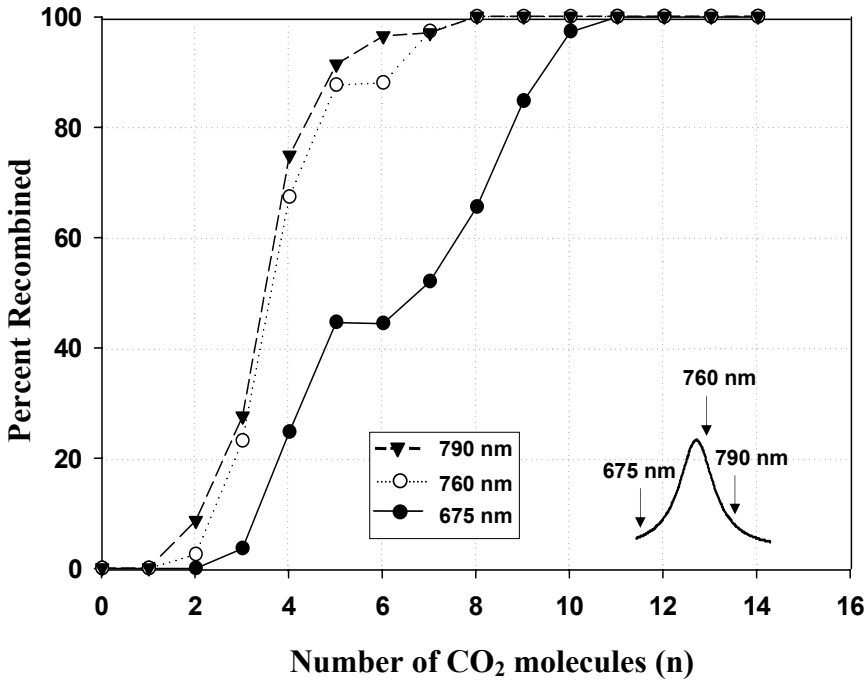

Figure 3.8: Recombination efficiency across the A' absorption band in $IBr^-(CO_2)_n$ cluster ions. The excitation wavelengths are 790, 760, and 675 nm corresponding to energy releases on A' of 0.30, 0.35, and 0.55 eV, respectively. The locations of the wavelengths on the A' band are also shown in the inset.

shows the first recombined products at n = 3 and does not reach 100% recombination until n =11. The additional 0.2 eV in kinetic energy release is roughly the binding energy of one CO_2 to IBr^-. This binding energy value is determined below. This leads to the prediction that the 675 nm recombination curve should be shifted one CO_2 solvent higher. This is indeed the case for the onset of recombination on the ground state where this occurs at n = 2 for 790 and 760 nm and at n = 3 for 675 nm. However, the clusters in the n = 5–11 range show very different behavior for 675 nm. The solvent shift is almost four solvents compared to the other wavelengths and the Br^--based products reach a much higher percentage of the total products. The simple energetic arguments thought to be applicable cannot account for this larger than expected solvent shift. Detailed simulations, similar to those previously reported[18,19] for I_2^-, will need to be carried out to provide a complete explanation for the large solvent shift in the recombination dynamics.

3.4 Photofragmentation of $IBr^-(CO_2)_n$ upon excitation to the B 2 $^2\Sigma^+_{1/2}$ state

Photodissociation studies are carried out on mass-selected $IBr^-(CO_2)_n$ cluster ions upon excitation to the B 2 $^2\Sigma^+_{1/2}$ state in a manner analogous to that of A' $^2\Pi_{1/2}$ excitation. The B state in IBr^- is not spectroscopically characterized to the extent that A' was above. The calculated spectrum shown in Fig. 3.3 is used, along with the experimental absorption band for A', to determine the excitation wavelengths for photodissociation on B. Two convenient wavelengths for both the femto- and nanosecond laser systems are used for excitation to the B state. The wavelength 355 nm is the third harmonic of the Nd:YAG Infinity and has large pulse energies with

superior mode quality as compared to the XPO wavelengths. There is also predicted to be substantial absorption cross section at this wavelength based on the calculated spectrum with the observed experimental blue shift taken into account. The 395 nm light is the second harmonic of the 790 nm fundamental wavelength characterized above and would be used in a two-color pump-probe scheme to study the time-resolved dynamics of the $IBr^-(CO_2)_n$ clusters. The appropriate blue-shift of the calculated spectrum also puts it very near the band maximum for B state excitation. Excitation of bare IBr^- at both wavelengths produces only Br^- and I* as the photoproducts with kinetic energy releases on the B state of 1.75 and 1.4 eV for 355 and 395 nm, respectively.

The addition of CO_2 solvent molecules provides a total of five possible product channels. Channels (A), (B), and (C) that are observed for excitation to the A' state are present as well as the now energetically accessible channels:

$$IBr^-(CO_2)_n \rightarrow Br^-(CO_2)_{n-m} + mCO_2 + I^* \qquad (D)$$

$$\rightarrow I^-(CO_2)_{n-k} + kCO_2 + Br^* \qquad (E)$$

Channel (D) corresponds to direct dissociation on B, giving the expected Br^--based photoproducts. Channel (E) represents a dissociation preceded by a charge transfer from the initially formed Br^- to the spin-orbit excited I* leaving Br in a spin-orbit excited state. These two channels are separated by around 0.5 eV corresponding to the binding energy of two CO_2 solvents. Products formed on these two channels are expected to differ in two solvent molecules retained. Further solvation is then expected to lead to product formation on Channels (A), (B), and (C).

The photofragmentation products from excitation of $IBr^-(CO_2)_n$ clusters with 355 and 395 nm photons as a function of cluster size are shown in Fig. 3.9 and Fig. 3.10, respectively. The exact photoproducts formed with their percentages are shown in Tables 3.4 and 3.5. The total percentages in bold are plotted in the figures. The cluster n = 5 is the largest size studied for 395 nm with n = 11 the largest cluster for 355 nm. In both cases, the unsolvated IBr^- produces exclusively Br^- as the photoproduct. The addition of the first solvent molecules leads to the production of the charge-transfer product I^-, likely accompanied by Br*. For 355 nm dissociation, the I^--based products have reached 80% of the total products by n = 4, then level off to an apparent asymptotic value of around 65% at the largest cluster size studied. Likewise, the Br^--based products drop in percentage quickly as the number of solvents is increased, but level out at roughly 25–30% of the total products by n = 8 up to the largest cluster. The recombined products on the ground state appear at n = 7, but never reach 10% of the total products. The product distributions at 395 nm are taken over a much smaller range of cluster sizes (up to n = 5), but show the same basic trends as the 355 nm data. Although, the increase in I^--based products is not as steep as for 355 nm, the total percentage of I^--based products is greater for 395 nm. The recombination product channel also turns on one solvent faster than for 355 nm photodissociation. The solvent loss for each product is used to determine the identity of the product channel on which it is formed and is discussed below.

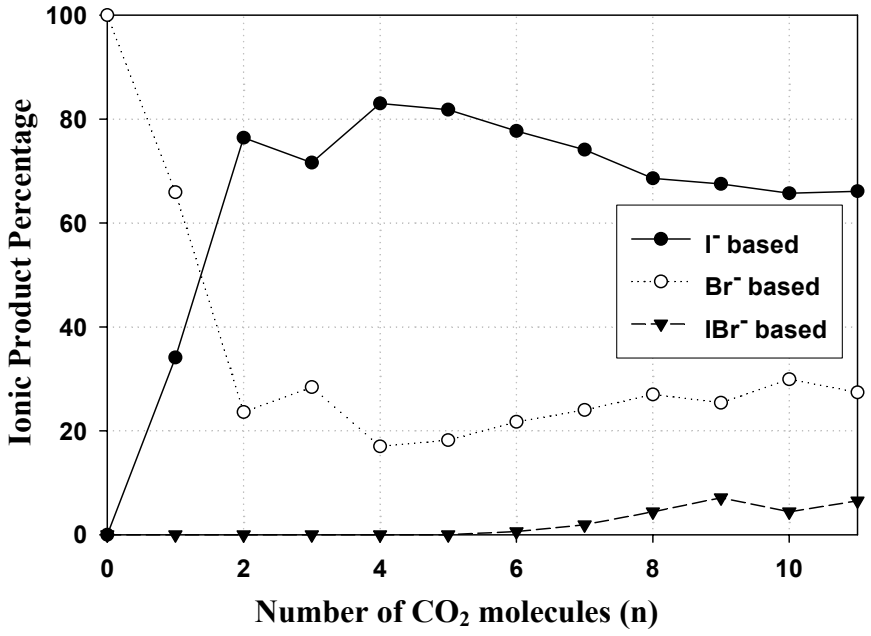

Figure 3.9: Photofragmentation products of $IBr^-(CO_2)_n$ cluster ions upon excitation to the B state with 355 nm photons and an energy release of 1.75 eV on this state.

Table 3.4: Photofragmentation branching ratios for $IBr^-(CO_2)_n$ at 355 nm.

Parent Ion	I^--based	Br^--based	IBr^--based
IBr^-	NONE	Br^-: 100%	NONE
$IBr^-(CO_2)_1$	I^-: 34.1% **[34.1%]**	Br^-: 65.9% **[65.9%]**	NONE
$IBr^-(CO_2)_2$	I^-: 48.6% $I^-(CO_2)_1$: 27.8% **[76.4%]**	Br^-: 20.5% $Br^-(CO_2)_1$: 3.1% **[23.6%]**	NONE
$IBr^-(CO_2)_3$	I^-: 26.9% $I^-(CO_2)_2$: 44.7% **[71.6%]**	Br^-: 7.3% $Br^-(CO_2)_1$: 21.1% **[28.4%]**	NONE
$IBr^-(CO_2)_4$	I^-: 20.0% $I^-(CO_2)_1$: 60.1% $I^-(CO_2)_2$: 2.9% **[83.0%]**	Br^-: 1.2% $Br^-(CO_2)_1$: 12.8% $Br^-(CO_2)_2$: 3.0% **[17.0%]**	NONE
$IBr^-(CO_2)_5$	I^-: 12.1% $I^-(CO_2)_1$: 59.1% $I^-(CO_2)_2$: 10.6% **[81.8%]**	$Br^-(CO_2)_1$: 6.3% $Br^-(CO_2)_2$: 9.7% $Br^-(CO_2)_3$: 2.2% **[18.2%]**	NONE
$IBr^-(CO_2)_6$	I^-: 6.8% $I^-(CO_2)_1$: 54.9% $I^-(CO_2)_2$: 15.4% $I^-(CO_2)_3$: 0.6% **[77.7%]**	$Br^-(CO_2)_1$: 1.3% $Br^-(CO_2)_2$: 10.1% $Br^-(CO_2)_3$: 8.8% $Br^-(CO_2)_4$: 1.5% **[21.7%]**	IBr^-: 0.6% **[0.6%]**
$IBr^-(CO_2)_7$	I^-: 2.4% $I^-(CO_2)_1$: 29.0 $I^-(CO_2)_2$: 39.1% $I^-(CO_2)_3$: 3.6% **[74.1%]**	$Br^-(CO_2)_1$: 0.8% $Br^-(CO_2)_2$: 6.1% $Br^-(CO_2)_3$: 12.3% $Br^-(CO_2)_4$: 4.5% $Br^-(CO_2)_5$: 0.3% **[24.0%]**	IBr^-: 1.9% **[1.9%]**
$IBr^-(CO_2)_8$	I^-: 0.5% $I^-(CO_2)_1$: 7.7% $I^-(CO_2)_2$: 30.7% $I^-(CO_2)_3$: 28.8% $I^-(CO_2)_4$: 0.9% **[68.6%]**	$Br^-(CO_2)_1$: 0.6% $Br^-(CO_2)_2$: 1.4% $Br^-(CO_2)_3$: 11.2% $Br^-(CO_2)_4$: 11.1% $Br^-(CO_2)_5$: 2.7% **[27.0%]**	IBr^-: 4.4% **[4.4%]**
$IBr^-(CO_2)_9$	$I^-(CO_2)_1$: 1.3% $I^-(CO_2)_2$: 11.8% $I^-(CO_2)_3$: 39.0% $I^-(CO_2)_4$: 15.0% $I^-(CO_2)_5$: 0.4% **[67.5%]**	$Br^-(CO_2)_1$: 0.6% $Br^-(CO_2)_2$: 1.4% $Br^-(CO_2)_3$: 5.8% $Br^-(CO_2)_4$: 12.1% $Br^-(CO_2)_5$: 4.9% $Br^-(CO_2)_6$: 0.6% **[25.4%]**	IBr^-: 6.7% $IBr^-(CO_2)_1$: 0.4% **[7.1%]**

$IBr^-(CO_2)_{10}$	$I^-(CO_2)_1$: 0.4% $I^-(CO_2)_2$: 3.3% $I^-(CO_2)_3$: 19.7% $I^-(CO_2)_4$: 35.5% $I^-(CO_2)_5$: 7.0% **[65.7%]**	$Br^-(CO_2)_3$: 3.3% $Br^-(CO_2)_4$: 10.8% $Br^-(CO_2)_5$: 13.2% $Br^-(CO_2)_6$: 2.6% **[29.9%]**	IBr^-: 3.4% $IBr^-(CO_2)_1$: 1.0% **[4.4%]**
$IBr^-(CO_2)_{11}$	$I^-(CO_2)_2$: 0.2% $I^-(CO_2)_3$: 8.6% $I^-(CO_2)_4$: 26.6% $I^-(CO_2)_5$: 28.5% $I^-(CO_2)_6$: 2.2% **[66.1%]**	$Br^-(CO_2)_2$: 0.3% $Br^-(CO_2)_3$: 4.7% $Br^-(CO_2)_4$: 7.2% $Br^-(CO_2)_5$: 11.6% $Br^-(CO_2)_6$: 3.6% **[27.4%]**	IBr^-: 3.0% $IBr^-(CO_2)_1$: 2.9% $IBr^-(CO_2)_2$: 0.6% **[6.5%]**

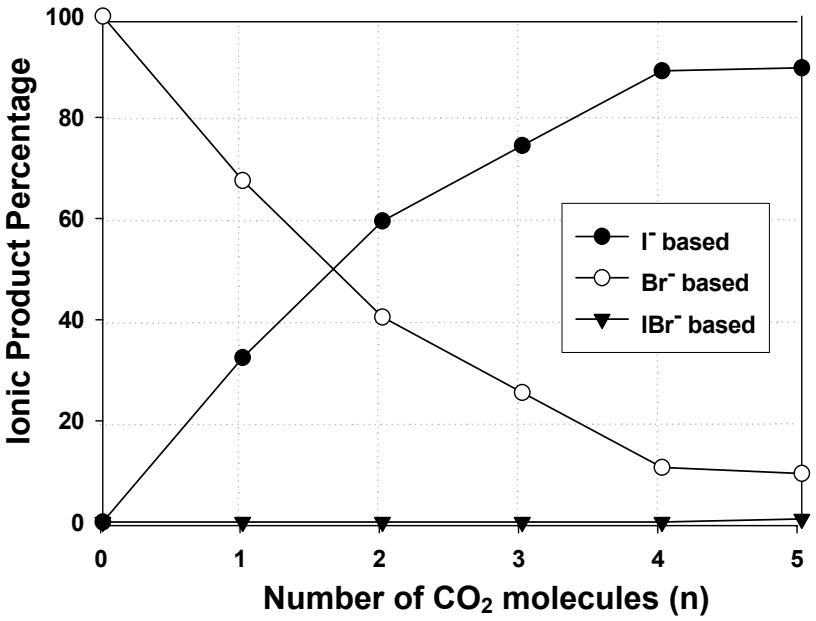

Figure 3.10: Photofragmentation products of $IBr^-(CO_2)_n$ cluster ions upon excitation to the B state with 395 nm photons and an energy release of 1.4 eV on this state.

Table 3.5: Photofragmentation branching ratios for $IBr^-(CO_2)_n$ at 395 nm.

Parent Ion	I^--based	Br^--based	IBr^--based
IBr^-	NONE	Br^-: 100%	NONE
$IBr^-(CO_2)_1$	I^-: 32.5% **[32.5%]**	Br^-: 67.5% **[67.5%]**	NONE
$IBr^-(CO_2)_2$	I^-: 27.4% $I^-(CO_2)_1$: 32.2% **[59.5%]**	Br^-: 19.1% $Br^-(CO_2)_1$: 21.4% **[40.5%]**	NONE
$IBr^-(CO_2)_3$	I^-: 5.7% $I^-(CO_2)_1$: 68.7% **[71.6%]**	Br^-: 3.6% $Br^-(CO_2)_1$: 22.0% **[25.6%]**	NONE
$IBr^-(CO_2)_4$	I^-: 15.8% $I^-(CO_2)_1$: 64.1% $I^-(CO_2)_2$: 9.3% **[91.2%]**	$Br^-(CO_2)_1$: 7.8% $Br^-(CO_2)_2$: 3.0% **[8.1%]**	NONE
$IBr^-(CO_2)_5$	I^-: 5.2% $I^-(CO_2)_1$: 61.5% $I^-(CO_2)_2$: 23.1% **[89.8%]**	$Br^-(CO_2)_1$: 2.4% $Br^-(CO_2)_2$: 5.7% $Br^-(CO_2)_3$: 1.5% **[9.6%]**	IBr^-: 0.6% **[0.6%]**

3.5 Time resolved dynamics of $IBr^-(CO_2)_8$ following excitation to the A' state

As mentioned in Ch.1, the time-resolved absorption recovery experiments provide an excellent probe for the timescales of photodissociation and subsequent recombination on the ground electronic state. After photodissociation of the IBr^- chromophore within the cluster, the cluster anion is transparent to absorption of either near-IR or UV light until the chromophore has recombined on the ground state with sufficient vibrational relaxation. This provides an overall timescale for dissociation on an excited electronic state and recombination on the ground state. By tuning the excitation wavelength, other processes such as charge-transfer and spin-orbit relaxation can be included in the overall absorption recovery time.

A one-color pump-probe experiment is carried out here on the $IBr^-(CO_2)_8$ cluster. A 790 nm pump pulse excites the chromophore within the cluster to the A' $^2\Pi_{1/2}$ dissociative state. A second 790 nm probe pulse is then absorbed by the chromophore after it has recombined and vibrationally relaxed on the ground state. The two-photon signal as a function of the delay between the pump and the probe pulses then gives the timescale for photodissociation, charge transfer from I^- to Br, and recombination and vibrational relaxation on the ground state. The cluster $IBr^-(CO_2)_8$ is chosen due to the 100% recombination after excitation to A'. This was also the most intense cluster in the mass spectra for which 100% recombination was present. Based on similar experiments[10] in $I_2^-(CO_2)_n$ clusters, the absorption recovery time after excitation to the A' state is predicted to be 10–30 ps.

The time-resolved data for $IBr^-(CO_2)_8$ are shown in Fig. 3.11. The pump and the probe wavelengths have polarizations perpendicular to one another due to beam

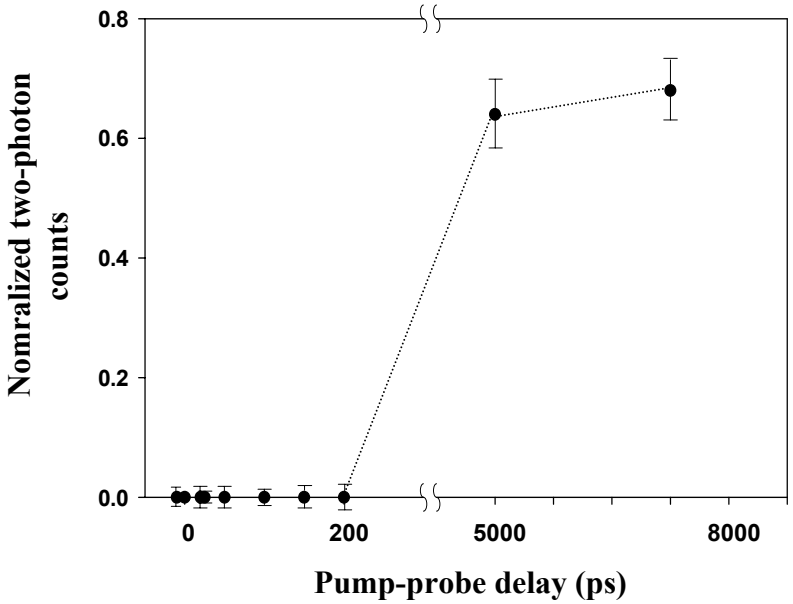

Figure 3.11: The $IBr^-(CO_2)_8$ absorption recovery as a function of time following excitation to the A' $^2\Pi$ state with a 790 nm pump pulse. A break is shown to indicate the substantial change in scale. The dashed line is simply to guide the eye.

recombination restrictions. The one-photon photofragmentation results presented in Sec. 3.3 are used to determine that $I^-(CO_2)$ is the two-photon product ion of the largest intensity for this cluster and excitation scheme. This product ion is monitored as a function of pump-probe delay to yield the absorption recovery curve. The appropriate backgrounds are subtracted to show that this two-photon product depends upon the presence of both the pump and the probe pulses and represents true two-photon signal.

The striking feature of the absorption recovery curve is that there is no detectable absorption recovery signal over the first 200 ps, the maximum delay time available using the precision delay line. The one-photon photodissociation branching ratios from above require that there must be complete absorption recovery within around 10 μs, which is the flight time from the laser interaction region to detection on the off-axis detector. A crude delay-line is set up to allow for the use of longer than 200 ps pump-probe delay times. Two data points were taken at 5 ns and 8 ns with this longer delay-line. At these long delay times, the overlap between the pump and probe pulses is poorly controlled resulting in a large uncertainty in the two data points. The curve shows the two-photon signal to be increasing from 5 ns to 8 ns, but within the experimental uncertainty it is impossible to determine if this is the case or a complete absorption recovery plateau has been reached. Nevertheless, some degree of recombination on the ground state is occurring by 5 ns with none before at least 200 ps. This is in stark contrast to the predictions made based on the ~20 ps recombination time observed for the smallest $I_2^-(CO_2)_n$ cluster (n = 12) that shows 100% recombination.[10]

3.6 Photofragmentation of $ICl^-(CO_2)_n$ upon excitation to A' at 790 nm

The photodissociation dynamics of $ICl^-(CO_2)_n$ cluster ions has been thoroughly investigated previously[8,13] with numerous excitation wavelengths. However, photofragmentation studies at wavelengths near 790 nm were not carried out. In the event that time-resolved experiments are carried out on $ICl^-(CO_2)_n$ clusters, 790 nm will be an important excitation wavelength due to the enhanced performance of the femtosecond laser system near this wavelength. The photofragmentation as a function of cluster size is carried out in an analogous manner to that described for $IBr^-(CO_2)_n$ clusters described in Sec. 3.3. Only the results are provided here as detailed explanations on the product channels and dynamics can be found elsewhere.[8,13]

The photofragmentation products as a function of cluster size after excitation with 790 nm photons are shown in Fig. 3.12. The complete product distributions are found in Table 3.6. The kinetic energy release on A' is roughly 0.25 eV. The results show qualitatively similar behavior to those previously observed[8,13] for photodissociation at 644 nm and 740 nm. The photodissociation of unsolvated ICl^- produces the expected I^- + Cl photoproducts. The addition of the first CO_2 leads to recombination on the ground state. Recombination reaches 100% at n = 2 and is 100% for n = 3. The fourth solvent molecule begins to yield Cl^--based products that then increase at the expense of the recombined products with increasing solvation. The Cl^--based products reach 100% by n = 9 with no other photoproducts present at larger clusters. Molecular dynamics simulations[17] show a Cl^--based product channel

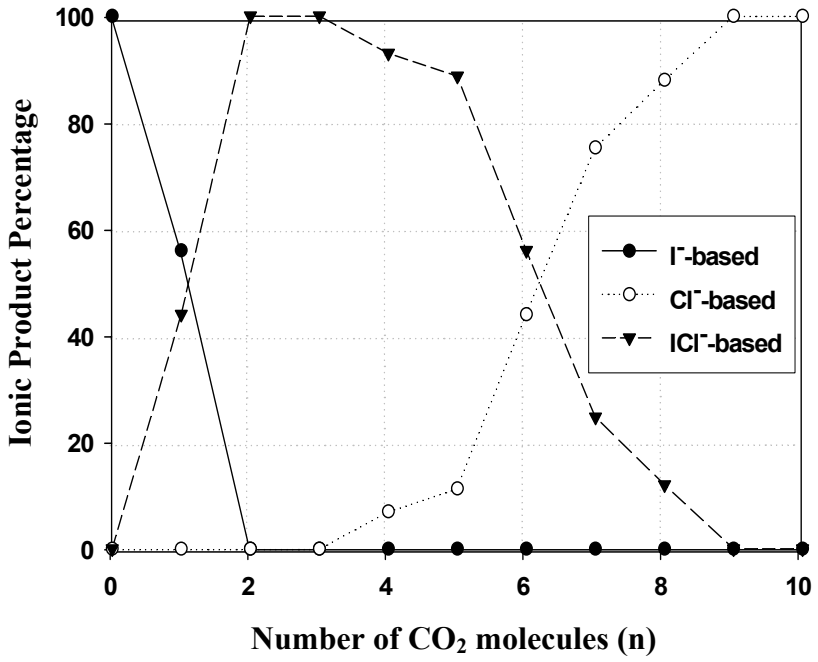

Figure 3.12: Photofragmentation products of $ICl^-(CO_2)_n$ cluster ions upon excitation to the A' $^2\Pi$ state with 790 nm photons and an energy release of 0.25 eV on the state.

Table 3.6: Photofragmentation branching ratios for $ICl^-(CO_2)_n$ at 790 nm.

Parent Ion	I^--based	Cl^--based	ICl^--based
ICl^-	I^-: 100% **[100%]**	NONE	NONE
$ICl^-(CO_2)_1$	$I^-(CO_2)_1$: 56% **[56%]**	NONE	ICl^-: 44% **[44%]**
$ICl^-(CO_2)_2$	NONE	NONE	ICl^-: 100% **[100%]**
$ICl^-(CO_2)_3$	NONE	NONE	ICl^-: 89.5% $ICl^-(CO_2)_1$: 10.5% **[100%]**
$ICl^-(CO_2)_4$	NONE	Cl^-: 7% **[7.0%]**	ICl^-: 48.5% $ICl^-(CO_2)_1$: 35.0% $ICl^-(CO_2)_2$: 9.5% **[93.0%]**
$ICl^-(CO_2)_5$	NONE	$Cl^-(CO_2)_3$: 2.9% $Cl^-(CO_2)_4$: trace $Cl^-(CO_2)_5$: 8.4% **[11.3%]**	ICl^-: 10.1% $ICl^-(CO_2)_1$: 43.3% $ICl^-(CO_2)_2$: 31.1% $ICl^-(CO_2)_3$: 4.2% **[88.7%]**
$ICl^-(CO_2)_6$	NONE	$Cl^-(CO_2)_4$: 1.0% $Cl^-(CO_2)_5$: 1.0% $Cl^-(CO_2)_6$: 42.0% **[44.0%]**	$ICl^-(CO_2)_1$: 19.0% $ICl^-(CO_2)_2$: 24.0% $ICl^-(CO_2)_3$: 13.0% **[56.0%]**
$ICl^-(CO_2)_7$	NONE	$Cl^-(CO_2)_7$: 75.3% **[75.3%]**	$ICl^-(CO_2)_1$: 2.1% $ICl^-(CO_2)_2$: 11.0% $ICl^-(CO_2)_3$: 8.8% $ICl^-(CO_2)_4$: 2.8% **[24.7%]**
$ICl^-(CO_2)_8$	NONE	$Cl^-(CO_2)_7$: 29.4% $Cl^-(CO_2)_8$: 58.6% **[88.0%]**	$ICl^-(CO_2)_3$: 7.4% $ICl^-(CO_2)_4$: 4.6% **[12.0%]**
$ICl^-(CO_2)_9$	NONE	$Cl^-(CO_2)_8$: 100% **[100%]**	NONE
$ICl^-(CO_2)_{10}$	NONE	$Cl^-(CO_2)_9$: 26.8% $Cl^-(CO_2)_{10}$: 73.2% **[100%]**	NONE

corresponding to formation of spin-orbit excited I*. Products formed on this channel would be expected to not lose any solvents. It appears that this channel may turn on at n = 5 where the solvent loss decreases dramatically to one or zero solvents from the n = 4 solvent loss. This decreased solvent loss is more apparent than in the solvent loss data after 644 nm and 740 nm excitation.[8,13] The decrease in kinetic energy release on A' at 790 nm may favor products on this spin-orbit excited I* channel.

3.7 Solute dependent photodissociation dynamics upon excitation to A' $^2\Pi_{1/2}$

The results presented in Sec. 3.3 demonstrate the dramatic effects that the presence of a small number of CO_2 solvent molecules has on the photodissociation dynamics of $IBr^-(CO_2)_n$ clusters after excitation on the A' electronic state. The dynamics of these photodissociation processes can be discussed in terms of a comparison with previous results carried out on excitation to the A' electronic state for $ICl^-(CO_2)_n$ and $I_2^-(CO_2)_n$ cluster ions.[8-10,13] The calculated potential energy curves[17,20] for ICl^- and I_2^- are shown in Fig. 3.13. The photodissociation dynamics of the three solutes are compared at wavelengths that correspond to kinetic energy releases of 0.3 eV on the A' state for each. The recombination efficiency as a function of cluster size for the three solute ions is shown in Fig. 3.14. The presence of a single CO_2 molecule is sufficient to allow for a nonadiabatic transition to the ground electronic state via a charge-transfer for both ICl^- and IBr^-. Recombination on the ground state is also present for ICl^-.with the addition of the first solvent. The second CO_2 molecule increases the fraction of ions reaching the ground state and recombining for ICl^- as well producing the first ground state recombined IBr^-

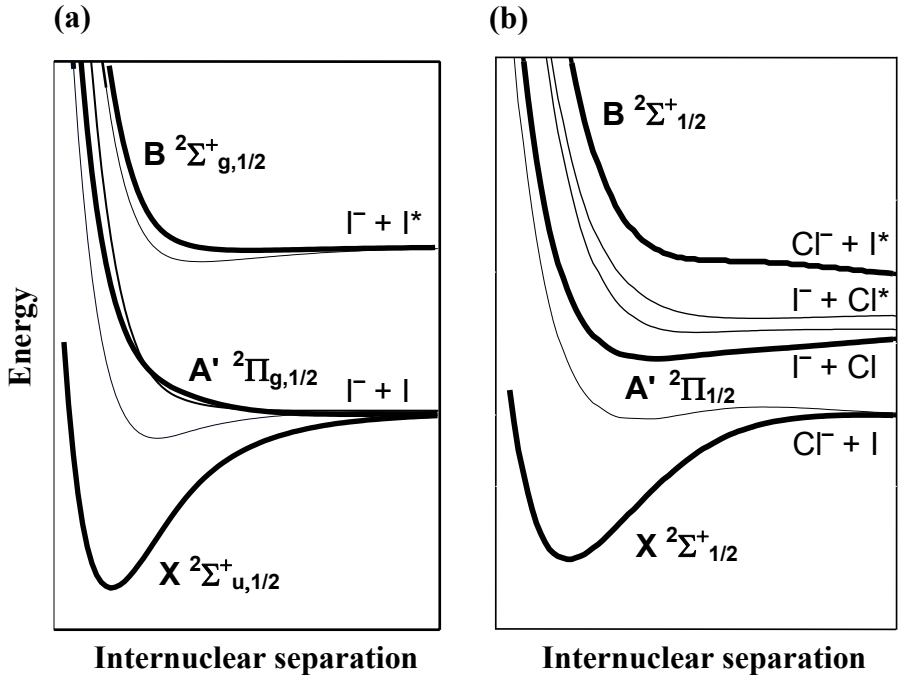

Figure 3.13: Calculated potential energy curves for (a) I_2^- and (b) ICl^- anions. The original calculations are found in references cited in the text. The states in bold are accompanied by their state labels.

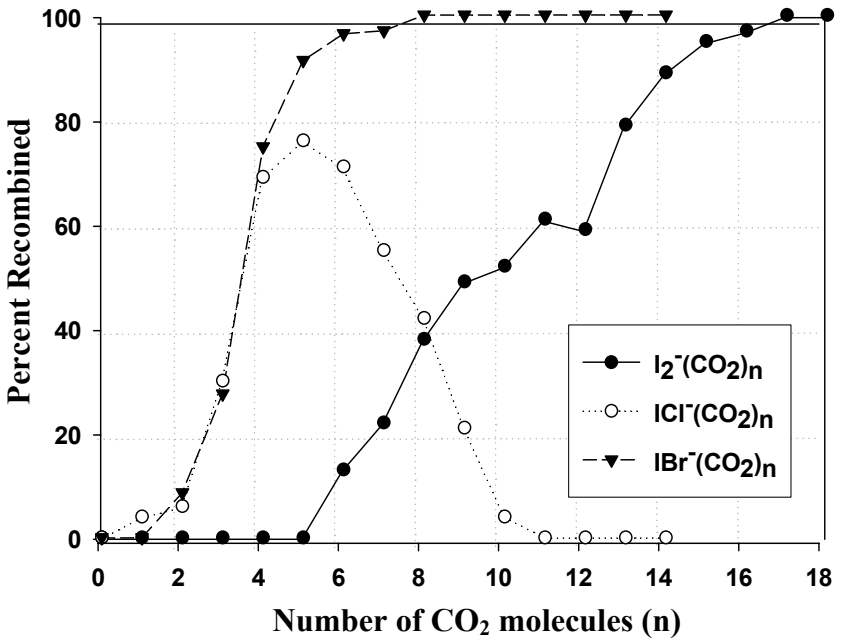

Figure 3.14: Recombination percentage for the three solutes as a function of the number of CO_2 molecules upon excitation to the A' $^2\Pi$ state. The excitation wavelengths are chosen to provide 0.3 eV energy release for each solute.

products. Increasing solvation up to n = 4 leads to increasing recombination on the ground state for both solutes.

The behavior for IBr^- and ICl^- diverge greatly for clusters larger than n = 4. The recombination fraction begins to drop dramatically eventually reaching zero by n = 10 for $ICl^-(CO_2)_n$ clusters with Cl^--based products being exclusively formed for clusters with n>9. The $IBr^-(CO_2)_n$ clusters show increasing recombination with increasing cluster size reaching 100% recombination by n = 8. This recombination behavior is similar to that of $I_2^-(CO_2)_n$ clusters where recombination reaches 100% with increasing cluster size. However, recombined products do not appear until n = 6 and 100% recombination is not reached until n = 16 for $I_2^-(CO_2)_n$.

This photodissociation behavior of the three solutes can partially be explained in terms of the properties of the solvent cages depicted in Fig. 3.15 for the three dihalide solutes. After excitation on the A' state for the three solutes, 0.3 eV must be removed from the dissociating dihalide to prevent prompt, direct dissociation on this excited electronic state. The $IBr^-(CO_2)_n$ and $I_2^-(CO_2)_n$ have the first few CO_2 molecules ($n \leq 4$) bind near the waist of the dihalide solute and only begin to fully enclose one end of the solute (the smaller Br end in the case of IBr^-) with increasing solvation (Fig. 3.15). For the $ICl^-(CO_2)_n$ clusters, the first few solvents bind to the much smaller Cl end of the solute[8,17] with subsequent solvation continuing around the Cl end (Fig. 3.14). The large recombination efficiency for small $ICl^-(CO_2)_n$ clusters is a result of the CO_2 molecules location on the Cl end of the solute. These solvents are directly in the pathway for dissociation and the favorable mass match between Cl

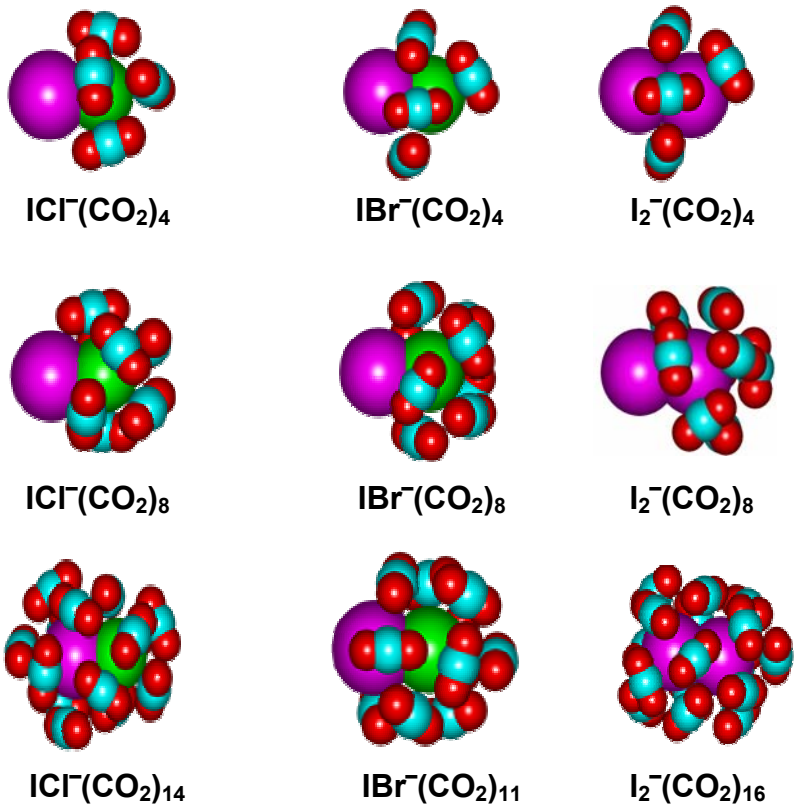

Figure 3.15: Representative cluster structures calculated for ICl^-, IBr^-, and I_2^- with various numbers of CO_2 solvent molecules. The smaller halogen is always on the right side. The reference for the original calculations is cited in the text.

(35 amu) and CO_2 (44 amu) provides effective energy transfer between the dissociating Cl and the solvent. The 0.3 eV of kinetic energy present is easily removed suppressing direct dissociation and allowing for nonadiabatic transitions to lower electronic states.

Recombination in $IBr^-(CO_2)_n$ is not observed until n = 2 due to the fact that there are no solvent molecules directly in the path of the dissociating dihalide at small cluster sizes. However, there are likely cluster structures slightly higher in energy present that have some solvation directly on the smaller Br end. This coupled with the slightly favorable mass match between Br (79 amu) and CO_2 (44 amu) leads to recombination at smaller cluster sizes. The $I_2^-(CO_2)_n$ clusters do not have solvents bound on one end of the solute nor is there a favorable mass match between I (127 amu) and CO_2 (44 amu). Recombination does not occur until n = 6, the size at which a solvent cage begins to form around one end of the I_2^- solute. Recombination also does not reach 100% until the 16^{th} CO_2 molecule caps the remaining I end closing the final pathway to direct dissociation. The recombination efficiency for the three solutes at small cluster sizes is highly dependent on both the position of the solvent molecules and the mass match between the solvents and the dissociated atoms.

The most striking difference between the recombination behavior of the three solutes is the termination of recombination on the ground state for $ICl^-(CO_2)_n$ at large cluster sizes. Both $I_2^-(CO_2)_n$ and $IBr^-(CO_2)_n$ clusters demonstrate the intuitive behavior of increasing recombination with increasing solvation. This agrees well with the picture of a larger solvent cage providing a stronger physical barrier to direct dissociation of the dihalide anion. Upon excitation to the A' state in $ICl^-(CO_2)_n$, there

are two deep minima on the potential surface.[17] The global minimum corresponds to solvated ICl^-. However, the system likely accesses a deep local minimum corresponding to solvated Cl^-. The minimum well deepens with increasing solvation making it less likely for the system to surmount and produce recombined products on the timescale of the experiment (~ 10 μs). This leads to the observation of only Cl^--based products at large cluster sizes. The IBr^- electronic structure calculations[1] indicate that the A' is not purely repulsive with a shallow well present at 3.5 Å. The presence of a solvent would deepen this well and trap the dissociating anion at small internuclear distances not allowing it to reach internuclear separations where transitions to lower electronic states occur. The well present accounts for the much longer recombination time observed for $IBr^-(CO_2)_8$ as compared to $I_2^-(CO_2)_n$ clusters. However, the well is not as deep as for $ICl^-(CO_2)_n$ clusters due to the differences in solvation energies for Cl^- and Br^-. The atomic radii of Cl^- and Br^- are 1.81Å and 1.96Å , respectively. These correspond to solvation energies for each of –347 kJ/mol and –321 kJ/mol obtained from the Born equation.[21] This shallower well for IBr^- allows for recombination times much shorter than 10 μs. Sanov and co-workers have also observed the minimum in IBr^- using time-resolved photoelectron imaging studies of IBr^- excited to the A' $^2\Pi_{1/2}$ electronic state.[22]

3.8 Dissociation following excitation to the 2 B $^2\Sigma^+_{1/2}$ state

The recombination efficiency as a function of solute following excitation to the B electronic state is shown in Fig. 3.16. The recombination percentage for IBr^- is much less than that of ICl^- and I_2^- at similar cluster sizes. Recombined products

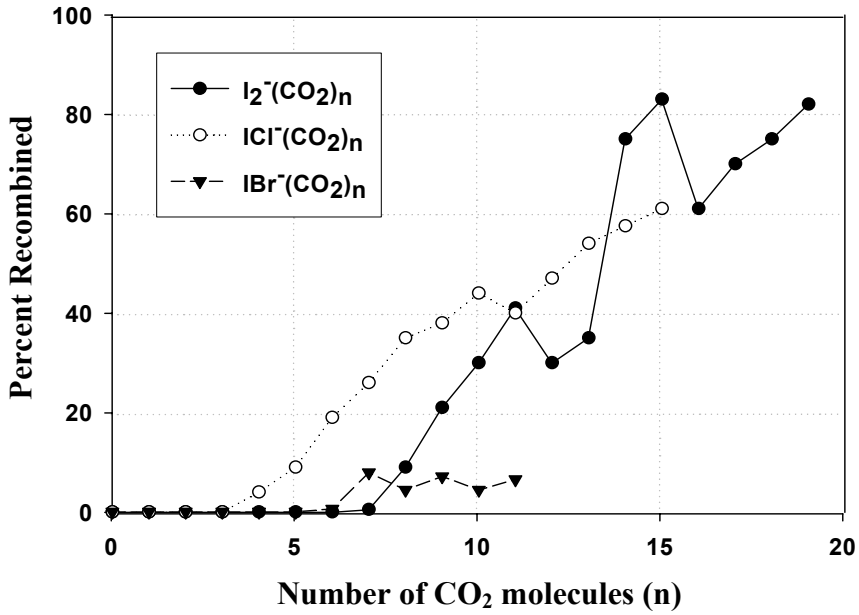

Figure 3.16: Recombination percentage for the three solutes as a function of number of CO_2 molecules following excitation to the B $2\,^2\Sigma$ state. The excitation wavelengths and corresponding energy releases on the B state are 1.2 eV for $I_2^-(CO_2)$n, 1.5 eV for $ICl^-(CO_2)_n$, and 1.75 eV for $IBr^-(CO_2)_n$.

initially appear at the same cluster sizes for IBr^- and I_2^- with the recombined channel turning on three CO_2 solvents earlier for ICl^-. The $ICl^-(CO_2)_n$ clusters show increasing recombination on the ground state with increasing solvation in sharp contrast to the recombination behavior after excitation to the A' state. Molecular dynamics simulations[17] of the recombination dynamics after excitation to the B state show that the dissociated ICl^- does not access the local minimum present in A' dissociation allowing for efficient recombination with increasing cluster size. The $IBr^-(CO_2)_n$ clusters show very little recombination at the largest cluster sizes studied with less than 10% of the total products at n = 11, the largest cluster studied. Excitation on A' conversely reaches 100% recombination by n = 8. The $I_2^-(CO_2)_n$ recombination shows the overall trend of increasing with increasing cluster size similar to $ICl^-(CO_2)_n$ behavior. The recombination rate for $I_2^-(CO_2)_n$ does not smoothly increase as for $ICl^-(CO_2)_n$, however. The recombination is more sensitive to the number of solvents and thus the structure of the CO_2 solvent cage. The symmetric I_2^- solute likely depends more on the solvent structure to facilitate spin-orbit relaxation of I before recombination than the asymmetric solutes leading to a much stronger dependence on the number of solvent molecules present.

3.9 Time-resolved recombination dynamics

The time-resolved recombination dynamics for $IBr^-(CO_2)_8$ after excitation to the A' $^2\Pi_{1/2}$ state show a recombination time of more than 200 ps. Measurable recombination is observed on the 5 to 8 ns timescale. This cluster size produces recombination on the ground state for every cluster ion excited. When compared to

similar experiments[10,12] carried out on $I_2^-(CO_2)_n$ clusters, the IBr^- recombination time is some two orders of magnitude slower than for the corresponding $I_2^-(CO_2)_n$ clusters that exhibit complete recombination. The discrepancies in the recombination times for these two systems must be due to the presence of the previously mentioned minimum well present in the IBr^- A' $^2\Pi_{1/2}$ potential that is absent for I_2^-.

The well thought to be present in ICl^- is deeper than that found on IBr^- due to the larger solvation energy for Cl^- compared to Br^-. This deeper well does not allow for recombination on the 10 μs timescale necessary for detection on the off-axis detector. This is manifested in the observation of only Cl^--based products at large cluster sizes in $ICl^-(CO_2)_n$. The IBr^- well is sufficient to provide early trapping of the anion, but is shallow enough to allow the anion to escape and produce recombination on the ground state on the nanosecond timescale. This picture of a shallow well accounts for the very slow, but complete recombination for $IBr^-(CO_2)_{n\geq 8}$ after excitation to the A' $^2\Pi_{1/2}$ state. This will need to be comfirmed through extensive molecular dynamics simulations similar to those performed for A' excitation in $ICl^-(CO_2)_n$ and $I_2^-(CO_2)_n$ clusters.[17,18,23,24]

3.10 Solvent evaporation energetics

Analysis of the number of solvent molecules attached to the ionic photoproducts provides important information on the approximate ion-solvent binding energies as well as identification of the electronic states from which dissociated photoproducts arise. The first step is the determination of the average energy removal upon evaporation of a single CO_2 molecule from the IBr^- solute

anion. Analysis of the number of solvent molecules remaining on recombined IBr^--based products after excitation to A' with three excitation energies provides the total energy (solvent binding energy + kinetic energy) removed by evaporation of a CO_2 solvent molecule.

The average solvent loss for the recombined products, as well as the other product channels, can be determined from the photofragmentation branching ratios shown in Tables 3.1, 3.2, and 3.3 for excitation of $IBr^-(CO_2)_n$ clusters to the A' state. The average number of solvents lost through evaporation for each of the three types of products after excitation to A' at 790 nm is shown in Fig. 3.17. The data in the figure is obtained from the branching ratios found in Table 3.1. Similar graphs can be constructed from the branching ratios for 760 nm and 675 nm excitations, but are not shown here. To determine the average energy loss for each CO_2, the number of solvents lost for the recombined IBr^--based products must be determined for large initial cluster sizes. For an accurate determination of the energy removal upon solvent evaporation, the IBr^- must undergo sufficient vibrational relaxation on the ground state potential to reach the vibrational levels occupied prior to photoexcitation. Larger numbers of solvents initially present in the clusters should ensure that complete vibrational relaxation is taking place on the ground state. The solvent loss for the recombined products at the three A' excitation wavelengths are shown as a function of initial cluster size in Fig. 3.18. The average number of solvent lost is determined in the n = 10–14 cluster range for each wavelength. This number is divided by the photon energy to yield the average energy removed by each solvent evaporated. The values for each wavelength are then averaged to yield an overall

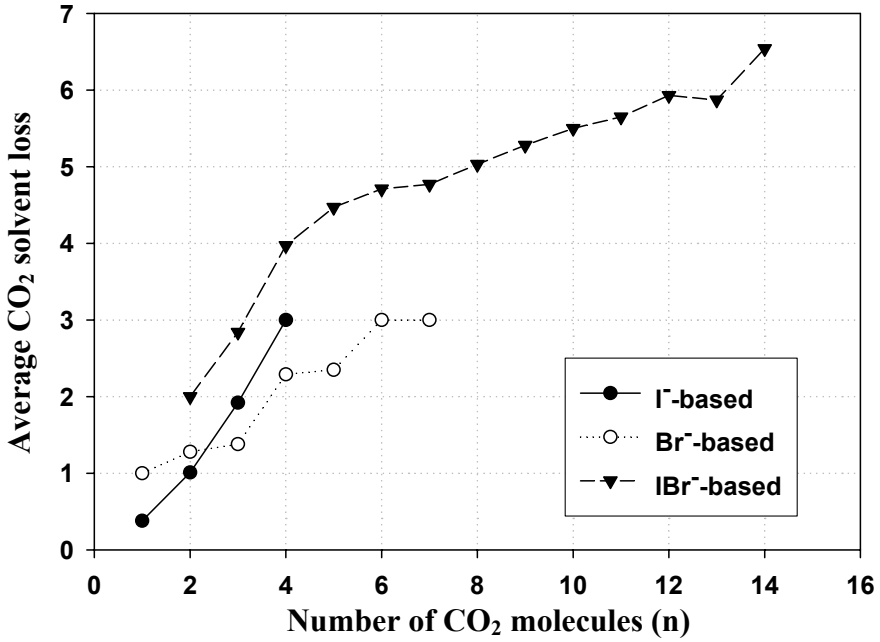

Figure 3.17: Average number of solvent loss for the three product channels after excitation with 790 nm to A' as a function of initial cluster size (n).

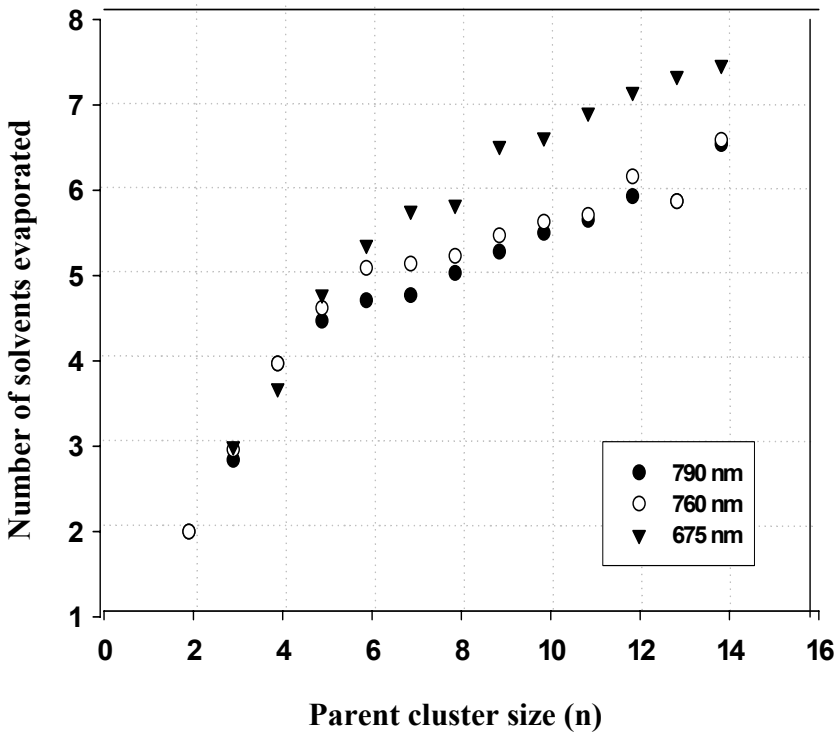

Figure 3.18: Average solvent loss for the recombined products after excitation to A' in $IBr^-(CO_2)_n$ clusters at the three labeled wavelengths as a function of initial cluster size.

average energy removal of 263 ± 12 meV per CO_2 evaporated from IBr^-. This quantity is consistent with the average CO_2 energy removal observed[9] of 250 meV for $I_2^-(CO_2)_n$ clusters. The solvent binding energy is determined by the use of a statistical model[25] to estimate the kinetic energy associated with solvent evaporation. This kinetic energy amounts to around 40 meV for $IBr^-(CO_2)_n$ clusters giving an average solvent binding energy of 223 meV for 7–15 solvent molecules attached to IBr^-. This number will increase slightly at smaller cluster sizes when there is preferential binding around the smaller Br end of the solute. However, this model adds no uncertainty to the assignment of the electronic states on which dissociation takes place as only the total energy removal (kinetic energy + solvent binding energy) is required.

Excitation to the A' $^2\Pi_{1/2}$ state

The photofragmentation branching ratios for the excitation to the A' electronic state in $IBr^-(CO_2)_n$ clusters were presented in Sec. 3.3. The excitation yields the photodissociation products I^- + Br for the unsolvated IBr^- solute. Solvation produced not only the expected I^--based products, but Br^--based products on the ground state following a charge-transfer event as well as recombined IBr^--based products on the ground state. The excitation with 760 and 790 nm photons leads to a kinetic energy release of about 0.3 eV or roughly the removal energy of one CO_2 solvent molecule based on the discussion above. The solvent loss for each product is used to determine the identity of the electronic state on which the products are formed. With only 0.3 eV kinetic energy release during dissociation on A', the I^--based products are expected to only lose a single CO_2 molecule. However, the data in Tables 3.1 and 3.2

show more than one solvent loss for clusters sizes up to n = 4 where the I^--based product channel turns off. This larger solvent loss is a result of direct dissociation of I^- from the IBr^- clusters occurring faster than the solvent is able to rearrange to solvate the newly formed atomic anion. The I^--based products are then formed with fewer than expected solvents. A statistical equilibrium model is not applicable to these small clusters.

For the larger clusters studied ($n \geq 13$), the average solvent loss has reached a plateau at around six CO_2 solvents lost. This is the expected solvent loss for complete vibrational relaxation on the ground electronic state for the IBr^--based products. For instance, after excitation on A' with 790 nm, complete vibrational relaxation on the ground state requires dissipating the entire 790 nm photon energy of 1.57 eV. This is equal to the energy of the removal of six CO_2 solvent molecules using the value of 263 meV from above. Complete vibrational relaxation then requires the removal of six CO_2 molecules. It should be noted that at n = 8, the cluster size for which the time-resolved experiment was carried out, there has been only a loss of five CO_2 leaving the recombined products vibrationally excited. However, the additional vibrational exciation equal to the removal of one CO_2 does not significantly shift the absorption spectrum to affect the time-resolved experiments.

Excitation to the B 2 $^2\Sigma^+_{1/2}$ state

The solvent evaportation analysis becomes critical for product state identification when products can be formed in multiple spin-orbit states of the neutral. For instance, excitation with 355 nm light to the B 2 $^2\Sigma^+_{1/2}$ state produces Br^--based that could be associated with either an I atom product (X $^2\Sigma$ state dissociation) or an

I* product (B 2 $^2\Sigma$ state dissociation). The solvent loss as a function of initial cluster size for 355 nm excitation on the B state is shown in Fig. 3.19 based on the data from Table 3.4. Excitation on B with 355 nm leads to a kinetic energy release of 1.75 eV. With the average energy removal of around 260 meV per CO_2 solvent, dissociation on B leading to Br^--based products is expected to show a loss of 6–7 CO_2 solvents corresponding to the amount of kinetic energy release. Dissociation on the X state producing Br^--based would lead to a loss of 10–11 solvents reflecting the additional loss equivalent to the spin-orbit splitting energy of I atom. Analysis of the solvent loss for the Br^--based products at 355 nm shows, for instance, that the Br^- solvent distribution for the largest cluster studied, $IBr^-(CO_2)_{11}$, peaks at $Br^-(CO_2)_5$ with a loss of six solvents. This confirms, based on the argument above, that the Br^- photodissociation products are formed exclusively via direct dissociation on the initially excited B state. The same conclusion is true for the Br^--based products at all other cluster sizes studied.

The I^--based products from excitation to the B 2 $^2\Sigma^+_{1/2}$ state have very similar behavior, with the average solvent loss being about one CO_2 solvent less than for the Br^--based products. This result shows that the I^--based products are formed on the a' 2 $^2\Pi_{1/2}$ state, leading to I^- + Br*. The alternative product channel corresponding to dissociation on the A' $^2\Pi_{1/2}$ state producing I^- + Br is much closer in energy to the I^- + Br* channel than are the two Br^- channels with an asymptotic energy spacing of only 0.47 eV, or less than two CO_2 solvents. It could be argued that this close energy spacing makes the product channel assignment ambiguous. However, the very small recombination fraction does not support this alternative assignment. The A'

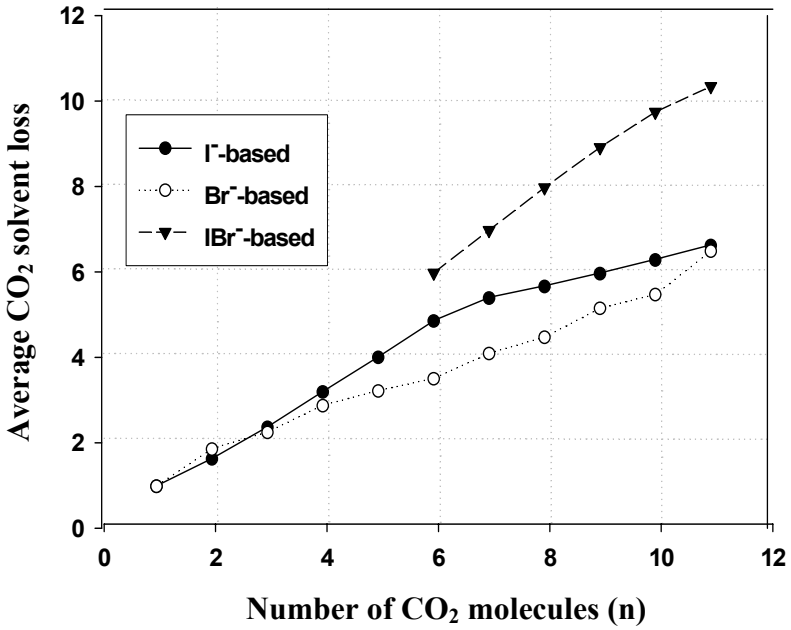

Figure 3.19: Average number of solvent loss for the three product channels after excitation with 355 nm to B as a function of initial cluster size (n).

photofragmentation branching ratios demonstrated that recombination on the ground state is very efficient for even small cluster sizes after excitation on A'. In the case of B state excitation, if the I^--based products were being formed on A' then a larger fraction of recombined products should accompany this than observed.

The dynamics following excitation to the B state for all cluster sizes with more than two CO_2 solvents is determined by the initial curve crossing between the B $2\ ^2\Sigma^+_{1/2}$ and a' $2\ ^2\Pi_{1/2}$ states. This is very similar to the Marcus-like picture of the dynamics used to describe the results for excitation of $I_2^-(CO_2)_n$ clusters to the B state.[19,24] There is an initial step in the dynamics involving either a charge transfer from Br^- to I* or solvent rearrangement around the newly formed Br^- charge center. After the branching ratio is determined for solvent reorganization and direct dissociation on B versus a charge transfer followed by dissociation on a' at a minimum cluster size, subsequent solvation does not affect this branching ratio.

3.11 Conclusions

The photodissociation dynamics of $IBr^-(CO_2)_n$ clusters were studied to determine the effects of solvation on a mixed dihalide anion. The bare solute, IBr^-, was first spectroscopically characterized and compared to theoretical calculations. These results were used to determine wavelengths for excitation to the A' $^2\Pi_{1/2}$ and B $2\ ^2\Sigma^+_{1/2}$ electronic states of IBr^- corresponding to I^- + Br and Br^- + I* photoproducts, respectively. The IBr^- anion was also shown to possess a modest bond strength of 1.10 eV, making the solvent binding energy of a small number of CO_2 molecules comparable to the bond energy. The addition of CO_2 solvent molecules demonstrated

the central role of the solvent configuration in determining the photodissociation dynamics. The solvent was shown to drive such processes as charge-transfer, spin-orbit relaxation, and recombination and vibrational relaxation on the ground state. Solvent evaporation was used to determine the binding energy of a CO_2 solvent to the IBr^- solute as well as to identify product channels where the production of an anionic product may take place on multiple electronic corresponding to the different spin-orbit states of the accompanying neutral product. The photofragmentation branching ratios were used to carry out a time-resolved experiment on $IBr^-(CO_2)_8$ to determine the timescale for recombination on the ground electronic state after A' excitation. The recombination time was found to be unexpected long at 5 ns when compared to similar experiments in $I_2^-(CO_2)_n$. The presence of a shallow well on A' seems to trap the dissociating anion solute leading to the longer than expected recombination time. The photodissociation behavior was compared to results from $ICl^-(CO_2)_n$ and $I_2^-(CO_2)_n$ clusters demonstrating the importance of the solute properties in determining the dynamics of solvation.

Chapter 3 References

[1] T. Sanford, S.-Y. Han, M. A. Thompson, R. Parson, and W. C. Lineberger, **to be published** (2004).

[2] M. A. Thompson and R. Parson, unpublished results (2004).

[3] C. E. Moore, *Atomic Energy Levels*. (National Bureau of Standards, Washington, D.C., 1949).

[4] M. W. Chase, Jr., C. A. Davies, J. R. Downey, Jr., D. J. Frurip, R. A. McDonald, and A. N. Syverud, JANAF Thermochemical Tables (J.Phys.Chem. Ref. Data 14), 421 (1985).

[5] A. Sanov, T. Sanford, L. J. Butler, J. Vala, R. Kosloff, and W. C. Lineberger, J. Phys. Chem. A **103**, 10244 (1999).

[6] E. Gershgoren and S. Ruhman, private communication.

[7] J. M. Papanikolas, Ph.D. Thesis, University of Colorado, 1994.

[8] M. E. Nadal, Ph.D. Thesis, University of Colorado, 1996.

[9] J. M. Papanikolas, J. R. Gord, N. E. Levinger, D. Ray, V. Vorsa, and W. C. Lineberger, J. Phys. Chem. **95** (21), 8028 (1991).

[10] J. M. Papanikolas, V. Vorsa, M. E. Nadal, P. J. Campagnola, H. K. Buchenau, and W. C. Lineberger, J. Chem. Phys. **99** (11), 8733 (1993).

[11] J. M. Papanikolas, V. Vorsa, M. E. Nadal, P. J. Campagnola, J. R. Gord, and W. C. Lineberger, J. Chem. Phys. **97** (9), 7002 (1992).

[12] V. Vorsa, S. Nandi, P. J. Campagnola, M. Larsson, and W. C. Lineberger, J. Chem. Phys. **106** (4), 1402 (1997).

[13] M. E. Nadal, P. D. Kleiber, and W. C. Lineberger, J. Chem. Phys. **105** (2), 504 (1996).

[14] P. E. Maslen, J. M. Papanikolas, J. Faeder, R. Parson, and S. V. ONeil, J. Chem. Phys. **101** (7), 5731 (1994).

[15] G. E. Busch, R. T. Mahoney, R. I. Morse, and K. R. Wilson, J. Chem. Phys. **51** (1), 449 (1969).

[16] M. T. Zanni, T. R. Taylor, B. J. Greenblatt, B. Soep, and D. M. Neumark, J. Chem. Phys. **107** (19), 7613 (1997).

[17] J. Faeder, Ph.D. Thesis, University of Colorado, 1998.

[18] J. Faeder, N. Delaney, P. E. Maslen, and R. Parson, Chem. Phys. **239** (1-3), 525 (1998).

[19] N. Delaney, J. Faeder, and R. Parson, J. Chem. Phys. **111**, 651 (1999).

[20] P. E. Maslen, J. Faeder, and R. Parson, Chem. Phys. Lett. **263** (1-2), 63 (1996).

[21] Y. Marcus, *Ion Solvation*. (Wiley, New Yord, 1985).

[22] R. Mabbs, K. Pichugin, E. Surber, and A. Sanov, J. Chem. Phys. **121**, 265 (2004).

[23] N. Delaney, Ph.D. Thesis, University of Colorado, 1999.

[24] R. Parson, J. Faeder, and N. Delaney, J. Phys. Chem. A **104**, 9653 (2000).

[25] P. C. Engelking, J. Chem. Phys. **87** (2), 936 (1987).

Chapter 4

Photoelectron Imaging Spectroscopy of Cu^- and $Cu^-(H_2O)_{1,2}$ Anions

4.1 Introduction

The photofragmentation branching ratio experiments described in Ch. 3 demonstrate the detailed nature of the solvation effects observed in $IBr^-(CO_2)_n$ clusters as a function of cluster size. However, these studies probe the state of the system upon detection some 10 μs after the dynamics are initiated. The time-resolved absorption recovery experiments shed a more light on the early time photodissociation dynamics, but the probing of the system is limited to the narrow window when the chromophore is recombined on the ground state as discussed in Ch. 1. The photoelectron imaging spectrometer was designed and installed to provide a method to measure the state of the system at any given time during the dynamics. The photodetachment of charged species in the clusters is not limited to a specific region of the potential energy surfaces and provides snapshots of the dynamics at any time after initiation by photoabsorption of the chromophore. The pulsed nature of the experiment allows the use of pulsed, tunable lasers to provide higher photon energies than those available with cw lasers for the study of higher energy electronic states.

The first photoelectron imaging studies are carried out on Cu^- and $Cu^-(H_2O)_n$ clusters for three reasons. The new imaging spectrometer initially needed to have its performance optimized. This includes the determination of electrode voltages for the best focusing of the images on the detector. An atomic system was desirable due to the narrow lineshapes for atoms. Also, the Cu^- photoelectron spectrum had

previously been measured[1] in this group and could be used as a benchmark for the spectra obtained from the new spectrometer. The second reason is that the Cu^- solute solvated by H_2O molecules provides a simple solvent system in which to test the applicability of the photoelectron imaging spectrometer to solvation studies in general. The Neumark group has previously shown the effect of increasing solvation on an atomic anion represented by the shift of spectral features to higher binding energies as the number of solvent molecules is increased as well as changes in the vibrational progressions of the solvent molecules as a result of perturbations by the charged solute.[2,3] Similar solvation affects should be present in the $Cu^-(H_2O)_n$ complexes. The final reason for the imaging study of $Cu^-(H_2O)_n$ complexes is to build on work carried out on $Cu^-(H_2O)_{1,2}$ which includes a low resolution photoelectron spectroscopy study,[4,5] rearrangement dynamics of the complexes following photodetachment,[6] and calculations on the complexes.[7,8]

4.2 Photoelectron Imaging of unsolvated Cu^-

The copper atomic anion has an electron configuration of $3d^{10}4s^2$ leading to a $^1S_0$ ground state. The energy level diagram of the anion ground state, as well as the three low-lying electronic states of the neutral, is shown in Fig 4.1. The electron affinity (EA) of Cu corresponding to the Cu $^2S_{1/2}$ $(3d^{10}4s^1) \leftarrow Cu^-$ $^1S_0$ $(3d^{10}4s^2)$ transition has been measured[9] as 1.23579(4) eV in agreement with the earlier measurement[1] of 1.235(5) eV. Higher energy photons with the tunable laser can be employed to detach d shell electrons leading two transitions at higher binding energies corresponding to Cu $^2D_{5/2}$ $(3d^9 4s^2) \leftarrow Cu^-$ $^1S_0$ $(3d^{10}4s^2)$ and Cu $^2D_{3/2}$ $(3d^9 4s^2)$

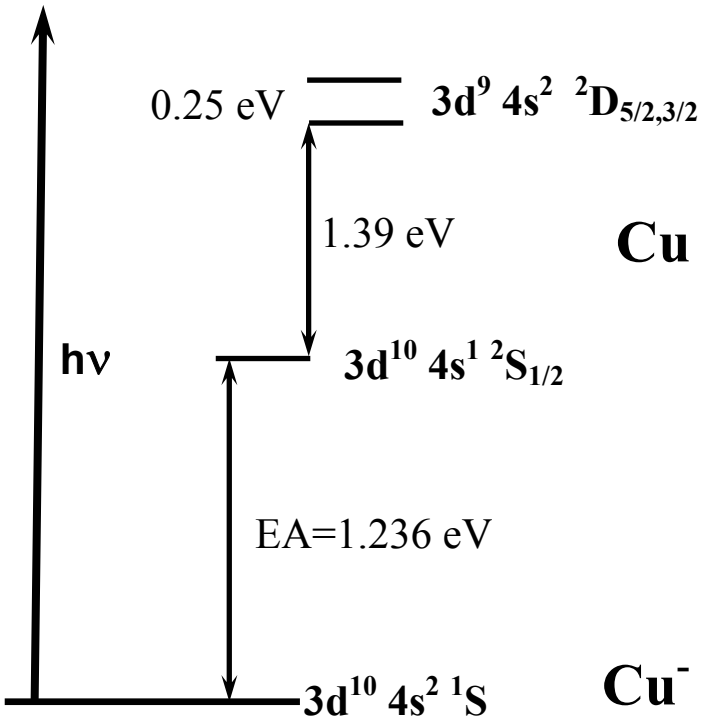

Figure 4.1: Energy level diagram for the ground state of Cu^- and the three low-lying states of Cu neutral.

← Cu^- $^1S_0$ ($3d^{10}4s^2$). The term energy of the $^2D_{5/2}$ neutral state is 1.3889 eV with the higher spin-orbit state $^2D_{3/2}$ 0.2533 eV greater in energy.[10]

The Cu^- bare anion is easily produced in the discharge source and the slightly more intense $^{63}Cu^-$ isotope is mass-selected and used for the bare anion photodetachment. The first step is to determine the electrode voltage ratio to provide the best focusing of the image. This ratio is the absolute value of the flight tube voltage divided by the extraction plate voltage. In this case, the Cu^- anion is detached using 964.7 nm (1.285 eV) photons producing photodetached electrons with a kinetic energy of around 50 meV. The electron kinetic energy (eKE) scales as velocity squared, so the best resolution occurs for slower electrons. The extraction voltage is set to –30 V to ensure that the images are completely on screen and the flight tube voltage is then varied and images acquired. The photoelectron spectra are extracted from the images and the $^2S_{1/2}$ peak is fit to a Gaussian line-shape and the full-width half-maximum of the fit determined. The flight tube voltage is varied until this FWHM is minimized, which is typically less than 5 meV in width for Cu^- at these low electron kinetic energies. The optimum ratio is found to be 4.48 meaning that if the extraction plate is at –10 V the flight tube must be set to +44.8 V to ensure the best focusing of the image.

The energy resolution, $\Delta E/E$, of the instrument is measured as the FWHM of a peak divided by the electron kinetic energy of the peak. These values are around 0.025 with the best $\Delta E/E$ value of 0.017 recorded for photodetachment at 532 nm, which is a fundamental wavelength from the Infinity with a narrower line-width than those for the OPO wavelengths. The image can now be magnified by changing by

the voltage on the extraction plate and thus the flight tube to keep the determined voltage ratio constant. Two raw images at extraction plate voltages of –5 V and –50 V are shown in Fig. 4.2 to demonstrate the effects of varying the extraction voltage and thus the magnification of the image. Both the raw and reconstructed images are shown in Fig. 4.2 as well to highlight the improvement in quality between the two. The center line noise in Fig. 4.2 b,c is an artifact from the reconstruction. It should be noted, however, that the energy resolution, $\Delta E/E$, remains approximately independent of the magnification. The magnification determines the calibration scale as electrons with the same kinetic energy are located at different pixels on the CCD camera depending on the extraction voltage used. The electron kinetic energy and thus the resolution are determined largely by the photon energy used. The spectra must be calibrated for each extraction voltage used in the experiments.

The photoelectron spectra extracted from the reconstructed images are presented in counts versus pixel. The pixel axis must be calibrated and converted to an electron kinetic energy scale which can then be converted to electron binding energy if desired. The pixel, which represents the velocity of the photoelectron, must first be squared due to the velocity squared dependence of the kinetic energy. The pixel squared value with the most counts is determined, which is assigned as the electron affinity in the case of Cu^- photodetachment. This pixel squared value is then assigned the eKE value of the electron affinity determined from previous photoelectron assignments. The calibration factor for this particular extraction voltage is given by the assigned eKE divided by the pixel location squared. This

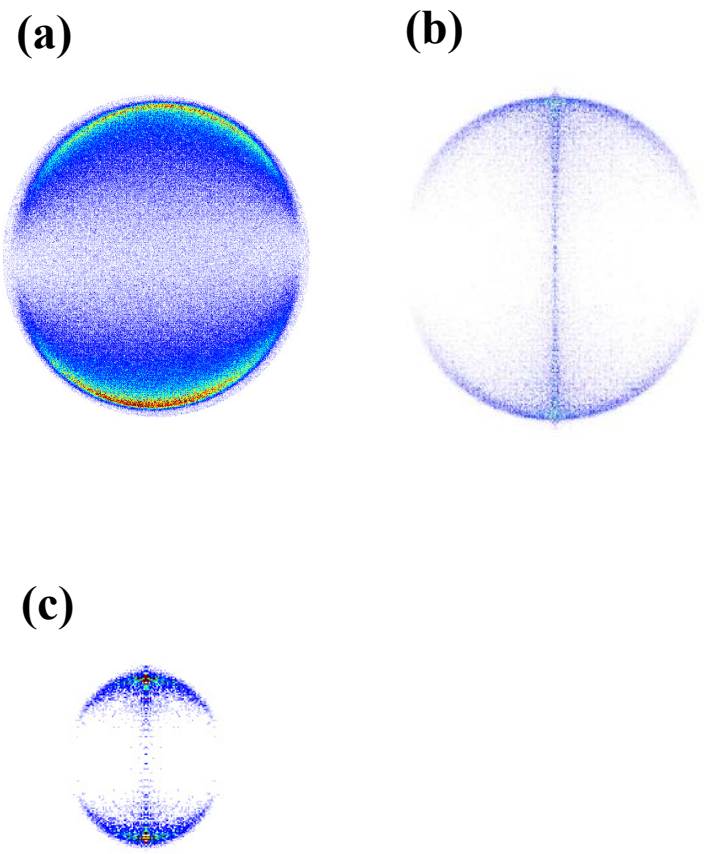

Figure 4.2: Photoelectron images of Cu^- taken at 964.7 nm (1.285 eV). Image (a) is the raw image taken an extraction plate voltage of –5 V and image (b) is the BASEX reconstruction. Image (c) is the raw image taken at an extraction plate voltage of –50 V demonstrating the magnification properties of images with the same eKE.

factor is then used to scale the rest of the pixel squared axis to eKE. This calibration factor is determined for various extraction voltages (but retaining the same voltage ratio for each) at 964.7 nm. The plot of calibration factor versus extraction voltage is shown in Fig. 4.3. The plot is nearly linear and a linear fit to the data is shown. This plot can then be used to determine the calibration factor for any extraction plate voltage used making recalibration of the spectrum unnecessary whenever the voltage is changed. The final data adjustment deals with the counts to be plotted as a function of eKE. A Jacobian correction must be made to account for the fact that the BASEX reconstruction program artificially produces more counts at large pixel radii where the integrated area is much larger than for the smaller pixel radii. This correction is simply the counts at a pixel divided by the pixel. This Jacobian correction is then normalized to the value at the most intense peak (typically the EA or VDE) and plotted versus the calibrated eKE to yield the final photoelectron energy spectrum.

The raw image and the reconstruction along with the photoelectron energy spectrum are shown in Fig. 4.4 for the 532 nm (2.33 eV) photodetachment of Cu^-. Both the electron binding (eBE) and the electron kinetic energies (eKE) are shown. The electron binding energy is simply the calibrated eKE subtracted from the photon energy, 2.33 eV in this case. The spectrum shows one intense peak at the EA of Cu of 1.236 eV and a labeled FWHM of 19 meV at an eKE of 1.095 eV and is assigned as the $^2S_{1/2}$ state of the neutral. This leads to a $\Delta E/E$ of 0.017. The value for β is 2.00(1) where the uncertainty is one standard deviation of the mean across the FWHM of the peak.

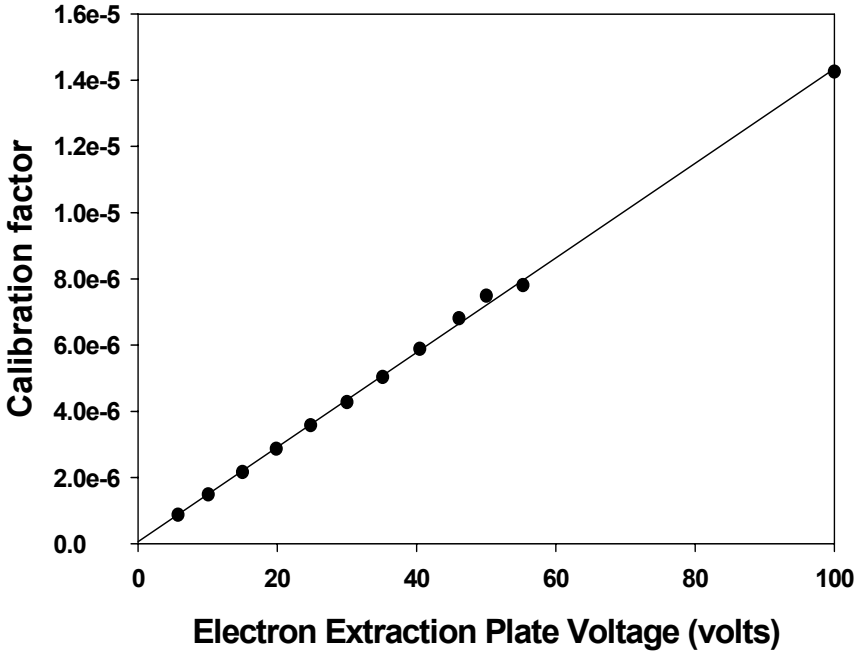

Figure 4.3: Energy scale calibration factor as a function of voltage placed on the extraction plate for Cu^- photodetachment at 964.7 nm. The extraction plate to flight tube voltage ratio is kept constant.

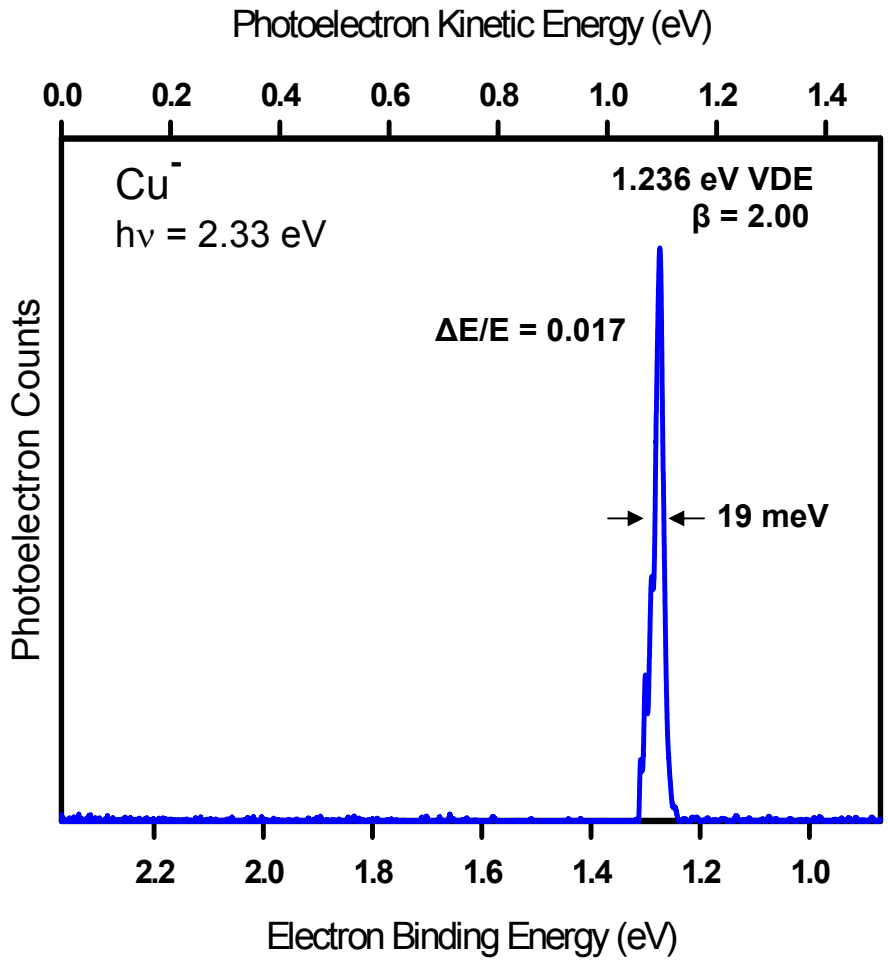

Figure 4.4: Photoelectron energy spectrum extracted from the BASEX reconstructed image of Cu^- photodetachment at 532 nm (2.33 eV). The peak is assigned as the $^2S_{1/2}$ state of neutral Cu.

The value of β represents the anisotropy of the photoelectron distribution for this ^{2}S peak and describes the nature of the orbital from which the photodetachment occurs. The angular distribution of photoelectrons within the dipole approximation[11] is given by the expression,

$$\frac{d\sigma}{d\Omega} = \frac{\sigma_{tot}}{4\pi}(1 + \beta P_2(\cos\Theta)), \tag{4.1}$$

where $P_2(\cos\Theta)$ is the second Legendre polynomial given by

$$P_2(\cos\Theta) = \frac{1}{2}(3\cos^2\Theta - 1). \tag{4.2}$$

The value of β is the asymmetry parameter and can range in value between –1 and 2. The symmetry character of the orbital from which photoelectrons originate is reflected in the angular distributions and is most easily demonstrated for atomic systems. The transition of an electron between electronic states must obey the $\Delta l = \pm 1$ orbital angular momentum selection rule. Photodetachment from an s orbital ($l = 0$) must impart one unit of angular momentum thus producing a p partial wave. A p partial wave has a $\cos^2\Theta$ distribution corresponding to a β value of +2. Detachment from a p orbital can lead to either s or d waves from the $\Delta l = \pm 1$ selection rule. Near threshold detachment leads to the isotropic s wave dominating and $\beta = 0$. Further from threshold, the d wave contribution increases leading to a mixing of the two and values closer to $\beta = -1$. The assignments become less clear for molecules due to the

mixing of atomic orbitals, but the complexes studied here can be approximated with the charge residing on the atomic copper with a weakly interacting solvent. The value of β for photodetachment of Cu^- at 532 nm was measured to be 2.00 corresponding to detachment from an s orbital producing a p partial wave.

The laser wavelength can be tuned to the blue to provide higher photon energies that now make the two ^2D states of the neutral Cu accessible. The photoelectron spectrum of Cu^- taken at 355 nm (3.49 eV) is shown in Fig. 4.5. The ^2S peak is still present, though slightly broader in width at 54 meV than the 532 nm spectrum due to the higher eKE of the photoelectrons associated with this peak at this wavelength. It still appears at the previously measured EA of 1.236 eV. The two accessible ^2D states appear at 1.39 eV higher eBE with the splitting between the two states reflecting the spin-orbit splitting of 250 meV. Both peaks have FWHMs of around 35 meV, narrower than the ^2S state reflecting the lower eKEs of the ^2D electrons. The ^2S state still retains $\beta = 2$ and the ^2D states have values of 0.07 and –0.11. These states correspond to detachment of d orbital electrons leading to p and f partial waves. This mixture of partial waves leads to near isotropic angular distributions and β values close to 0.

4.3 Photoelectron Imaging of $Cu^-(H_2O)_n$ complexes

The imaging photoelectron spectrometer was optimized and the spectra determined for the unsolvated Cu^- anion. These spectra will be used as a baseline to determine the effects of solvation of the Cu^- solute by H_2O solvent molecules. The Cu^- data also provide an energy calibration scale for all subsequent spectra of the

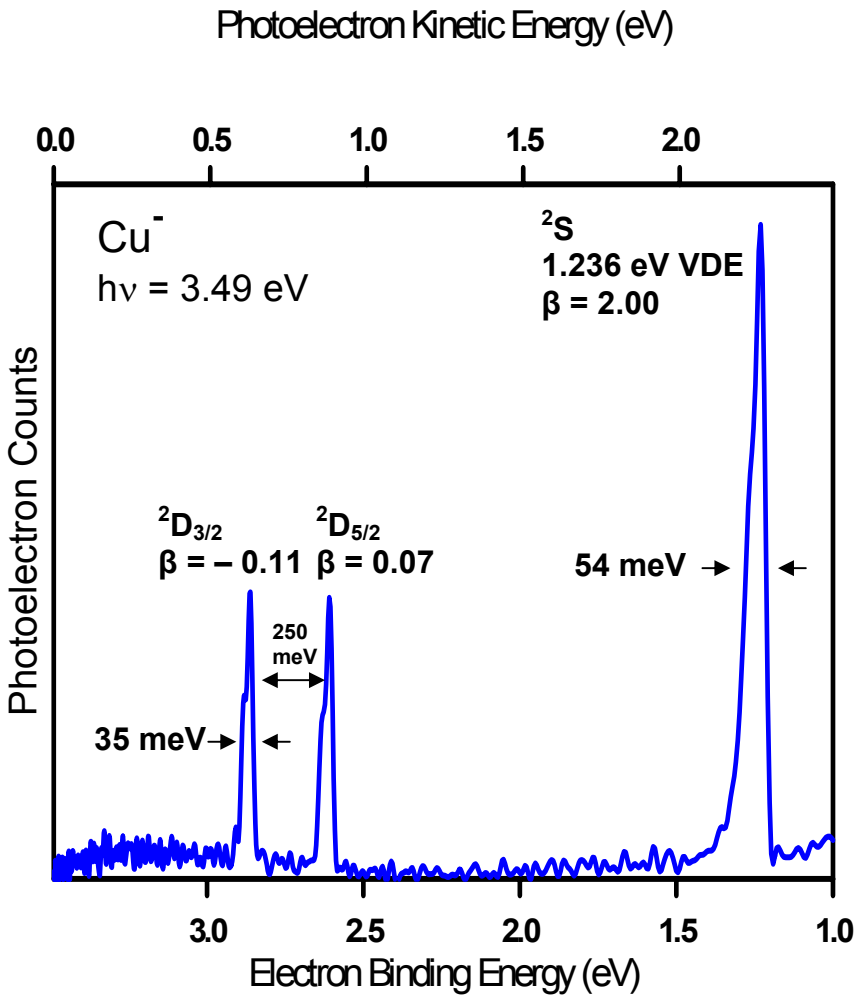

Figure 4.5: Photoelectron energy spectrum extracted from the BASEX reconstructed image of Cu^- photodetachment at 355 nm (3.49 eV). The main peak is assigned as the $^2S_{1/2}$ state of neutral Cu and now the two ^2D states are accessible. The term energy of the first ^2D is reported in the text. The 250 meV splitting between the two ^2D represents the spin-orbit splitting.

complexes. As mentioned above, the neutral states of the complexes are best characterized by the atomic state of the metal plus water molecules. The state notation used for the complexes is, for example, [Cu (^{2}S), H_2O] to represent the ground electronic state of the neutral Cu(H_2O) complex. In both $Cu^-(H_2O)$ and $Cu^-(H_2O)_2$, the ^{65}Cu isotope complex is mass-selected to avoid contamination from CuO^- and Cu^-(OH) peaks that are present in the mass spectra.

$Cu^-(H_2O)$

The photoelectron image and spectrum of $Cu^-(H_2O)$ are shown in Fig. 4.6 taken at 568.8 nm (2.184 eV). The electron kinetic energy scale is also shown to highlight the degree of energy resolution of the spectral features. The raw image is overlaid with the direction of the laser polarization with respect to the plane of the image shown as well. In this case, a lower energy photon is used for detachment to increase the resolution of the lower binding energy features. The dominant peak in the spectrum is assigned as the [Cu (^{2}S), H_2O] state of the neutral complex. The vertical detachment energy (VDE) is measured to be 1.637(4) eV where the 4 meV uncertainty is largely due to the error in the peak fitting of a Gaussian line-shape to the peak in the spectrum. The FWHM is found to be 40 meV with $\beta = 2.00(1)$. A smaller feature at slightly higher electron binding energy appears at 194 meV (1568(8) cm^{-1}) higher from the VDE with $\beta = 1.94(1)$ and is roughly 10% of the intensity of the main peak. This feature is just barely discernible in the raw image at a smaller radius from the main ring feature. The FWHM is roughly found to be 38

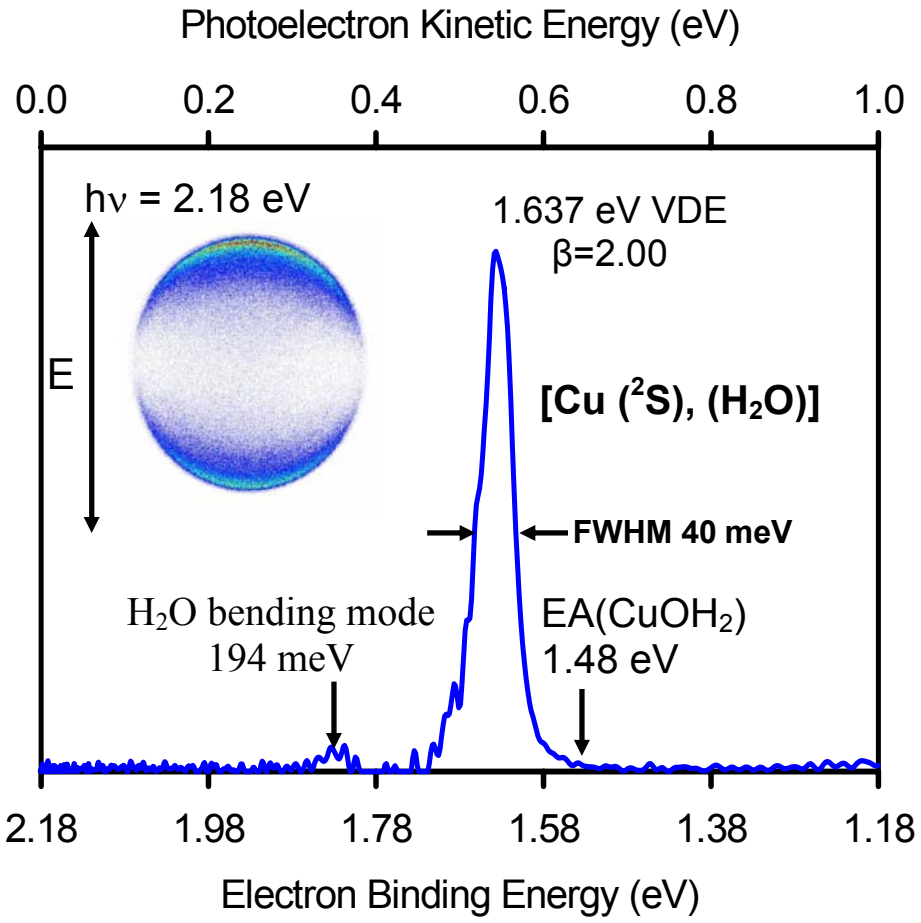

Figure 4.6: Photoelectron energy spectrum of $Cu^{-}(H_2O)$ taken at 568.8 nm (2.18 eV). This photon energy accesses only the ground ^2S state of the neutral complex. The bending mode of the H_2O solvent is labeled. The raw image is shown in the inset along with laser polarization direction.

meV, although the peak fit is somewhat uncertain due to the weak intensity of the feature.

The low intensity feature is assigned as the H_2O bending mode. The energy separation between this peak and the VDE of the [Cu (^{2}S), H_2O] state is close to the measured ν_2 bending mode frequency of isolated H_2O, 1595 cm^{-1}.[12] The studies of Cu atoms and H_2O molecules condensed in a cryogenic Ar matrix[13] provide a value of 1573 cm^{-1} that matches the photoelectron imaging value within the experimental uncertainty. The assignment of this feature to the H_2O bending mode is further confirmed by the measurement of the photoelectron spectrum of the deuterated complex, $Cu^-(D_2O)$. The photoelectron spectrum of $Cu^-(D_2O)$ is shown in Fig. 4.7 and is taken at 568.8 nm (2.18 eV). This spectrum exhibits a low intensity feature at 150 meV (1210(80) cm^{-1}) above the intense peak assigned as the [Cu (^{2}S), D_2O] transition. The energy difference between the two peaks is close to the D_2O ν_2 bending frequency[12] of 1178 cm^{-1} further validating the assignment of the small peak in the $Cu^-(H_2O)$ to the excitation of a local water bending mode in the complex. The VDE of the $Cu^-(D_2O)$ is 1.638(4) eV, the same as that in $Cu^-(H_2O)$, within the error bars.

The appearance of the photoelectron spectrum for $Cu^-(H_2O)$ with a single, narrow intense peak with what may be a small vibrational progression is expected for photodetachment of a nonbonding electron and production of a neutral molecule whose geometry is very close to that of the anion molecule. In this case, the most intense peak in the spectrum should provide the adiabatic electron affinity of the

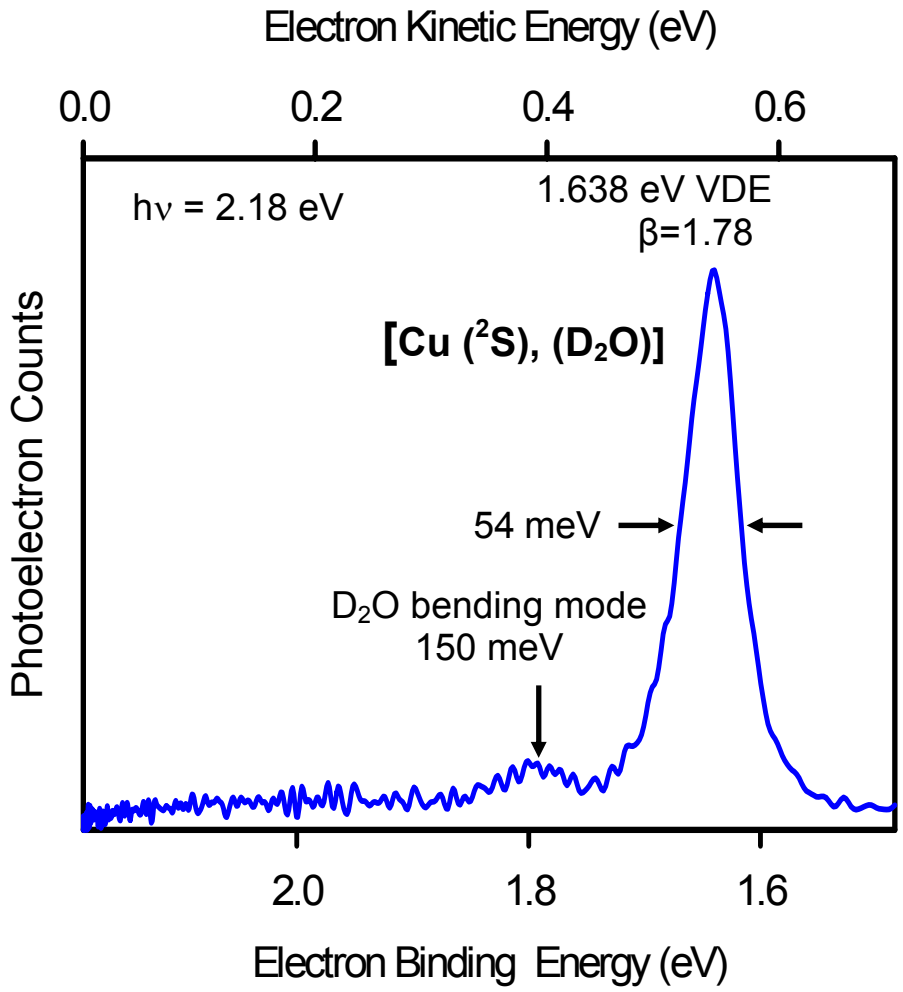

Figure 4.7: Photoelectron energy spectrum of $Cu^{-}(D_2O)$ taken at 568.8 nm (2.18 eV). This photon energy accesses only the ground ^2S state of the neutral complex. The bending mode of the D_2O solvent is labeled.

complex. However, there are no features found at the adiabatic electron affinity whose location is labeled in Fig. 4.6.

The Cu–O bond length in the $Cu^-(H_2O)$ complex is quite long at a calculated value[7] of 3.276 Å. Vertical photodetachment of the anion complex produces a neutral $Cu(H_2O)$ complex with a large Cu–O separation leading to very weak interactions between the Cu ^2S and the H_2O molecule. Calculations[7] have been carried out on the neutral complex and show that the potential energy difference between the neutral complex at the anion geometry and the separated Cu and H_2O is around 26 meV. This result is used in a simple thermodynamic cycle to determine the dissociation energy of the anion complex,

$$D_0[Cu^-–(H_2O)] = VDE[Cu^-(H_2O)] – EA[Cu] + \text{small correction} \qquad (4.3)$$

Where EA[Cu] is the electron affinity[9] of copper (1.236 eV), $VDE[Cu^-(H_2O)]$ is the measured vertical detachment energy found to be 1.637(4) eV, and the correction term is +20 meV, which is approximately 80% of the 26 meV calculated well depth. The value of $D_0[Cu^-–(H_2O)]$ is then found to be 0.42(2) eV which is in very good agreement with the calculated value of 0.44 eV.[7] The quantities in this calculation are shown in Fig. 4.8.

The large geometry difference between the anion and the neutral complexes is also demonstrated in that the most intense peak in the $Cu^-(H_2O)$ spectrum is the vertical detachment energy and not the adiabatic electron affinity. The electron affinity of $Cu(H_2O)$ is determined from a calculation[7] of the $Cu(H_2O)$ ground state

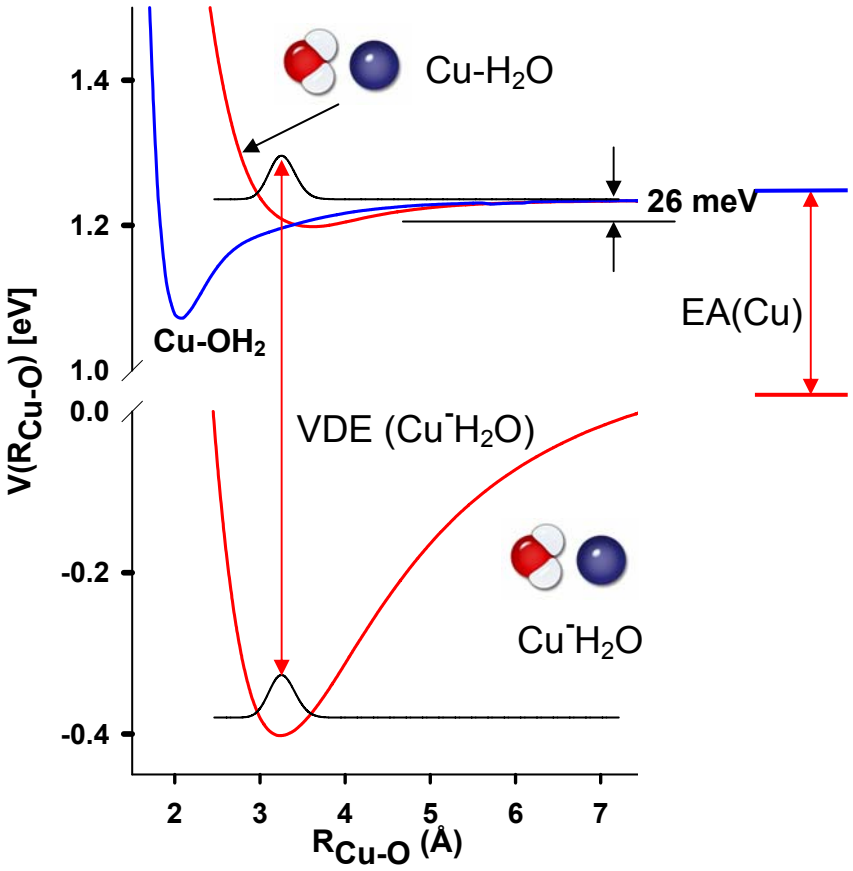

Figure 4.8: The potential energy surfaces for the $Cu^{-}(H_2O)$ anion and neutral complexes. The quantities mentioned in the text for the calculation of the anion complex dissociation energy are labeled. The structures for the anion ground state and the neutral complex after vertical detachment are shown.

surface from which the dissociation energy of the neutral complex, 0.16 eV, is found. The adiabatic electron affinity is given by this dissociation energy of the neutral complex subtracted from the VDE[$Cu^-(H_2O)$] represented by the intense peak in the $Cu^-(H_2O)$ spectrum. This gives an EA[$Cu(H_2O)$] of 1.48(3) eV. The error estimate is largely due to uncertainties in the neutral dissociation energy calculation. This spectrum has no detectable intensity where the electron affinity peak is expected to occur.

The photoelectron spectrum of $Cu^-(H_2O)$ with 355 nm (3.49 eV) is shown in Fig. 4.9. Photodetachment at this wavelength now accesses the two excited electronic states [Cu $^2D_{3/2,5/2}$, H_2O] of the neutral complex. The two peaks representing transitions to these two ^2D states are quite broad at roughly 150 meV FWHM compared to a FWHM of 40 meV for the ^2S state taken at low eKE. The greater width of these ^2D states is a result of the greater size of Cu ^2D compared to Cu ^2S. These peaks appear at electron binding energies of 3.050(2) and 3.313(2) eV, respectively, and show the expected spin-orbit splitting energy of 250 meV. The β values for these two peaks are 0.16(1) and 0.19(1), values that are quite different from $\beta = 2$ that is expected for detachment from an s orbital.

$Cu^-(H_2O)_2$

The photoelectron imaging spectroscopy of $Cu^-(H_2O)_2$ is carried out to study the effect of additional solvation on the Cu^- solute. This complex is very similar to $Cu^-(H_2O)$ in that the size difference between Cu^- $3d^{10}4s^2$ ^1S and Cu $3d^{10}4s^1$ ^2S allows for electron photodetachment to access portions of the neutral potential energy surface that have relatively weak interactions between the metal solute and solvent

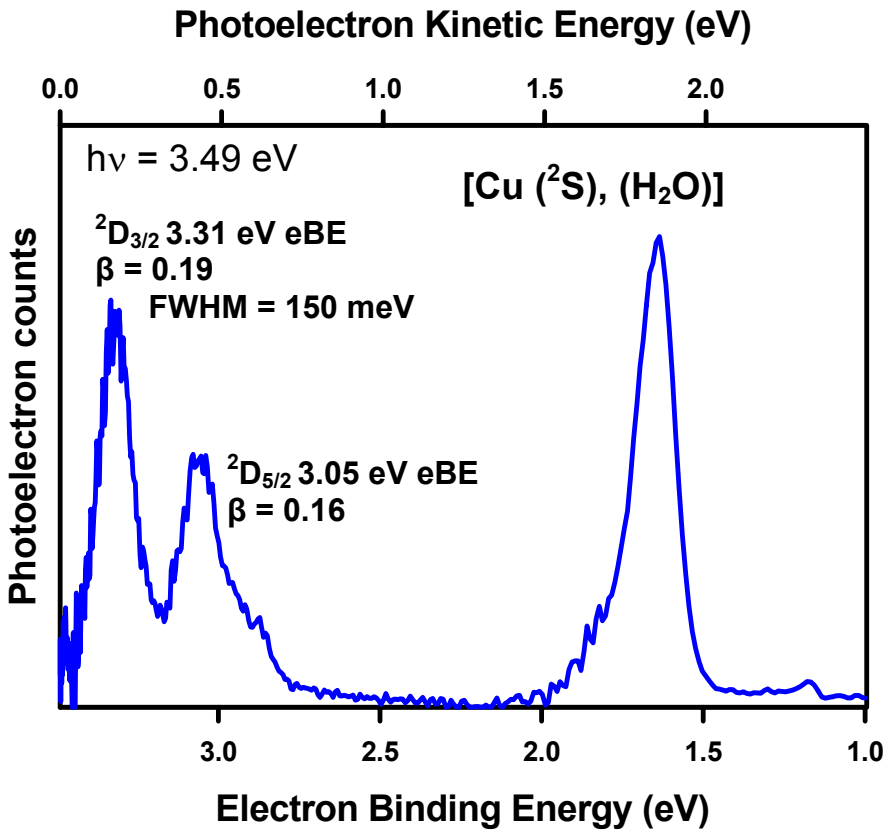

Figure 4.9: Photoelectron energy spectrum of $Cu^{-}(H_2O)$ at 355 nm (3.49 eV). The ^2D states are now accessible and are labeled accordingly. The values for the ^2S ground state do not appear as they are found in Fig. 4.6. The electron binding energies (eBE) at which the ^2D states appear are labeled along with the β values. The FWHM of each peak is roughly 140 meV.

water molecules. The orientation of the two water molecules is important in determining the observed peak widths in the spectra. The 40 meV peak width observed for $Cu^-(H_2O)$ would be expected to roughly double if the two H_2O solvent molecules were on opposite sides of the Cu^-. However, if the two H_2O solvent molecules are on the same side in a "quasi hydrogen-bonded dimer" configuration, photodetachment would lead to significant changes in the water-water interactions resulting in unresolved vibrational structure in the ground state peak with a width more than twice that of $Cu^-(H_2O)$.

The 521.2 nm (2.379 eV) photoelectron spectrum of $Cu^-(H_2O)_2$ is shown in Fig. 4.10 and only accesses the [Cu (^{2}S), 2 H_2O] state. The VDE is assigned as 2.003(8) eV with β = 1.86(2) consistent with detachment from an s orbital of Cu^-. The width of the peak is measured to be 97 meV, which is more than twice the width of the $Cu(H_2O)$ VDE peak. This suggests the two H_2O solvents are interacting significantly on one side of the solute and agrees with structure calculations of the complex.[14] There is also a partially resolved feature at 1540(80) cm^{-1} above the VDE, which is again assigned as the ν_2 bending mode of H_2O. A photoelectron spectrum is also taken at 313 nm (3.961 eV) to access the higher energy [Cu ($^2D_{3/2,\ 5/2}$), 2 H_2O] states of the complex and is shown in Fig. 4.11. The [Cu ($^2D_{5/2}$), 2 H_2O] state has a VDE of 3.50(7) eV with β = 0.4(1). The higher spin-orbit $^2D_{3/2}$ state has a VDE of 3.72(7) eV and β = 0.3(1). These transitions are even broader at roughly 200 meV than the ground state transition of $Cu(H_2O)_2$.

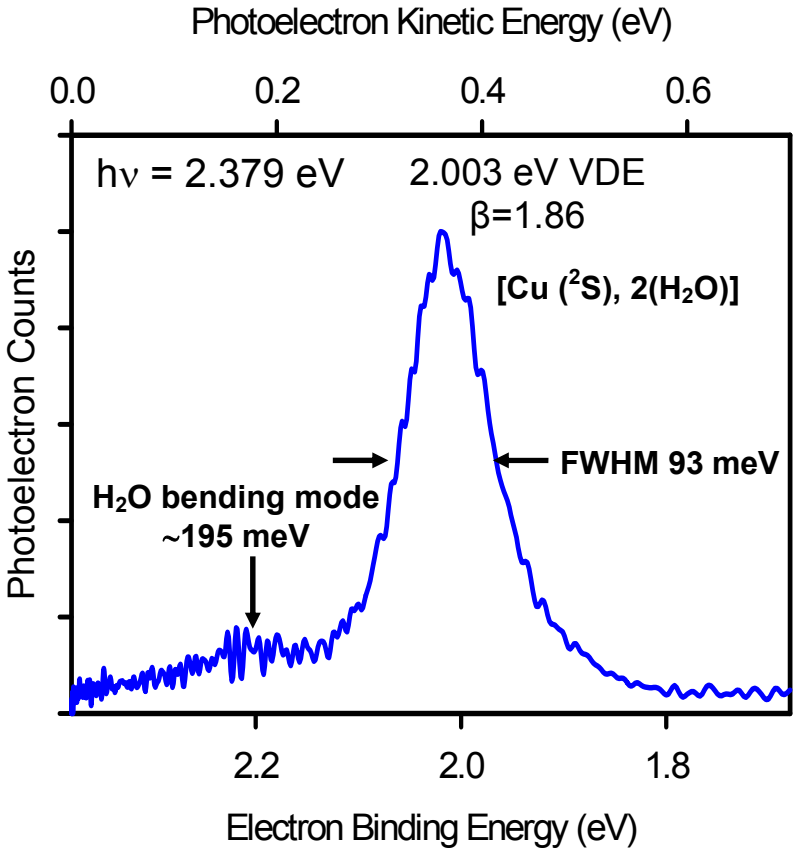

Figure 4.10: Photoelectron imaging spectrum of $Cu^{-}(H_2O)_2$ at 521.2 nm (2.379 eV). This wavelength only accesses the ground ^2S state of the complex. A very small feature at roughly 195 meV higher in binding energy is assigned as the H_2O bending mode.

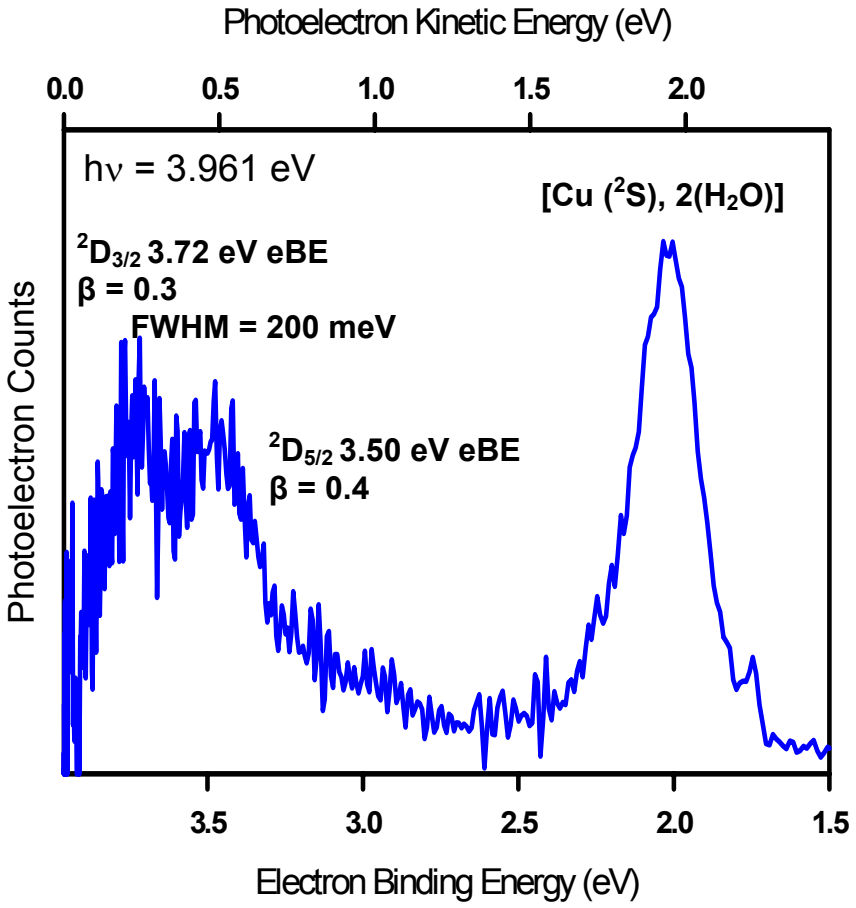

Figure 4.11: Photoelectron energy spectrum of $Cu^{-}(H_2O)_2$ at 313 nm (3.961 eV). The ^2D states are now accessible and are labeled accordingly. The values for the ^2S ground state do not appear as they are found in Fig. 4.10. The electron binding energies (eBE) at which the ^2D states appear are labeled along with the β values. The FWHM of each peak is roughly 200 meV.

4.4 Summary of increasing solvation on $Cu^-(H_2O)_n$ complexes

The performance of the new photoelectron imaging spectrometer was first characterized and optimized using the Cu^- atomic anion. The results on the bare Cu^- "solute" provide the peak widths and energy resolution, vertical detachment energy (in this case the electron affinity) and term energies of the $^2S_{1/2}$ ground state and the $^2D_{3/2,\ 5/2}$ excited states of the neutral Cu from which the effects of solvation by H_2O molecules can be determined. The subsequent spectra on the $Cu^-(H_2O)_{1,2}$ complexes demonstrate that the solvation is best characterized as the metal anion solute being perturbed by the H_2O adducts in these weakly bound complexes. A composite of the spectra for $Cu^-(H_2O)_{0,1,2}$ is shown in Fig. 4.12. The bare Cu^- was taken previously on a separate photoelectron spectrometer.[1] The broadening patterns can be understood in terms of the size relationship $R(Cu^-\ 3d^{10}4s^2) \cong R(Cu\ 3d^9 4s^2) > R(Cu\ 3d^{10}4s)$. Photodetachment of an electron from the diffuse, doubly occupied $4s^2$ orbital leaves the neutral Cu with a 4s electron in an orbital with a much smaller spatial extent which interacts less with the H_2O solvents at the anion geometry due to an increased bond length between the Cu and the H_2O molecules. This leads to less peak broadening than that observed upon photodetachment of a 3d electron. In this case, the diffuse, doubly occupied $4s^2$ orbital is still present which interacts more strongly with the H_2O solvents leading to broader peaks. The excess charge in the $Cu^-(H_2O)_{1,2}$ is predominantly localized on the Cu^- anion solute, however, there is sufficient charge delocalization onto the solvent and reduction of the H-O-H bond angle to excite the H_2O bending mode upon photodetachment. This bending mode appears as the small features to higher electron binding energies of the ^2S ground state peaks. The ground

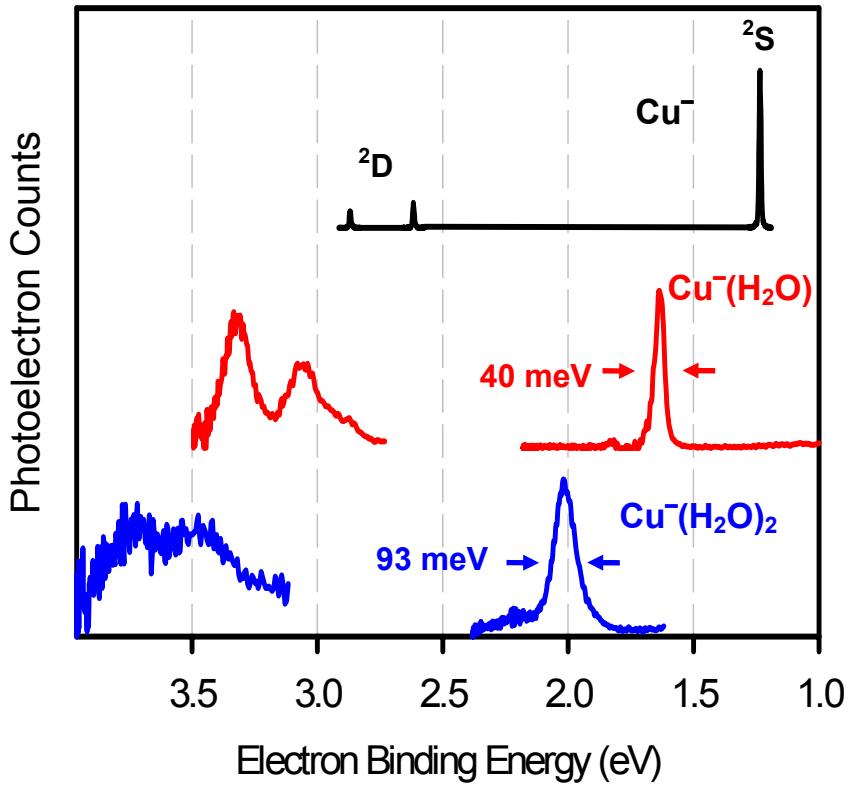

Figure 4.12: Composite photoelectron spectrum of the $Cu^-(H_2O)_n$ (n = 0,1,2) clusters. The individual spectra for $Cu^-(H_2O)_{1,2}$ can be found in previous figures. The Cu^- photoelectron spectrum is taken from Ho et al. referenced in the text. The progressive solvation retains the atomic level structure with broadening of peaks and shifts to higher electron binding energies.

state of the $Cu^-(H_2O)$ spectrum was shown to possess an intense, narrow peak with perhaps a short vibrational progression, which will be further investigated in future experiments. These traits are normally indicative of a neutral geometry that is very similar to the anion precursor geometry. However, the adiabatic electron affinity is absent from the spectrum and the intense peak is instead assigned as the vertical detachment energy. The absence of the adiabatic electron affinity is a result of the large size difference between Cu^- $3d^{10}4s^2$ and Cu $3d^{10}4s^1$ and the large geometry change between the anion and neutral complexes upon photodetachment. The vertical detachment energy is related to the dissociation energy of the anion complex which is calculated through a simple thermodynamic cycle.

Chapter 4 References

[1] J. Ho, K. M. Ervin, and W. C. Lineberger, J. Chem. Phys. **93**, 6987 (1990).

[2] D. W. Arnold, S. E. Bradforth, E. H. Kim, and D. M. Neumark, J. Chem. Phys. **97**, 9468 (1992).

[3] D. W. Arnold, S. E. Bradforth, E. H. Kim, and D. M. Neumark, J. Chem. Phys. **102**, 3510 (1995).

[4] F. Misaizu, K. Tsukamato, M. Sanekata, and K. Fuke, Laser Chemistry **15,** 195 (1995).

[5] F. Misaizu, K. Tsukamoto, M. Sanekata, and K. Fuke, Surf. Rev. Lett. **3**, 405 (1996).

[6] F. Muntean, M. S. Taylor, A. B. McCoy, and W. C. Lineberger, J. Chem. Phys. **121**, 5676 (2004).

[7] M. S. Taylor, F. Muntean, W. C. Lineberger, and A. B. McCoy, J. Chem. Phys. **121**, 5688 (2004).

[8] A. Antusek, M. Urban, and A. J. Sadlej, J. Chem. Phys. **119**, 7247 (2003).

[9] R. C. Bilodeau, M. Scheer, and H. K. Haugen, J. Phys. B **31**, 3885 (1998).

[10] J. Sugar and A. Musgrove, Journal of Physical Chemistry Reference Data **19**, 527 (1990).

[11] J. Cooper and R. N. Zare, J. Chem. Phys. **48**, 942 (1968).

[12] T. Shimanouchi, *Tables of Molecular Vibrational Frequencies Consolidated Volume I*. (National Bureau of Standards, Washington, DC, 1972).

[13] J. W. Kauffman, R. H. Hauge, and J. L. Margrave, J. Phys. Chem. **89**, 3541 (1985).

[14] M. S. Taylor, J. Barbera, C. P. Schulz, F. Muntean, A. B. McCoy, and W. C. Lineberger, J. Chem. Phys. **in press** (2004).

Chapter 5

Photodissociation Dynamics of Trihalide Anions

5.1 Introduction

Trihalide anions offer precursors for the study of dihalide anion wavepacket dynamics. The selective photodissociation of these trihalide anions produces a vibrationally excited wavepacket in the dihalide anion products. The triiodide anion, I_3^-, has been the subject of numerous of these wavepacket dynamics studies in both solution[1-10] and in the gas phase.[11,12] However, the triiodide anion is symmetric with both bonds being identical making control of the dissociation process and selective bond breaking impossible. It is also difficult to determine on which atom the charge resides after dissociation and the exact product formation mechanism.

These problems are reduced in the case of a non-symmetric trihalide anion. The reaction pathways and charge location are unambiguously identifiable and the dynamics are richer due to the appearance of additional reaction pathways. The subjects of these mixed trihalide studies are $BrICl^-$ and IBr_2^-, which were easily synthesized in the pulsed valve source. Characterization of these species is first carried out by theoretical calculations to determine ground state structures and energies along with vibrational frequencies. One-photon photodissociation experiments are carried out to determine the products formed and then comparisons are made with the expected photodissociation products predicted from the calculations. The vibrational wavepacket dynamics of the diatomic anion formed from the photodissociation of the triatomic anion is studied by time-resolved pump-

probe experiments. The triatomic anions are photodissociated with a UV pump photon to produce a vibrationally excited diatomic anion. The vibrational wavepacket dynamics of the diatomic anion product is monitored by the absorption of an IR probe photon. The time-dependent signal observed when the delay between the pump and the probe pulses is varied results from the motion of the wavepacket. These experimental results are compared to wavepacket dynamics simulations performed near dissociation threshold of the diatomic anion to determine the relationship between the proximity of this threshold to the level where the wavepacket is initially formed on the subsequent dynamics of the wavepacket.

5.2 Synthesis and Identification of $BrICl^-$ and IBr_2^-

The apparatus on which these experiments are carried out has been described in detail in Ch. 2. The ions are formed and analyzed in the same manner, but the method for preparation was not discussed previously. Separate mixtures are used to preferentially form each of the two trihalide anion species studied. For the formation of $BrICl^-$, the gas sample is prepared by passing a mixture of 5% CH_3Br seeded in Ar over a sample of solid ICl at room temperature. The resulting mixture is expanded through the supersonic nozzle at a backing pressure of 3 atm. The neutral expansion is crossed perpendicularly by the 1 keV beam of electrons. To preferentially form the IBr_2^-, the ICl sample is replaced by IBr which is heated to about 40ºC to increase the vapor pressure. The same 5% mixture of CH_3Br in Ar is used for the backing gas. Though not the subject of experiments presented here, I_2Br^- was also preferentially

formed in an analogous manner as for $BrICl^-$ and IBr_2^- by using I_2 as the solid sample with the same backing gas mixture.

The mass spectra of these two mixtures are shown in Fig. 5.1. The two trihalide anions of interest are the dominant peaks in each spectrum. The exact mechanism for the formation of these ions is not known, but it likely involves the attachment of slow, secondary electrons to complex neutral clusters as solvent evaporation and collisions remove the excess energy.[13] An alternative mechanism for the formation is a solvent-assisted association of ICl or IBr with Br^- generated by dissociative electron attachment to CH_3Br or IBr itself (i.e. via a diabatic electron capture mechanism).[13-17]

The peaks in the spectra were easily assigned due to the various isotope ratios of the constituent Br and Cl atoms in the ions of interest. The triplet structures of the $BrICl^-$ and IBr_2^- peaks in Fig. 5.1(a) (masses 241, 243, 245, and 285, 287, 289, respectively) reflect the existence of the isotopes of $^{79,81}Br$ and $^{35,37}Cl$ (while ^{127}I is the only major natural isotope of iodine). The natural abundance ratios of $^{79}Br : {}^{81}Br \approx 1:1$ and $^{35}Cl : {}^{37}Cl \approx 3:1$ dictate the following intensity patterns for the $BrICl^-$ and IBr_2^- peaks: $^{79}BrI^{35}Cl^- : (^{79}BrI^{37}Cl^- + {}^{81}BrI^{35}Cl^-) : {}^{81}BrI^{37}Cl^- \approx 3:4:1$ and $^{79}BrI^{79}Br^- : {}^{79}BrI^{81}Br^- : {}^{81}BrI^{81}Br^- \approx 1:2:1$. The isotope patterns for these and other ions are helpful in assigning the peaks in the mass spectra. For example, the group of four peaks (m = 379, 381, 383, and 385) in Fig. 5.1(b) labeled as $IBr_2^-\cdot CH_3Br$ reveals deviation from the statistically expected isotope ratio of 1:3:3:1. The excessive intensity of the m = 381 peak is most likely due to a contribution from I_3^-.

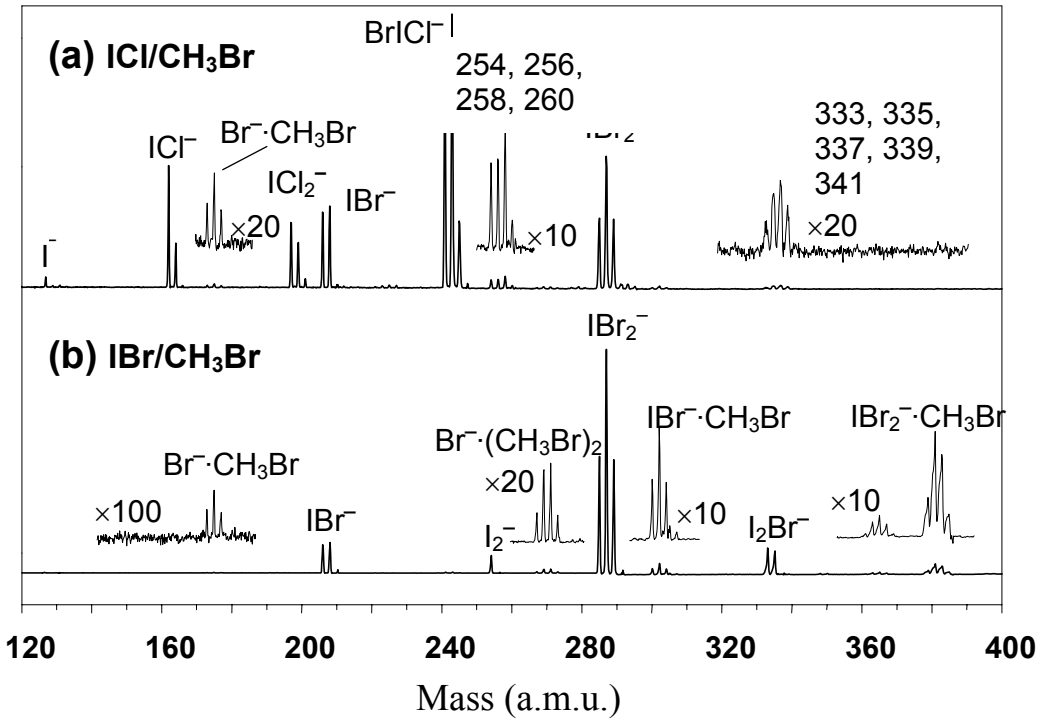

Figure 5.1: Mass spectra of precursor anions formed by co-expanding (a) ICl and CH_3Br seeded in Ar carrier gas, and (b) IBr and CH_3Br in Ar.

5.3 Calculated Structures and Dissociation Energetics

The zero-order energetics and structures of the $BrICl^-$ and IBr_2^- anions are investigated using density functional theory (DFT). The calculations are carried out with Gaussian 98[18] at the level of Barone and Adamo's Becke-style one-parameter exchange functional *m*PW1PW.[19] For open-shell and closed-shell systems, the spin-unrestricted and spin-restricted methods are used, respectively. For iodine, the relativistic effective core potential of Hay and Wadt,[20] combined with a double-zeta valence basis set (LanL2DZ) is used. This basis is augmented with uncontracted diffuse *s* and *p* functions (exponents 0.0569 and 0.0330, respectively) and *d* and *f* polarization functions (exponents 0.292 and 0.441, respectively).[21] For bromine and chlorine, the 6-311+G(d) all-electron basis sets are used. For all species larger than an atom, the energies are calculated after full geometry optimizations.

The calculated energetics for the various possible structures of $BrICl^-$ and IBr_2^-, along with the energies corresponding to the various dissociation pathways, is shown in Fig. 5.2. As a comparison, the same energetics is also shown for I_3^- at the same level of theory. Spin-orbit coupling was not accounted for in these calculations and the zero-point vibrational energy corrections were not included. As seen in Fig. 5.2, the expected linear isomer $BrICl^-$ is the most stable form of $BrICl^-$.

For all of the trihalide anions, the ground state anion geometry is linear with most of the charge localized on the two end atoms. The $BrICl^-$ isomer is stabilized relative to the two other forms that have the I atom on an end position due to the greater electronegativity of Br and Cl compared to I. The larger I atom in the middle position also serves to screen the two partially charged Cl and Br atoms further,

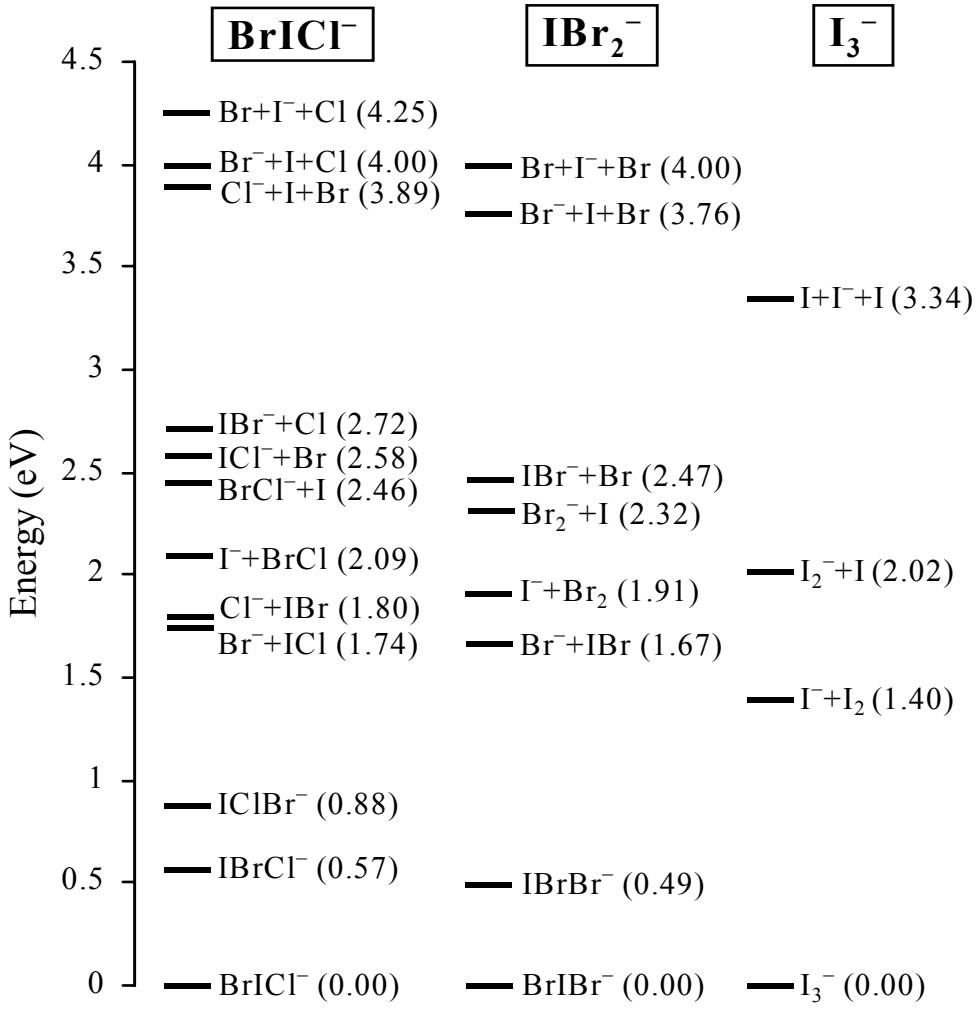

Figure 5.2: Energetics of the $BrICl^-$, IBr_2^-, and I_3^- anions, calculated using the *m*PW1PW density functional method, as described in the text. Numbers in parentheses are energies in electron volts relative to the most stable isomer of the corresponding trihalide anion

stablilizing the lowest energy isomer. The next lowest energy isomer, $IBrCl^-$, is calculated to be 0.57 eV higher and the least stable form, with the most electronegative Cl in the middle position, is 0.88 eV above the most stable $BrICl^-$ isomer. Similarly, the most stable form of IBr_2^- is the form containing the less electronegative I in the middle position with the two Br atoms occupying the end positions. The isomer $BrBrI^-$ is 0.49 eV higher in energy.

The energetics analysis does not include spin-orbit effects that play an important role in the spectroscopy and dynamics. The spin-orbit splittings for each atom lead to a multiplicity in all of the dissociation channels involving open-shell fragments in Fig. 5.2. Also, the DFT calculations overestimate the bond dissociation energies of the open-shell species due in part to the omission of spin-orbit coupling. For instance, Fig. 5.2 shows the dissociation energy of I_2^- as being 1.32 eV. This value was measured experimentally to be 1.01 eV.[22,23] The accuracy is better in closed-shell species. The bond strength of I_3^- is calculated to be 1.40 eV for dissociation to $I_2 + I^-$ compared to the experimental value of 1.31 ± 0.06 eV.[24] The calculations, though not completely accurate in all cases, do provide a helpful guide for interpreting the experimental data.

5.4 Photodissociation of $BrICl^-$

The photodissociation experiments are carried out on the mass selected $^{79}BrI^{35}Cl^-$ (m = 241) anion, corresponding to the first isotope peak in the $BrICl^-$ triplet in Fig. 5.1(a). The photodissociation of this mass selected anion was carried out at two UV wavelengths. The photofragmentation mass spectra are shown in Fig.

5.3 for photodissociation at 350 and 392 nm, respectively. For all wavelengths studied (350–410 nm), the IBr^- and ICl^- photodissociation products account for >95% of the one-photon photofragments and the $BrCl^-$ (m = 114) photoproduct is not produced. These products indicate that only the $BrICl^-$ isomer is formed in the ion source. This is in agreement with calculations that found the $BrICl^-$ isomer to be lowest in energy.

At these dissociation wavelengths, IBr^- is the dominant photoproduct with the yield decreasing slightly with increasing wavelength from 0.8 at λ = 405 nm to <0.7 at λ = 350 nm. The other prominent product is ICl^-, which increases in yield with increasing photon energy from about 0.2 at λ = 405 nm to 0.3 at λ = 350 nm. The atomic anion photoproducts, Cl^-, Br^-, and I^-, are present at the shorter wavelength (350 nm). However, these atomic products account for about 5% of the total photoproduct yield and completely disappear at the longer wavelength.

The time-resolved experiments are now carried out based on the one-photon results above. The diatomic photoproducts IBr^- and ICl^- are probed using the fundamental wavelengths (780–820 nm) to perform a second photodissociation step that is delayed in time with respect to the photodissociation of the trihalide anion. The photodissociation cross sections for IBr^- and ICl^- in this wavelength range have been characterized in a preceding chapter for IBr^- and previously for ICl^-.[25,26] For both dihalide products, absorption at these wavelengths produces I^- as the dominant product.

The pump-probe experiment consists of photodissociation of mass-selected $BrICl^-$ using second harmonic wavelengths (around 400 nm) of the fundamental

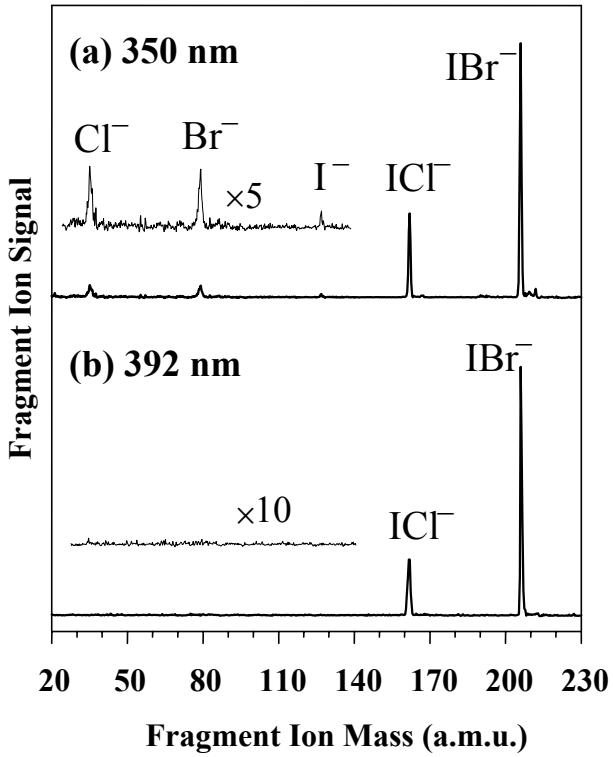

Figure 5.3: Photofragment ion mass spectrum obtained in the photodissociation of $BrICl^-$ (the $^{79}BrI^{35}Cl^-$ isotope) at (a) 350 nm and (b) 392 nm.

output of the femtosecond laser system. These wavelengths are used due to the improved performance of the system near 800 nm. The initial photodissociation produces the IBr^- and ICl^- photoproducts shown in Fig. 5.3(b). These diatomic fragments are then photodissociated with the fundamental IR (~800 nm) femtosecond pulse to produce I^- photoproducts that are detected as a function of delay between the pump (UV) and probe (IR) pulses. The time-resolved data for this process are shown in Fig. 5.4 representing two different pump-probe schemes with the wavelengths shown. Both the IBr^- and ICl^- photoproducts are produced in highly excited vibrational states. These excited states have absorptions that are red shifted from the maximum absorption of vibrationally relaxed IBr^- and ICl^-. The contributions from each of the dihalide anions to the two-photon I^- signal are not resolved, but it is assumed that most of the signal originates from IBr^- due to the relative product ratios from $BrICl^-$ dissociation and the relative absorption cross sections between ICl^- and IBr^- mentioned in a preceding chapter.

The first noticeable feature of the signals is the sharp initial peak at very short pump-probe delays and its rise time is determined by the time resolution of the experiment. This feature can partially be due to excited state absorption of $BrICl^-$ before any dissociation of the trihalide has taken place. This excited state correlates to IBr^- + Cl and/or ICl^- + Br channels if direct dissociation is occurring. The peak could then be attributed to probe absorption of IBr^- (ICl^-) being perturbed at early times by the neutral Cl (Br) fragments that have not yet left the vicinity of the excited photoproduct anion. The second feature is the oscillatory structure following the initial sharp peak. The time-dependent signal is superimposed with sine waves with

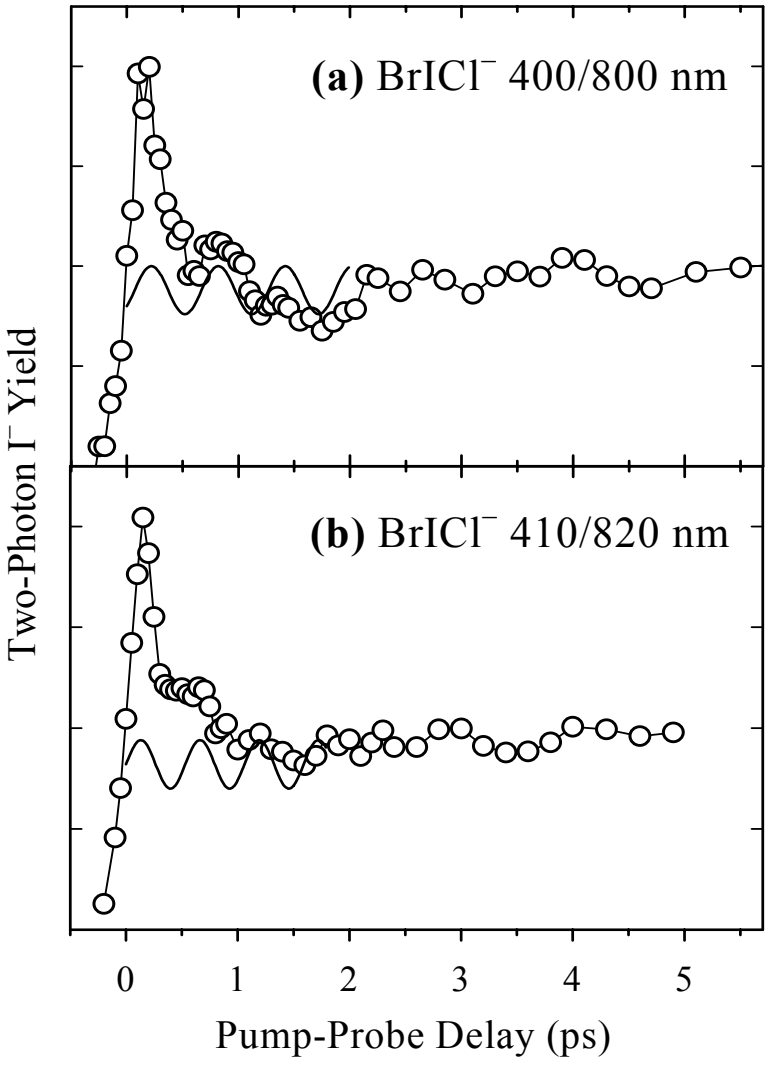

Figure 5.4: Delay-dependent pump-probe signals in the photo-dissociation of $BrICl^-$ as described in the text with 400 nm pump/800 nm probe in (a) and 410 nm pump/820 nm probe in (b). The superimposed sine waves highlight the oscillations and have periods of 600 fs in (a) and 530 fs in (b).

periods of 600 fs in Fig. 5.4(a) and 530 fs in Fig. 5.4(b). These oscillations are attributed to the newly formed IBr^- vibrational wavepacket and are discussed below.

5.5 Photodissociation of IBr_2^-

The photodissociation experiments on IBr_2^- were carried out on the $^{79}BrI^{81}Br^-$ (m = 287) isotope that corresponds to the most intense peak in the triplet in Fig. 5.1(b). The one-photon photodissociation products for photodissociation at 402 nm are shown in Fig. 5.5. The IBr^- fragments account for >95% of the total products, similar to $BrICl^-$. The photoproduct Br_2^- is not seen confirming the suspected identity of the lowest energy isomer predicted by the calculations. A small amount of dissociation leads to the atomic anion products Br^- and I^-. These atomic products do not disappear at lower photon energies as in the case of $BrICl^-$ photodissociation. The product mass spectrum shown for 402 nm photodissociation is representative of the product mass spectra over the entire wavelength range studied.

The time-resolved experiments for IBr_2^- are carried out in an analogous manner to $BrICl^-$. The pump photon produces vibrationally excited IBr^- that is then probed using the fundamental output wavelengths (~800 nm) by monitoring the pump-probe delay-dependent I^- two-photon product. The I^- product necessarily originates from IBr^- unlike $BrICl^-$ pump dissociation that yields both IBr^- and ICl^- photoproducts. However, the trihalide used in the experiments consists of both ^{79}Br and ^{81}Br isotopes. The observed two-photon I^- signal then arises from photodissociation of both $I^{79}Br^-$ and $I^{81}Br^-$ isotopes. The vibrational frequencies of the two isotopes differ by only 0.77% making the short term dynamics (<10ps)

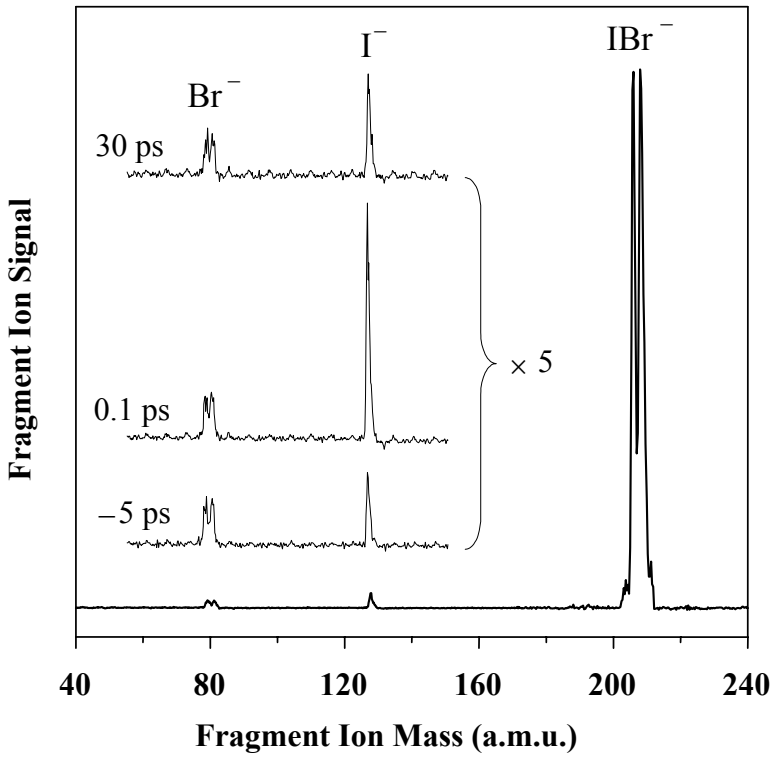

Figure 5.5: Photofragment ion mass spectrum of the photodissociation of IBr_2^- (the $^{79}BrI^{81}Br^-$ isotope) at 402 nm. The superimposed lines indicate the mass spectra with 402 nm pump/804 nm probe at the indicated delay times between the two.

unaffected by the superposition of the two frequencies. The mismatch of the frequencies becomes important on the tens of picoseconds timescale.[27]

The two-photon I^- signal is superimposed on the one-photon I^- signal from IBr_2^- dissociation by the pump beam only. The superimposed lines in Fig. 5.5 show portions of the photofragment mass spectra obtained from the pump (402 nm) and probe (804 nm) measurements at the indicated delays between the two. The bottom spectrum, recorded with the probe pulse arriving 5 ps before the pump, is similar to the pump-only mass spectrum, because the probe pulse is not absorbed by IBr_2^-. The middle trace, obtained at a 0.1 ps delay, shows an increase in the I^- intensity resulting from the two-photon formation of this fragment. The Br^- product intensity remains unaffected, because I^- is exclusively produced in IBr^- dissociation in the near-IR. At longer delays, the intensity of the I^- peak reduces again, but stays above the one-photon background level.

The delay dependent results are shown in Fig. 5.6 for three different wavelength combinations of pump and probe pulses. These time-resolved signals include background subtraction of the one-photon I^- signal that is present at all time delays. Qualitatively, the overall pattern of the data is similar to that of $BrICl^-$. However, the intensity of the initial peak compared to the long time signal is much greater in IBr_2^-. This ratio drops significantly with increasing pump and probe wavelengths. This could be due to either a decrease in excited state absorption in IBr_2^- or to an increase in probe absorption by vibrationally excited IBr^-.

Periodic oscillations in the I^- signal are present, as they are in the $BrICl^-$ data, and are attributed to IBr^- vibrational wavepacket motion. The oscillations are

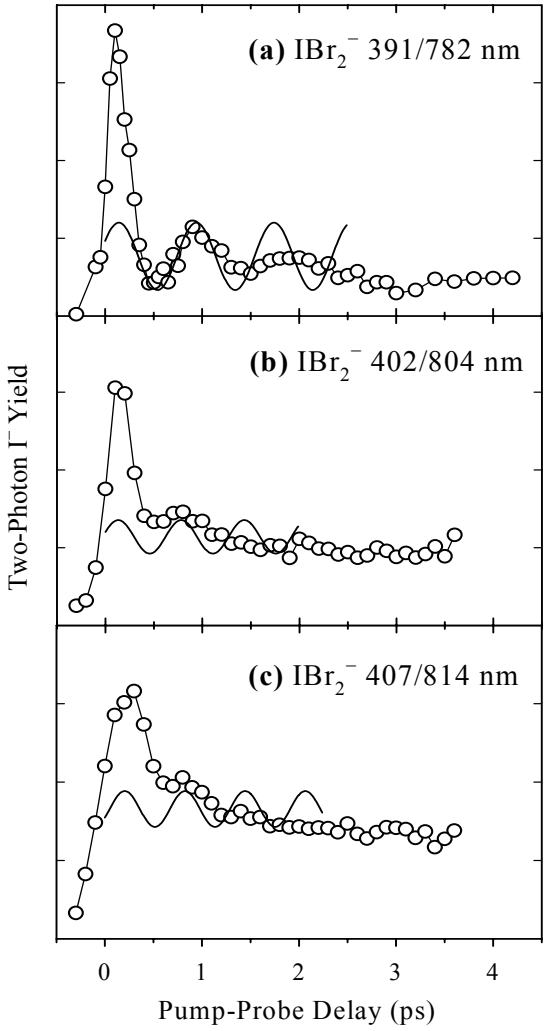

Figure 5.6: Delay-dependent pump-probe signals in the photo-dissociation of IBr_2^- as described in the text with 391 nm pump/ 782 nm probe in (a), 402 nm pump/804 nm probe in (b), and 407 nm pump/814 probe in (c). The superimposed sine waves highlight the oscillations and have periods of 800 fs in (a), 650 fs in (b), and 620 fs in (c).

highlighted with superimposed sine waves on the experimental curves. The sine waves have varying periods to best fit the experimental data. The trend in these three data sets is that decreasing pump and probe photon energies correspond to decreasing oscillation periods. As can be seen from Fig. 5.6, 391 nm pump/782 nm probe has an oscillation period of roughly 800 fs, 402/804 nm corresponds to 650 fs, and 407/814 nm with 620 fs. This trend is the result of exciting and probing progressively lower vibrational levels in the IBr^- photoproduct.

The IBr_2^- system presents an attractive subject for the study of wavepacket dynamics. It possess only one distinct intermediate fragment from which to probe the dynamics, unlike $BrICl^-$ where the observed time dependent I^- signal can originate from both ICl^- and IBr^- making the results less straightforward to interpret. As mentioned above, the presence of two isotopomers in the IBr^- one photon product can affect the wavepacket dynamics at longer pump-probe delays. The $I^{79}Br_2^-$ species is used when looking for long time recurrences in the wavepacket dynamics to ensure that only one vibrational frequency was present in the dihalide photoproduct. However, no recurrences in the vibrational wavepackets are observed around 18 and 29 ps where they are predicted to occur based on wavepacket simulations discussed below. In addition to insufficient time resolution that may smear out the weak revival signal seen at short delays, there may be a smearing of the revivals themselves due to the proximity of the wavepackets to the dissociation limit of the dihalide anion at longer pump-probe delays, which is described in detail below.

The photodissociation of I_2Br^- was briefly studied at 392 nm. This produced the dominant diatomic anion products of I_2^- and IBr^- with trace amounts of atomic anion products. The I_2^- photoproduct was five or six times as large as the IBr^- product. The appearance of I_2^- as a photodissociation product implies a structure with an I atom residing in the center position of the trihalide. The structure energetics was not calculated, however this experimentally determined structure follows from the results for $BrICl^-$ and IBr_2^- in which the more electronegative atom resides on an end position. The I_2Br^- trihalide anion provides an interesting precursor for studying the I_2^- wavepacket dynamics which have been carried out starting from I_3^- precursor.[11,12] Photodissociation of I_2Br^- places the I_2^- wavepacket closer to the dissociation threshold of I_2^- than photodissociation of I_3^-. The effects of the proximity of the dissociation threshold to the wavepacket dynamics in I_2^- can now be studied by simply tuning the precursor trihalide anion on which experiments are carried out.

5.6 Vibrational Dynamics of IBr^- Photofragments

The photodissociation of a trihalide anion to a diatomic anion and a neutral atom takes an excess anti-bonding electron delocalized across two bonds in the parent trihalide anion and localizes it onto one bond in the product diatomic anion. Both of the bonds in IBr_2^- and I_3^- have a bond order of ~3/4, while the bond order in the two diatomic fragment anions IBr^- and I_2^- is reduced to only 1/2. Therefore, the I-Br and I-I bonds are initially compressed in the trihalides relative to the relaxed diatomic anion products. The dihalide fragments are formed in vibrationally excited states at a short bond length. This is also true for both photofragment dihalides arising from the

dissociation of $BrICl^-$ and I_2Br^-.

The equilibrium geometries of the trihalide anions are shown along with the corresponding photofragment geometries in Fig. 5.7. These geometries are calculated with the DFT method described above. The values in parentheses indicate the bond elongation in angstroms upon photodissociation of each of the trihalides. The fragments IBr^- and ICl^- from photodissociation of $BrICl^-$ and IBr_2^- show a greater bond elongation than in the I_2^- fragment from I_3^- photodissociation. It is expected that the IBr^- and ICl^- products are formed with higher vibrational excitation than the I_2^- fragment formed from I_3^-.

The observed oscillations in the I^- signal are attributed to the motion of this newly created wavepacket on the IBr^- potential surface. The fragment formed is a coherent superposition of vibrational levels due to the duration of the pump pulse (~180 fs) being less than that of the fragment vibrational period. The diatomic fragment is able to absorb the probe photon when the initially compact wave packet passes through an absorption window most likely localized on the outer wall of the IBr^- potential. As the wavepacket makes several round-trips across the well, the anharmonicity of the potential causes the wavepacket to dephase and the absorption signal then disappears. In the case of $BrICl^-$, there is also a contribution from ICl^- as a wavepacket is also formed on the corresponding ICl^- potential and provides a time-dependent signal contribution to the overall observed I^- signal. However, these contributions from ICl^- are neglected due to the smaller amount of it formed from $BrICl^-$ dissociation (~4:1 for IBr^-:ICl^-) and the much smaller absorption cross section for ICl^- in the near-IR. Both of these factors lead to a negligible contribution to the I^-

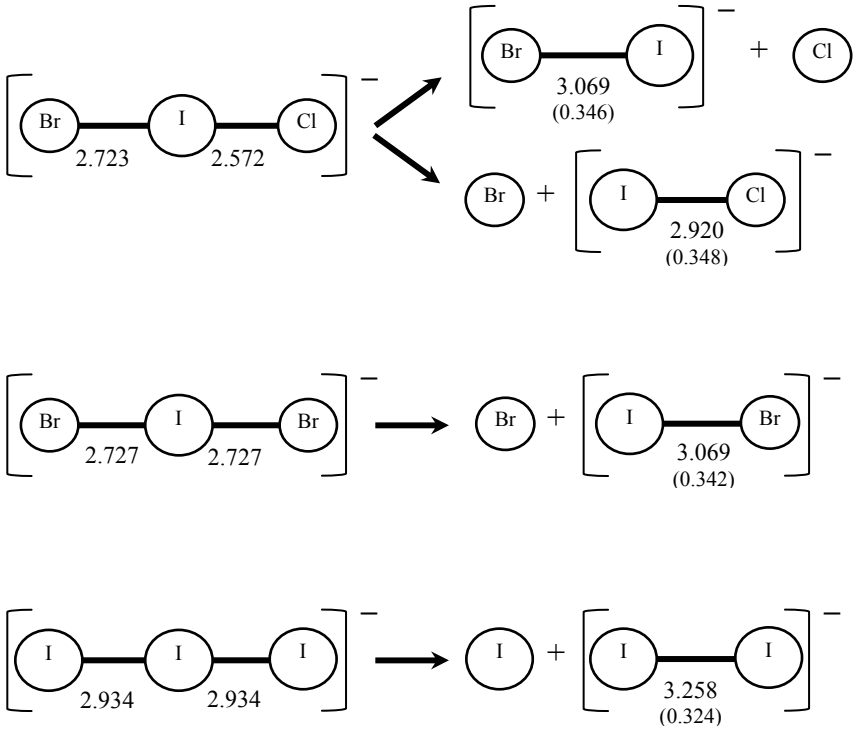

Figure 5.7: Equilibrium geometries of the $BrICl^-$, IBr_2^-, and I_3^- anions and their fragments, calculated using the *m*PW1PW method, as described in the text. Bond lengths are in angstroms. Numbers in parentheses indicate the bond elongation upon dissociation of the respective trihalide anion.

signal from ICl^-. The vibrational periods observed range from about 530 to 600 fs for $BrICl^-$ and 620 to 800 fs for IBr_2^-. These values correspond to frequencies of 63 to 56 cm^{-1} and 54 to 42 cm^{-1}, respectively.

The ground state vibrational frequency of IBr^- has been measured[28] to be ω_o = 136 cm^{-1}. The classical vibrational frequency scales as:

$$\omega(E) = \omega_o(E/D_o)^{1/2} \tag{5.1}$$

in the limit of the Morse oscillator model, where D_o is the dissociation energy and E is the energy below the I^- + Br threshold. The vibrational energy, E_v, is given by the expression $E_v = D_o - E$. Using Eq. 5.1, the $BrICl^-$ frequencies of 63 to 56 cm^{-1} correspond to average vibrational excitations from 0.79 to 0.83 of the IBr^- dissociation energy, D_o, which is about 1 eV. For IBr_2^-, the observed frequencies of 54 to 42 cm^{-1} lead to excitations of 0.84 to 0.91 of D_o. The I_2^- wavepacket was observed[11,12] to have a period of 550 fs (60 cm^{-1}) after photodissociation of I_3^- at 390 nm. The ground state vibrational frequency[23] of I_2^- is 110 cm^{-1} which corresponds to an average vibrational excitation of 70% of the dissociation energy after dissociation of I_3^-.

The overall picture at this point is that $BrICl^-$ and IBr_2^- show a larger geometry change upon dissociation to the dihalide species IBr^- and ICl^- than is seen in the corresponding I_3^- to I_2^- photodissociation process. This larger geometry change leads to the mixed dihalide anion products having more vibrational excitation than the I_2^- product. This geometry change results in the mixed dihalide anion

wavepackets being produced closer to the dissociation threshold, diminishing the prospects of detecting wavepacket revivals at long time delays.

5.7 Wave Packet Dynamics near Dissociation Threshold

One of the goals of studying the vibrational wavepacket dynamics of these dihalide anion photoproducts is to observe the wave packet revivals at long pump-probe delays. The wavepacket motion was only observed at short times (<10 ps) after formation, but then rapidly dephased due to the potential anharmonicity and signal was lost. At a later time, the wavepackets were expected to rephase and the signal to revive. However, these signal revivals were not detected. Experimental factors such as insufficient time resolution along with rotational dephasing and multiple spin-orbit surfaces that can be accessed during dissociation could in principle explain the lack of the revival observation. However, revivals were observed in the I_3^- experiments under similar experimental conditions.

The time-dependent wavefunction of a wavepacket is given by:

$$\psi(x,t) = \sum_{v} c_v u_v(x) \exp[-iE(v)t/\hbar] \tag{5.2}$$

where v is the vibrational quantum number, and c_v and $u_v(x)$ are the level amplitudes and spatial wavefunctions. The wavepacket initially created is real and localized. For short times after its creation, the wavepacket behaves classically.[29-31] During this time the position of the wavepacket can be finitely measured and produces the initial oscillations in the pump-probe signal (Figs. 5.4 and 5.6). However, the energy levels

E(v) of a quantum system are not uniformly spaced[32,33] leading to a delocalization or dephasing of the wave packet and its subsequent revivals. The energy levels of the system can be expanded in a Taylor series as a function of v to account for the anharmonicity of the potential well:

$$E(\mathrm{v}) = E(\bar{\mathrm{v}}) + (\mathrm{v}-\bar{\mathrm{v}})\frac{\partial E}{\partial \mathrm{v}}\bigg|_{\bar{\mathrm{v}}} + \frac{(\mathrm{v}-\bar{\mathrm{v}})^2}{2!}\frac{\partial^2 E}{\partial \mathrm{v}^2}\bigg|_{\bar{\mathrm{v}}} + \frac{(\mathrm{v}-\bar{\mathrm{v}})^3}{3!}\frac{\partial^3 E}{\partial \mathrm{v}^3}\bigg|_{\bar{\mathrm{v}}} + \ \ldots \tag{5.3}$$

where $\bar{\mathrm{v}}$ is the average level quantum number of the wavepacket. Equation 5.3 can also be written in the form[32,33]:

$$E(\mathrm{v}) = E(\bar{\mathrm{v}}) + 2\pi\hbar\frac{(\mathrm{v}-\bar{\mathrm{v}})}{T_{\mathrm{cl}}} \pm 2\pi\hbar\frac{(\mathrm{v}-\bar{\mathrm{v}})^2}{T_{\mathrm{rev}}} \pm 2\pi\hbar\frac{(\mathrm{v}-\bar{\mathrm{v}})^3}{T_{\mathrm{d}}} + \ \ldots \tag{5.4}$$

where the ± denotes the sign of the derivatives from Eq. 5.3. The value of T_{cl} is the classical vibrational period, T_{rev} is the wavepacket "revival" period, and T_d is the period for second-order revivals.[32-34] The higher order time scales in Eq. 5.4 can be defined in a similar manner, but are not discussed here.

For a Morse oscillator, the series in Eqs. 5.3 and 5.4 are terminated after the quadratic term which describes first-order anharmonicity. The resulting wavepacket dynamics displays two timescales: the linear term represents the classical period T_{cl} and the quadratic term gives the revival period T_{rev}.[32-34] When higher order terms are included, additional timescales appear in the dynamics. Much as the classical oscillations cease after a certain time, the periodic revivals should terminate as well

after a given propagation time as the higher order terms in Eq. 5.4 come into play. This smearing of the revival structure is described by the cubic term in Eq. 5.4. The value of T_d then represents the period of second-order revivals.

The frequency scaling with energy for a Morse oscillator is given by Eq. 5.1. In the case of the Morse potential, the wavepacket dynamics are described entirely in terms of oscillations and periodic revivals due to the value of T_d being infinite.[34] However, for a general potential, the higher order terms "explode" near dissociation threshold and smear out these expected revivals. For this revival picture to be valid, the cubic and higher order terms in Eq. 5.4 must be neglected. The condition for which this is valid[34] is:

$$1/T_{rev} >> |v - \bar{v}| / T_d \tag{5.5}$$

or

$$E >> \left(\frac{2\hbar\alpha}{3n} |v - \bar{v}| \right)^{\frac{2n}{n-2}} \tag{5.6}$$

where α is a constant, n is the parameter describing the long-range scaling of the potential, and v and $\bar{v}$ are described in Eq. 5.3. As the system nears the dissociation threshold, E approaches 0 and the condition of Eq. 5.6 breaks down. This leads to a breakdown of the revival picture of the wavepacket dynamics as one nears the dissociation threshold. The condition must be valid for all the terms that have significant amplitude in Eq. 5.2, so the case of $|v - \bar{v}| \approx N$ where N is the number of vibrational levels in the wave packet must be considered. For potentials with n>2, the number of bound levels is finite and N scales as $N \propto \Delta E/\omega \propto |dV/dR|/\omega$.

The potential gradient is taken at the initial position where the wavepacket is formed. In these experiments, the initial position of the wavepacket is on the inner wall of the IBr^- potential. Both the energy range (ΔE) and the level density, which is proportional to $1/\omega$, are increasing with E_v. This means that N is rapidly increasing near the dissociation threshold. The simplest approximation involves the reflection principle which entails projecting the ground state wavefunction of IBr_2^- onto the quantum levels of the IBr^-. A ballpark estimate of the spread ΔE is roughly 0.5 eV.

The long range potential for the near-threshold IBr^- is best approximated by the ion-neutral interaction which scales as R^{-4}. For this potential, the number of bound levels between $E_v = 0.8D_0$ and the dissociation level is $N \approx 10^2$. The right hand side of Eq. 5.10 is found to be ~0.08 eV when the other parameters are estimated. Overall, this analysis shows that the revival picture of the wavepacket dynamics is only valid when $E_v << 0.92$ eV, which is likely not the case in the $BrICl^-$ and IBr_2^- systems. The wavepackets in the experiments are formed too close to the dissociation threshold for the revival picture of the dynamics to be valid, thus the revivals are not observed in the time-dependent I^- signals.

The IBr^- vibrational excitation ($E_v \sim 0.9D_o$) observed in IBr_2^- photodissociation corresponds to the near-threshold regime where higher order timescales are important. On the other hand, in the Neumark experiment on gas phase I_3^-,[11,12,32,33] the vibrational excitation of I_2^- ($\sim 0.7D_o$) corresponds to the intermediate regime where the smearing of the early wavepacket revivals only begins to be important.

Time-dependent wavepacket simulations were carried out on two sets of

calculated IBr^- potentials[34] to determine the accuracy of the above analysis. The results of the simulation are shown in Fig. 5.8 with parts (a) and (b) representing the two different levels of theory for the potential calculations. The difference in revival times between the two levels of theory highlights the dependence of the revival times on the details of the potentials. The signals show the expected wavepacket revival structures[32,33] along with partial revivals of various orders for moderate vibrational excitation ($E_v \leq 0.6D_o$). As the vibrational excitation is increased, the revival structures become less intense ($E_v \approx 0.8D_o$) and are completely lost by $E_v = 0.93D_o$. This clearly agrees with the hypothesis that as the vibrational excitation in the wavepacket approaches the dissociation limit, the higher order timescales become more important and the wavepacket revival structures smear out. In the case of IBr^-, the vibrational excitation is around $0.9D_o$. The simulations suggest that this close proximity to the dissociation limit should smear the revivals to the point of being unobservable. The work[11,12] of the Neumark group on I_3^- produced wavepackets in I_2^- with ~$0.7D_o$ vibrational excitation from which they observe a wavepacket revival structure. According to the simulations, this intermediate regime should produce observable revivals where the smearing is just becoming important. As mentioned above, the I_2Br^- system could directly test the above hypothesis by forming the I_2^- wavepacket closer to the dissociation limit and determining if the previously observed revival structure from the I_3^- work is still present.

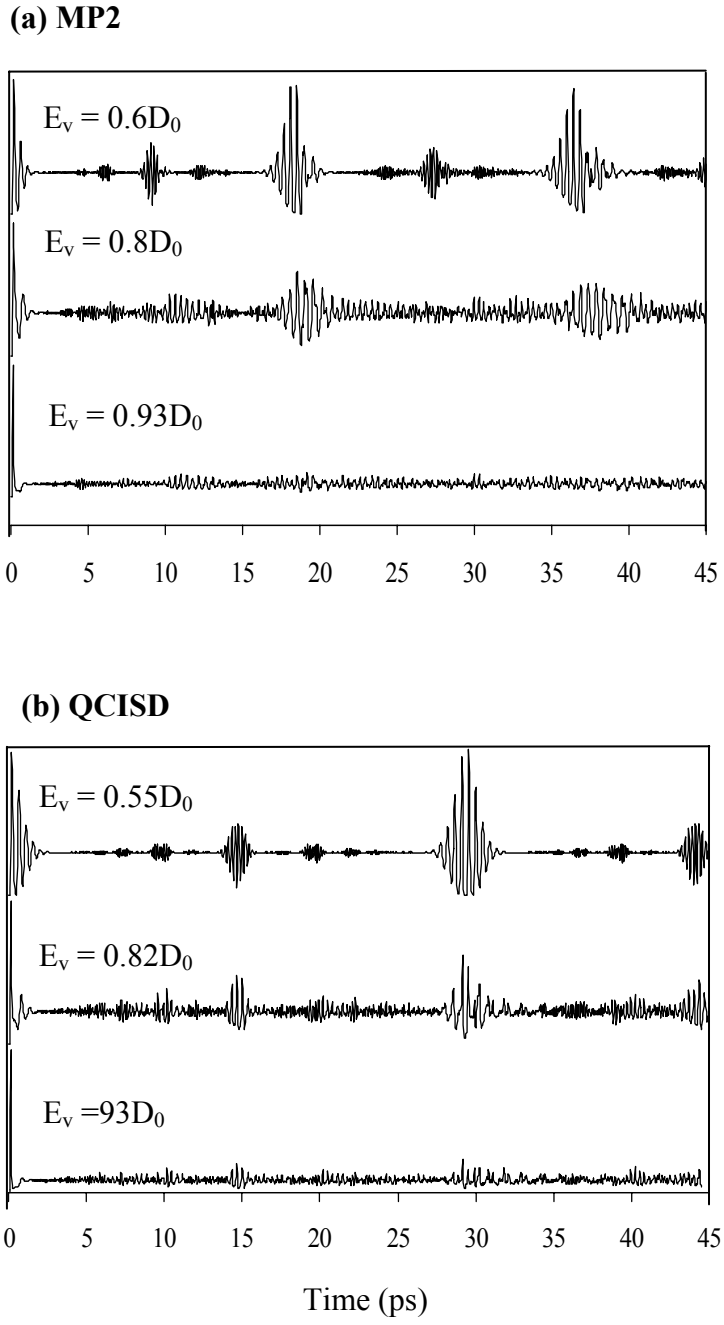

Figure 5.8: IBr^- absorption signals calculated by propagating wave-packets on the (a) MP2 and (b) QCISD potentials calculated in the reference in the text. The degrees of vibrational excitation are labeled above each set of absorption signals.

Chapter 5 References

[1] U. Banin, R. Kosloff, and S. Ruhman, Isr. J. Chem. **33**, 141 (1993).

[2] U. Banin, R. Kosloff, and S. Ruhman, Chem. Phys. **183**, 289 (1994).

[3] U. Banin and S. Ruhman, J. Chem. Phys. **98**, 4391 (1993).

[4] U. Banin and S. Ruhman, J. Chem. Phys. **99**, 9318 (1993).

[5] U. Banin, A. Waldman, and S. Ruhman, J. Chem. Phys. **96**, 2416 (1992).

[6] E. Gershgoren, U. Banin, and S. Ruhman, J. Phys. Chem. A **102**, 9 (1998).

[7] E. Gershgoren, E. Gordon, and S. Ruhman, J. Chem. Phys. **106**, 4806 (1997).

[8] T. Kühne, R. Kuster, and P. Vöhringer, Chem. Phys. **233**, 161 (1998).

[9] T. Kühne and P. Vöhringer, J. Chem. Phys. **105**, 10788 (1996).

[10] T. Kühne and P. Vöhringer, J. Phys. Chem. A **102**, 4177 (1998).

[11] M. T. Zanni, B. J. Greenblatt, A. V. Davis, and D. M. Neumark, Proc. SPIE **3271**, 196 (1998).

[12] M. T. Zanni, B. J. Greenblatt, A. V. Davis, and D. M. Neumark, J. Chem. Phys. **111**, 2991 (1999).

[13] M. A. Johnson and W. C. Lineberger, in *Techniques for the Study of Ion Molecule Reactions*, edited by J. M. Farrar and J. W. Saunders (Wiley, New York, 1988), pp. 591.

[14] D. Klar, M. W. Ruf, and H. Hotop, Australian Journal of Physics **45**, 263 (1992).

[15] D. Klar, M. W. Ruf, and H. Hotop, Chem. Phys. Lett. **189**, 448 (1992).

[16] J. P. Ziesel, I. Nenner, and G. J. Schulz, J. Chem. Phys. **63**, 1943 (1975).

[17] J. P. Ziesel, G. J. Schulz, and J. Milhaud, J. Chem. Phys. **62**, 1936 (1975).

[18] M. J. Frisch, G. W. Trucks, H. B. Schlegel, G. E. Scuseria, M. A. Robb, J. R. Cheeseman, V. G. Zakrzewski, J. A. Montgomery, R. E. Stratmann, J. C. Burant, S. Dapprich, J. M. Millam, A. D. Daniels, K. N. Kudin, M. C. Strain, O. Farkas, J. Tomasi, V. Barone, M. Cossi, R. Cammi, B. Mennucci, C. Pomelli, C. Adamo, S. Clifford, J. Ochterski, G. A. Petersson, P. Y. Ayala, Q. Cui, K. Morokuma, D. K. Malick, A. D. Rabuck, K. Raghavachari, J. B. Foresman, J. Cioslowski, J. V. Ortiz, B. B. Stefanov, G. Liu, A. Liashenko, P. Piskorz, I. Komaromi, R. Gomperts, R. L. Martin, D. J. Fox, T. Keith, M. A. Al-Laham, C. Y. Peng, A. Nanayakkara, C. Gonzalez, M. Challacombe, P. M. W. Gill, B. G. Johnson, W. Chen, M. W. Wong, J. L. Andres, M. Head-Gordon, E. S. Replogle, and J. A. Pople, Gaussian 98, Rev. A.1 (Gaussian, Inc., Pittsburgh, PA, 1998).

[19] C. Adamo and V. Barone, J. Chem. Phys. **108**, 664 (1998).

[20] W. R. Wadt and P. J. Hay, J. Chem. Phys. **82**, 284 (1985).

[21] M. N. Glukhovtsev, A. Pross, and L. Radom, J. Am. Chem. Soc. **117**, 2024 (1995).

[22] B. J. Greenblatt, M. T. Zanni, and D. M. Neumark, Chem. Phys. Lett. **258**, 523 (1996).

[23] M. T. Zanni, T. R. Taylor, B. J. Greenblatt, B. Soep, and D. M. Neumark, J. Chem. Phys. **107**, 7613 (1997).

[24] K. Do, T. P. Klein, C. A. Pommerening, and L. S. Sunderlin, J. Am. Soc. Mass Spectrom. **8**, 688 (1997).

[25] M. E. Nadal, P. D. Kleiber, and W. C. Lineberger, J. Chem. Phys. **105**, 504 (1996).

[26] M. E. Nadal, Ph.D. Thesis, University of Colorado, 1996.

[27] I. S. Averbukh, M. J. J. Vrakking, D. M. Villeneuve, and A. Stolow, Phys. Rev. Lett. **77**, 3518 (1996).

[28] E. Gershgoren and S. Ruhman, private communication.

[29] N. Bohr, Z. Phys. **13**, 117 (1923).

[30] L. D. Landau and E. M. Lifshitz, *Quantum Mechanics: Nonrelativistic Theory*, 3rd ed. ed. (Pergamon Press, Oxford, 1977).

[31] E. Schrödinger, Naturwiss. **14**, 664 (1926).

[32] I. S. Averbukh and N. F. Perelman, Phys. Lett. A. **139**, 449 (1989).

[33] I. S. Averbukh and N. F. Perelman, Uspekhi Fiz. Nauk. **34**, 572 (1991).

[34] A. Sanov, T. Sanford, L. J. Butler, J. Vala, R. Kosloff, and W. C. Lineberger, J. Phys. Chem. A. **103**, 10244 (1999).

Chapter 6

Conclusion

The overall goal of this dissertation was to study the process of solvation at the molecular level by the use of gas-phase ionic clusters. These ionic clusters provide weakly bound solutes surrounded by a controllable number of solvent molecules. This solvent control allowed for the step-wise study of the effect of increasing solvation on the solute. It also provides well-defined solvent environments not found in condensed phase. The statistical nature to the observations in condensed phase environments made solvent studies in condensed phase media incomplete at the molecular level of understanding. Initially, the photodissociation dynamics of size-selected $IBr^-(CO_2)_n$ cluster ions are studied as a method to understand solvation at the microscopic level. This provides numerous insights into the detailed nature of the size-dependent effects of the solvent on the anion solute. However, the complete picture of the time-resolved dynamics is inaccessible using this method. Photoelectron imaging spectroscopy is then carried out on $Cu^-(H_2O)_n$ complexes to both characterize the new imaging spectrometer and determine the effect of a few H_2O solvents on the electronic structure of the atomic anion solute.

The second chapter of the dissertation described in detail the existing cluster ion source and tandem time-of-flight mass spectrometer. The modifications on the apparatus for the production and study of $IBr^-(CO_2)_n$ clusters were highlighted. Of central importance in this chapter was the design and description of the new photoelectron imaging spectrometer. The spectrometer was designed such that it

could be implemented into the existing apparatus with no loss of the original functionality. The image collection scheme along with the processing of the image data was described in some detail.

The photodissociation study of $IBr^-(CO_2)_n$ clusters built on previous work in the Lineberger group on $ICl^-(CO_2)_n$ and $I_2^-(CO_2)_n$ cluster ions and was the focus of Ch. 3. The IBr^- solute was attractive to study, because it provides a mixed halide solute with absorption cross sections and size-dependent recombination behavior that was thought to be ideally suited for time-resolved solvation dynamics studies. The spectroscopic properties of the bare IBr^- solute were characterized. The A' absorption band was measured and found to provide substantial cross section in the near-IR around 750 nm; ideal for the femtosecond laser system. The bond dissociation energy was found to be comparable to that of the two previously studied dihalide solutes at around 1.10 eV. The size selected $IBr^-(CO_2)_n$ clusters were excited to the A' and B electronic states of the solute anion. Photodissociation on A' yielded the expected I^- photoproduct in the unsolvated case. As the solvation was increased, the formation of the charge transfer Br^--based products occurred with recombination on the ground state beginning soon after with the addition of the second CO_2 solvent molecule. Recombination on the ground state reached 100% at n = 8 representing the smaller Br completely enclosed by the solvent molecules. The $IBr^-(CO_2)_n$ clusters exhibited behavior similar to $ICl^-(CO_2)_n$ clusters in that recombination first occurred at very small cluster sizes, unlike the recombination behavior observed for $I_2^-(CO_2)_n$. However, $IBr^-(CO_2)_n$ clusters did demonstrate increasing recombination with increasing cluster size unlike that found in $ICl^-(CO_2)_n$ in which the charge-transfer

Cl^--based products are formed exclusively at large cluster sizes with recombination reaching zero.

The unexpected recombination behavior in $ICl^-(CO_2)_n$ clusters is due to the presence of an excited state well corresponding to solvated Cl^- that increases with increasing cluster size. A similar well is thought to be present on the likewise asymmetric IBr^- potentials. A pump-probe experiment was carried out on $IBr^-(CO_2)_8$, which exhibits 100% recombination, to determine the timescale for recombination on the ground state after excitation on A'. No recombination on the ground state was observed before 200 ps, with significant recombination occurring at 5 and 8 ns. This result is in stark contrast to results in $I_2^-(CO_2)_n$ clusters after similar excitations that show recombination occurring on the tens of picoseconds timescales. This large difference is attributed to the presence of an excited state well similar to that found in solvated ICl^-. The well is not as deep, however, allowing for recombination to be observed on the nanosecond timescale. At large cluster sizes, the well traps the ICl^- for at least 10 μs (the time for detection on the off-axis detector) due to the absence of observed recombined products. The experiment is limited, however, in that the time-resolved dynamics can only be probed in the narrow window when the solute chromophore is recombined on the ground state.

Photoelectron imaging spectroscopy is thought to provide a much more powerful tool for probing the excited state dynamics at all times after photoexcitation. The new imaging spectrometer was characterized by the study of $Cu^-(H_2O)_n$ complexes. The bare Cu^- solute was used to optimize the spectrometer as well as provide a baseline to determine the effects of the addition of a few H_2O solvent

molecules. The spectrometer was shown to provide very good energy resolution in the spectra. A pulsed laser was used for the photodetachment and allowed for a wide range of wavelength tunability. This tunability allowed the study of selected features in the spectra at low photoelectron kinetic energies, thus providing higher resolution. The overall trend of increased solvation was to shift the unsolvated, atomic features to higher electron binding energies. Substantial peak broadening was also observed and is understood in terms of the sizes of the atomic anion versus the atomic neutral solute depending on the orbital from which the electron is detached. Some charge delocalization onto the H_2O solvent was observed by the presence of small features just above the VDE of the complexes that were assigned to the H_2O bending mode. The $Cu(H_2O)$ complex ground state was shown to be surprisingly narrow and was used to determine a dissociation energy of the complex.

Future work will center on the extension of the photoelectron imaging spectrometer to more complex and larger solvent systems as well as to address outstanding issues from previous work. The excited state dynamics of the $IBr^-(CO_2)_n$ must be probed in more depth. The recombination time at this point is still quite uncertain. It was found to be greater than 200 ps, which was itself a valuable discovery, but the exact recombination time is unknown over a few orders of magnitude. Time-resolved imaging spectroscopy can potentially follow the dynamics at all times from initial photodissociation through recombination on the ground state, including monitoring the motion of the solvent and the charge-transfer between the dissociating atoms. Additional solvation was shown to produce shifts in the electron binding energies in $Cu^-(H_2O)_n$ complexes. These shifts will also be present in the

dihalide systems as the solvent rearranges to solvate a newly formed charge center, for instance. The nature and location of the excited state well in $IBr^-(CO_2)_n$ can also now be probed. Time-resolved dynamics can be carried out for the first time on $ICl^-(CO_2)_n$ clusters, which was inaccessible due to the constraints of the absorption recovery experiments. Another exciting prospect is the study of solute anions which produce molecular dissociation photoproducts. Clusters involving solutes such as ICN^- or $BrCN^-$ are of great interest in that photoproducts based on CN^- can be produced from which the vibrational state distributions may be able to be probed using the imaging spectrometer. Finally, the trihalide anions could provide an interesting system on which to study solvation. Some clustering of the trihalides has been observed in these systems, though not reported here. The wavepacket studies on the dihalide anions formed from photodissociation of the precursor trihalides demonstrated the critical importance of the location where the dihalide is formed on the ground state potential in determining the subsequent wavepacket dynamics. Due to the nature of the photodissociation of the trihalides studied, the dihalide products were formed quite high on the well smearing out the expected revivals in the wavepackets. The presence of a solvent could lead to vibrational excitation transfer from the dihalide allowing for some degree of vibrational relaxation. The reappearance of the revival structure could then be probed as the degree of solvation is increased leading to formation of the dihalide at lower vibrational energy levels.

Bibliography

Adamo, C. and Barone, V., *Journal of Chemical Physics*. **108**, 664-675 (1998).

Alexander, M. L., Levinger, N. E., Johnson, M. A., Ray, D. and Lineberger, W. C., *Journal of Chemical Physics*. **88**, 6200-10 (1988).

Antusek, A., Urban, M. and Sadlej, A. J., *Journal of Chemical Physics*. **119**, 7247-7262 (2003).

Arnold, D. W., Bradforth, S. E., Kim, E. H. and Neumark, D. M., *Journal of Chemical Physics*. **97**, 9468-70 (1992).

Arnold, D. W., Bradforth, S. E., Kim, E. H. and Neumark, D. M., *Journal of Chemical Physics*. **102**, 3510-18 (1995).

Averbukh, I. S. and Perelman, N. F., *Physics Letters A*. **139**, 449-453 (1989).

Averbukh, I. S. and Perelman, N. F., *Sov. Phys. Usp.* **34**, 572-591 (1991).

Averbukh, I. S., Vrakking, M. J. J., Villeneuve, D. M. and Stolow, A., *Physical Review Letters*. **77**, 3518-3521 (1996).

Banin, U., Waldman, A. and Ruhman, S., *Journal of Chemical Physics*. **96**, 2416-2419 (1992).

Banin, U., Kosloff, R. and Ruhman, S., *Israel Journal Of Chemistry*. **33**, 141-156 (1993).

Banin, U. and Ruhman, S.,*Journal Of Chemical Physics*. **98**, 4391-4403 (1993).

Banin, U. and Ruhman, S., *Journal Of Chemical Physics*. **99**, 9318-9321 (1993).

Banin, U., Kosloff, R. and Ruhman, S., *Chemical Physics*. **183**, 289-307 (1994).

Bilodeau, R. C., Scheer, M. and Haugen, H. K., *J. Phys. B*. **31**, 3885-3891 (1998).

Blanksby, S. J., Ramond, T. M., Davico, G. E., Nimlos, M. R., Kato, S., Bierbaum, V. M., Lineberger, W. C., Ellison, G. B. and Okumura, M., *Journal of the American Chemical Society*. **123**, 9585-9596 (2001).

Bohr, N., *Z. Phys.* **13**, 117 (1923).

Bragg, A. E., Verlet, J. R. R., Kammrath, A. and Neumark, D. M., *Journal of*

Chemical Physics. **104**, 3515 (2004).

Busch, G. E., Mahoney, R. T., Morse, R. I. and Wilson, K. R., *Journal of Chemical Physics*. **51**, 449-450 (1969).

Castleman, A. W. *International Journal Of Mass Spectrometry And Ion Processes*. **118**, 167-189 (1992).

Castleman, A. W. and Bowen, K. H., *Journal Of Physical Chemistry*. **100**, 12911-12944 (1996).

Castleman, A. W., Jr. and Keesee, R. G., *Chemical Reviews*. **86**, 589-618 (1986).

Chandler, D. W. and Houston, P. L., *Journal of Chemical Physics*. **87**, 1445-1447 (1987).

Chase, M. W., Jr., Davies, C. A., Downey, J. R., Jr., Frurip, D. J., McDonald, R. A. and Syverud, A.N., *JANAF Thermochemical Tables (J. Phys. Chem. Ref. Data 14)*. 421 (1985).

Cooper, J. and Zare, R. N., *Journal of Chemical Physics*. **48**, 942-943 (1968).

Davis, A. V., Wester, R., Bragg, A. E. and Neumark, D. M., *Journal of Chemical Physics*. **118**, 999 (2003).

Delaney, N., Faeder, J. and Parson, R., *Journal of Chemical Physics*. **111**, 651 (1999).

Delaney, N., Ph.D. Thesis, University of Colorado (1999).

Do, K., Klein, T. P., Pommerening, C. A. and Sunderlin, L. S., *Journal of the American Society For Mass Spectrometry*. **8**, 688-696 (1997).

Dribinski, V., Ossadtchi, A., Mandelshtam, V. and Reisler, H., *Review of Scientific Instruments*. **73**, 2634 (2002).

Dunn, M. H. and Ebrahimzadeh, M., *Science*. **286**, 1513-1517 (1999).

Engelking, P. C., *Journal of Chemical Physics*. **87**, 936-40 (1987).

Eppink, A. and Parker, D. H., *Review of Scientific Instruments*. **68**, 3477-3484 (1997).

Ervin, K. M., Gronert, S., Barlow, S. E., Gilles, M. K., Harrison, A. G., Bierbaum, V. M., DePuy, C. H., Lineberger, W. C. and Ellison, G. B., *Journal of the American Chemical Society*. **112**, 5750 (1990).

Even, U., Jortner, J., Noy, D., Lavie, N. and Cossart-Magos, C., *Journal of Chemical Physics*. **112**, 8068-8071 (2000).

Faeder, J., Delaney, N., Maslen, P. E. and Parson, R., *Chemical Physics*. **239**, 525-548 (1998).

Faeder, J., Ph.D. Thesis, University of Colorado (1998).

Franck, J. and Rabinowitch, E., *Trans. Faraday Soc.* **30**, 120 (1934).

Frisch, M.J., Trucks, G.W., Schlegel, H.B., et.al., "Gaussian 98," (1998).

Gershgoren, E. and Ruhman, S., *private communication*.

Gershgoren, E., Gordon, E. and Ruhman, S., *Journal Of Chemical Physics*. **106**, 4806-4809 (1997).

Gershgoren, E., Banin, U. and Ruhman, S.,*Journal of Physical Chemistry A.***102**, 9-16 (1998).

Glukhovtsev, M. N., Pross, A. and Radom, L., *Journal of the American Chemical Society*. **117**, 2024-2032 (1995).

Greenblatt, B. J., Zanni, M. T. and Neumark, D. M., *Chemical Physics Letters*. **258**, 523-529 (1996).

Greenblatt, B. J., Zanni, M. T. and Neumark, D. M., *Journal of Chemical Physics*. **112**, 601 (2000).

Harris, A. L., Brown, J. K. and Harris, C. B., *Annual Review of Physical Chemistry*. **39**, 341-366 (1988).

Hillenkamp, M., Keinan, S. and Even, U., *Journal of Chemical Physics*. **118,** 8699 (2003).

Ho, J., Ervin, K. M. and Lineberger, W. C., *Journal of Chemical Physics*. **93**, 6987-7002 (1990).

Johnson, A. E., Levinger, N. E. and Barbara, P. F., *Journal of Physical Chemistry*. **96**, 7841 (1992).

Kafka, J. D., Watts, M. L. and Pieterse, J.-W. J., *IEEE Journal of Quantum Electronics*. **28**, 2151-2162 (1992).

Kauffman, J. W., Hauge, R. H. and Margrave, J. L., *Journal of Physical Chemistry*. **89**, 3541-47 (1985).

Keeton, W. T. and Gould, J. L., *Biological Science*. New York, W.W. Norton &

Co.: (1993).

Klar, D., Ruf, M. W. and Hotop, H., *Australian Journal of Physics*. **45**, 263-291 (1992).

Klar, D., Ruf, M. W. and Hotop, H., *Chemical Physics Letters*. **189**, 448-454 (1992).

Kliner, D. A. V., Alfano, J. C. and Barbara, P. F., *Journal of Chemical Physics*. **98**, 5375 (1993).

Kühne, T. and Vöhringer, P., *Journal of Chemical Physics*. **105**, 10788-10802 (1996).

Kühne, T., Kuster, R. and Vöhringer, P., *Chemical Physics*. **233**, 161-178 (1998).

Kühne, T. and Vöhringer, P., *Journal of Physical Chemistry A*. **102**, 4177-4185 (1998).

Landau, L. D. and Lifshitz, E. M., *Quantum Mechanics: Nonrelativistic Theory*. Oxford, Pergamon Press: (1977).

Levinger, N.E., Ph.D. Thesis, University of Colorado (1990).

Mabbs, R., Surber, E. and Sanov, A., *Analyst*. **128**, 765-772 (2003).

Mabbs, R., Pichugin, K., Surber, E. and Sanov, A., *Journal of Chemical Physics*. **121**, 265-272 (2004).

Mamyrin, B. A., Karataev, V. I., Shmikk, D. V. and Zagulin, V. A., *Sov. Phys.-JEPT*. **37**, 45 (1973).

Marcus, Y., *Ion Solvation*. New York, Wiley: (1985).

Maslen, P. E., Papanikolas, J. M., Faeder, J., Parson, R. and O'Neil, S. V., *Journal of Chemical Physics*. **101**, 5731-5755 (1994).

Maslen, P. E., Faeder, J. and Parson, R., *Chemical Physics Letters*. **263**, 63-72 (1996).

Meadows, L. F. and Noyes, R. M., *Journal of the American Chemical Society*. **82**, 1872 (1960).

Misaizu, F., Tsukamato, K., Sanekata, M. and Fuke, K., *Laser Chemistry*. **15**, 195-207 (1995).

Misaizu, F., Tsukamoto, K., Sanekata, M. and Fuke, K., *Surface Review and Letters*. **3**, 405-410 (1996).

Moore, C. E., *Atomic Energy Levels*. National Bureau of Standards, Washington, D.C.: (1949).

Muntean, F., Taylor, M. S., McCoy, A. B. and Lineberger, W. C., *Journal of Chemical Physics*. **121**, 5676 (2004).

Nadal, M. E., Kleiber, P. D. and Lineberger, W. C., *Journal Of Chemical Physics*. **105**, 504-514 (1996).

Nadal, M.E., Ph.D. Thesis, University of Colorado (1996).

Nandi, S., Sanov, A., Delaney, N., Faeder, J., Parson, R. and Lineberger, W.C., *Journal of Physical Chemistry*. **102**, 8827-8835 (1998).

Neumark, D. M., *PhysChemComm*. **11**, 76-81 (2002).

Neumark, D. M., *Science*. **272**, 1446-1447 (1996).

Osterwalder, A., Nee, M. J., Zhou, J. and Neumark, D. M., *Journal of Chemical Physics*. **121**, 6317-6322 (2004).

Otto, B., Schroeder, J. and Troe, J.*Journal of Chemical Physics*.**81**,202(1984).

Papanikolas, J. M., Gord, J. R., Levinger, N. E., Ray, D., Vorsa, V. and Lineberger, W. C., *Journal of Physical Chemistry*. **95**, 8028-40 (1991).

Papanikolas, J. M., Vorsa, V., Nadal, M. E., Campagnola, P. J., Gord, J. R. and Lineberger, W. C., *Journal of Chemical Physics*. **97**, 7002-7005 (1992).

Papanikolas, J. M., Vorsa, V., Nadal, M. E., Campagnola, P. J., Buchenau, H. K. and Lineberger, W. C., *Journal of Chemical Physics*. **99**, 8733-8750 (1993).

Papanikolas, J.M., Ph.D. Thesis, University of Colorado (1994).

Parson, R., Faeder, J. and Delaney, N., *Journal of Physical Chemistry A*. **104**, 9653 (2000).

Posey, L. A., DeLuca, M. J. and Johnson, M. A., *Chemical Physics Letters*. **131**, 170-174 (1986).

Ramond, T.M., Ph.D. Thesis, University of Colorado (2001).

Ravishankara, A. R., *Science*. **276**,1058-1065 (1997).

Reid, K. L., *Annual Review of Physical Chemistry*. **54**, 397-424 (2003).

Robertson, W. H., Kelley, J. A. and Johnson, M. A., *Review of Scientific Instruments*. **71**, 4431-4434 (2000).

Sanford, T., Han, S.-Y., Thompson, M. A., Parson, R. and Lineberger, W. C., *in press*. (2004).

Sanov, A., Sanford, T., Butler, L. J., Vala, J., Kosloff, R. and Lineberger, W.C., *Journal of Physical Chemistry A*. **103**, 10244-10254 (1999).

Sanov, A., Sanford, T., Nandi, S. and Lineberger, W. C. *Journal of Chemical Physics*. **111**, 664-675 (1999).

Sanov, A. and Lineberger, W. C., *PhysChemComm*. **5**, 165-177 (2002).

Sanov, A. and Lineberger, W. C., *Physical Chemistry Chemical Physics*. **6**, 2018-2032 (2004).

Schrödinger, E., *Naturwiss*. **14**, 664 (1926).

Shimanouchi, T., *Tables of Molecular Vibrational Frequencies Consolidated Volume I*. Washington, D.C., National Bureau of Standards: (1972).

Siegman, A. E., *Lasers*. Mill Valley, CA, University Science Books: (1986).

Smalley, R. E., Wharton, L. and Levy, D. H., *Accounts Of Chemical Research*. **10**, 139-145 (1977).

Steinfeld, J. I., Francisco, J. S. and Hase, W. L., *Chemical Kinetics and Dyanmics*. Englewood Cliffs, New Jersey, Prentice Hall: (1989).

Sugar, J. and Musgrove, A., *Journal of Physical Chemistry Reference Data*.**19**, 527-616 (1990).

Surber, E., Mabbs, R. and Sanov, A., *Journal of Physical Chemistry A*. **107**, 8215-8224 (2003).

Taylor, M. S., Barbera, J., Schulz, C. P., Muntean, F., McCoy, A. B. and Lineberger, W. C., *Journal of Chemical Physics*. **submitted**, (2004).

Taylor, M. S., Muntean, F., Lineberger, W. C. and McCoy, A. B., *Journal of Chemical Physics*. **121**, 5688 (2004).

Taylor, M. S., Ph.D. Thesis, University of Colorado (2004).

Thompson, M. A. and Parson, R., *unpublished results*. (2004).

Troe, J., *Ann. Rev. Phys. Chem.* **29**, 223-250 (1978).

Vorsa, V., Nandi, S., Campagnola, P. J., Larsson, M. and Lineberger, W. C., *Journal of Chemical Physics*. **106**, 1402-1410 (1997).

Wadt, W. R. and Hay, P. J., *Journal of Chemical Physics*. **82**, 284-298 (1985).

Wang, L., Kohguchi, H. and Suzuki, T., *Faraday Discussions*. **113**, 37-46 (1999).

Wiley, W. C. and McLaren, I. H., *Review of Scientific Instruments*. **26**, 1150 (1955).

Xu, X., Yu, S., Lingle, R., Zhu, H. and Hopkins, J. B., *Journal of Chemical Physics*. **95**, 2445 (1991).

Zanni, M. T., Taylor, T. R., Greenblatt, B. J., Soep, B. and Neumark, D. M., *Journal of Chemical Physics*. **107**, 7613-7619 (1997).

Zanni, M. T., Greenblatt, B. J., Davis, A. V. and Neumark, D. M., *Proc. SPIE*. **3271**, 196-207 (1998).

Zanni, M. T., Greenblatt, B. J., Davis, A. V. and Neumark, D. M., *Journal of Chemical Physics*. **111**, 2991 (1999).

Ziesel, J. P., Nenner, I. and Schulz, G. J., *Journal of Chemical Physics*. **63**, 1943-1949 (1975).

Ziesel, J. P., Schulz, G. J. and Milhaud, J., *Journal of Chemical Physics*. **62**, 1936-1940 (1975).